Politecnico di Torino
Corso di Laurea in Ingegneria Meccanica
A.a. 2024/2025
Sessione di Laurea Luglio 2025

Analysis of hydrogen embrittlement susceptibility of H_2ICE components

Relatori:
Prof. Graziano Ubertalli
Prof. Paolo Matteis

Candidato:
Matteo Astolfi

Acknowledgements

A heartfelt thank you to all the people who made it possible for me to get this far and complete this thesis work. A big thank you to Dr. Sujith S V, for his constant support, for providing me with high quality data by self-operating FeSEM and Mechanical Tests required for my thesis project and for promptly suggesting the right changes to be made. Also, thank you to Salvatore Guastella for his help in allowing the use of the laboratories. Of course, my biggest thanks go to my father, who always looking down on us from above, my mother, my brother and, in general, my entire family, whose support and encouragement allowed me to complete this course, and for always making me feel the warmth of their affection despite the difficult times. Thank you to my friends for always being there, even during this last phase of my master studies.

Abstract

Hydrogen embrittlement (HE) leads to significant materials degradation, given by dissolved hydrogen that detrimentally affects the mechanical properties of metals, including ductility, toughness, and strength. The present study addresses HE in internal combustion engine (ICE) (General Motors) parts sourced from Dumarey. The motive is to reveal the susceptibility to HE of IC engine parts in hydrogen-rich environments. The research methodology integrated a comprehensive literature review of hydrogen-metal interactions with targeted experimental evaluations. Materials were subjected to electrochemical hydrogen charging, followed by slow strain rate tensile (SSRT) testing at a strain rate of $5x10^{-5}$ s^{-1} to quantify variation in mechanical performance. Post-mortem analyses involved scanning electron microscopy (SEM) and energy-dispersive X-ray spectroscopy (EDS) followed by detailed fractographic analysis. Key findings revealed variation in the responses under hydrogen environment. Al-Si alloy from the engine head exhibited a significant reduction in ductility (~67%) with a mixed-mode fracture. In contrast, the Al-Si piston blank displayed an atypical increase in ultimate tensile strength and elongation, despite both charged and uncharged specimens shown inherently low ductility. Grey cast iron from the engine block demonstrated increased brittleness, with reductions in both ultimate tensile strength and ductility (~31%). Ductile cast iron from the exhaust manifold showed minimal strength loss but an unexpected increase in ductility after hydrogen charging, a result warranting further investigation. A central theme emerging from this work is the critical influence of microstructural features, particularly the nature, density, and distribution of hydrogen trap sites such as Si particles and intermetallic phases in Al-Si alloys, and graphite morphology and carbides in cast irons, on the overall HE susceptibility. These findings bear considerable importance for the informed selection and design of materials intended for application in emerging hydrogen-based IC engines.

Table of Contents

1. Introduction

The dawn of the 21st century has been marked by an urgent global pivot towards sustainable energy systems, driven by the dual imperatives of mitigating climate change and ensuring long-term energy security. In this transformative landscape, hydrogen has emerged as a cornerstone of future energy strategies, heralding the concept of a "hydrogen economy" where it serves as a versatile, clean energy carrier across various sectors [1]. Projections indicate substantial growth in hydrogen production and utilization, with significant investments fuelling innovation in production, and storage applications [2]. However, the widespread adoption of hydrogen, particularly in applications involving metallic materials, confronts a tough and insidious challenge known as hydrogen embrittlement (HE).

Hydrogen embrittlement is a complex materials degradation phenomenon where the absorption of hydrogen atoms into a metal's lattice structure leads to a significant and often catastrophic reduction in its mechanical properties, notably ductility, fracture toughness, and ultimate tensile strength [3]. This degradation can cause unexpected brittle failures in components that would otherwise be considered ductile, posing serious risks to structural integrity and operational safety across a multitude of engineering applications. The sources of hydrogen are varied, ranging from manufacturing processes such as electroplating, welding, and pickling, to in-service exposure in corrosive environments, under cathodic protection, or in direct contact with hydrogen gas, as is increasingly common in the hydrogen infrastructure. While strategies like careful material selection, protective coatings, and post-fabrication heat treatments are employed to mitigate HE, its unpredictable nature continues to present substantial hurdles in material design and engineering, particularly as new hydrogen-based technologies come to the fore.

One such promising technology is the hydrogen-fueled internal combustion engine (H_2ICE). H_2ICEs offer a pathway to decarbonize sectors where electrification faces challenges, such as heavy-duty transport and off-road applications, by leveraging much of the existing engine manufacturing infrastructure and expertise while producing zero CO_2 and low NO_x emissions [4]. Despite their potential, the transition to hydrogen fuel introduces unique material challenges. Engine components in H_2ICEs are exposed to a hydrogen-rich atmosphere, often at elevated temperatures and under dynamic stress conditions, creating an environment conducive to hydrogen ingress and subsequent embrittlement. Issues such as pre-ignition, backfiring, and ensuring material durability in the presence of hydrogen are critical areas of research and development. The long-term reliability and safety of H_2ICEs must be explored for the mitigation of HE.

This master's thesis focuses on the critical intersection of emerging energy technology and materials science, focusing on the hydrogen embrittlement susceptibility of specific engineering alloys used in a hydrogen-fueled internal combustion engine (H_2ICE). The research investigates components sourced from General Motors H_2ICE provided by Dumarey, specifically Al-Si alloys used for the engine head and the piston blank, and cast irons utilized for the exhaust manifold (ductile cast iron) and the engine block (grey cast iron). While the fundamental mechanisms of HE are broadly studied, their specific display in these complex commercial alloys, with their intricate microstructures developed for demanding engine applications, necessitates targeted investigation. The primary aim of this work is to systematically evaluate and compare the HE susceptibility of these selected Al-Si and cast iron engine components. To achieve this, the research integrates a review of scientific literature on hydrogen-material interactions and HE mechanisms with a focused experimental investigation. This technique involves electrochemical hydrogen charging of the materials to simulate hydrogen exposure, followed by slow strain rate tensile (SSRT) testing to quantify changes in mechanical properties. Detailed microstructural characterization and fractographic analysis using scanning electron microscopy (SEM) and energy-dispersive X-ray spectroscopy (EDS) are then employed to correlate mechanical behavior with microstructural features and identify operative embrittlement mechanisms.

The thesis is structured to provide a comprehensive understanding of the research undertaken. It begins with an in-depth scientific literature review covering hydrogen characteristics and fundamental hydrogen-metal interactions (adsorption, absorption, diffusion and trapping). It then continues focusing on established HE mechanisms, material-specific HE phenomena in relevant alloys (including aluminum alloys and cast irons), and current HE testing and prevention strategies. This is followed by a detailed description of the experimental procedures, encompassing material preparation, hydrogen charging protocols, mechanical testing (SSRT), and the techniques used for microstructural and fractographic characterization. Subsequently, the results from the mechanical tests and the microstructural/fractographic analyses are presented and critically discussed. This discussion focuses on the observed embrittlement phenomena, on the comparison of the HE susceptibility of the different aluminum and cast iron alloys and on the exploration of the influence of microstructural features, such as hydrogen trap sites. Finally, an analysis of an engine spark plug after service in the presence of hydrogen in an H_2ICE is presented as a case study to assess potential in-service hydrogen-related degradation before drawing overall conclusions from the research findings and offering recommendations for future work. This investigation seeks to contribute valuable insights for the informed selection and design of materials destined for the demanding environment of hydrogen-fueled internal combustion engines, thereby supporting the advancement of this important clean energy technology.

2. Hydrogen characteristics and behaviour

Hydrogen is the first element in the periodic table, with atomic number 1, and the lightest. It's the most abundant element in the universe and the third most on Earth [5]. Under standard conditions, it exists as a diatomic, colourless, and odourless gas (H_2) with a very low density of about 0.09 g/L and remarkably low melting and boiling points of approximately –259°C and –253°C, respectively. Its unique electronic configuration, consisting of just one electron orbiting a single proton, makes hydrogen the only atom for which the Schrödinger equation can be solved exactly, providing a fundamental model in quantum mechanics.

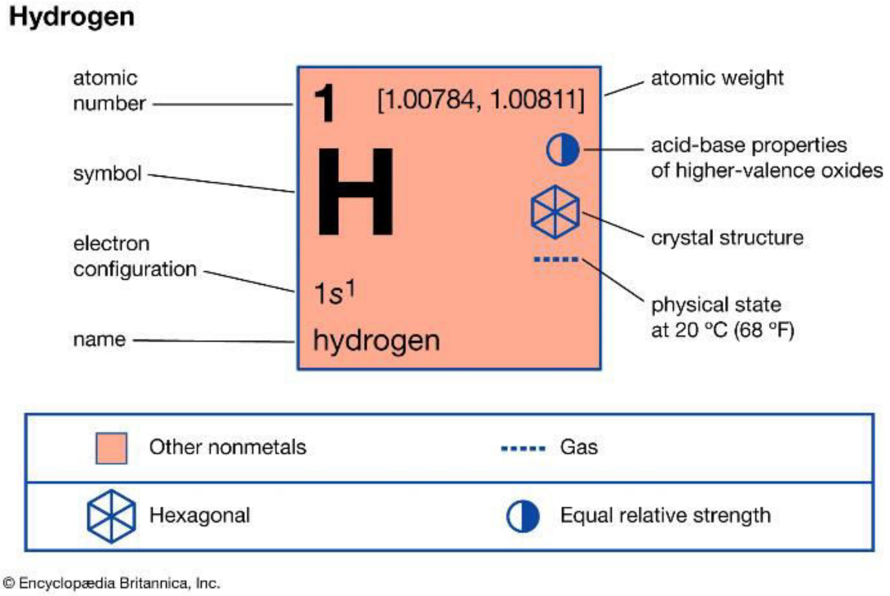

Figure 1. Chemical properties of hydrogen [6]

2.1 Hydrogen – metal interaction

2.1.1 Adsorption

Adsorption is defined as "the adhesion of atoms, ions, or molecules from a gas, liquid, or dissolved solid to a surface". The process is driven by the reduction in free energy as the adsorbate interacts with the substrate. The extent of adsorption is characterized by adsorption isotherms such as the Langmuir and Freundlich models [7], [8]. In many cases, the adsorption process is described by a heat of adsorption, which indicates the strength of the interaction between hydrogen and the metal surface. Kinetic barriers such as the activation energy for dissociation must be overcome in chemisorption, whereas physisorption occurs readily at low temperatures.

2.1.1.1 Physical adsorption

Physisorption occurs when hydrogen molecules (H_2) interact weakly with the metal surface via van der Waals forces. In this process hydrogen can easily desorb from the surface, making physisorption highly temperature-dependent, and so characterized by reversibility. The binding energy is low in this case, (typically in the range of 3 – 10 kJ/mol) which means that even modest thermal fluctuations can release the adsorbed hydrogen. Also, since it does not involve chemical bonding, physisorption is relatively insensitive to the chemical nature of the surface, though surface roughness and area play minor roles [7].

2.1.1.2 Chemical adsorption

Chemisorption involves the dissociation of hydrogen molecules into atoms, which then form strong chemical bonds with the metal surface. Chemisorption is characterized by irreversibility; under ambient conditions, chemisorbed hydrogen is often stable and requires significant energy to desorb. The chemical bonds formed are much stronger than the forces involved in physisorption (40–200 kJ/mol). Many metals (such as platinum or palladium) serve as catalysts that facilitate the dissociation of hydrogen molecules. The chemisorption process on these surfaces is critical for applications like hydrogenation reactions and fuel cells, where efficient hydrogen uptake is essential.

2.1.2 Absorption

Hydrogen absorption is defined as the uptake of hydrogen atoms into a metal's lattice, which occurs after the initial adsorption phase. Thermodynamically, the process is driven by the chemical potential difference between the hydrogen in the environment and the hydrogen dissolved in the metal. In many systems, hydrogen absorption follows Sieverts' law [9], which states that the concentration of dissolved hydrogen, C_H, is proportional to the square root of the hydrogen partial pressure, $P_{\{H_2\}}$:

$$C_H = S\sqrt{\{P_{\{H_2\}}\}} \tag{1}$$

where S is the solubility constant that depends on the material and temperature. This relation is fundamental for understanding how environmental conditions dictate the hydrogen content within a metal. Following chemisorption, hydrogen atoms penetrate the surface and dissolve into the metal lattice. In this stage, the atoms occupy interstitial sites (such as tetrahedral or octahedral positions) where the local environment and crystal structure determine the ease of dissolution. The extent of absorption is influenced by the lattice's free volume, the presence of oxide layers, and the material's intrinsic affinity for hydrogen.

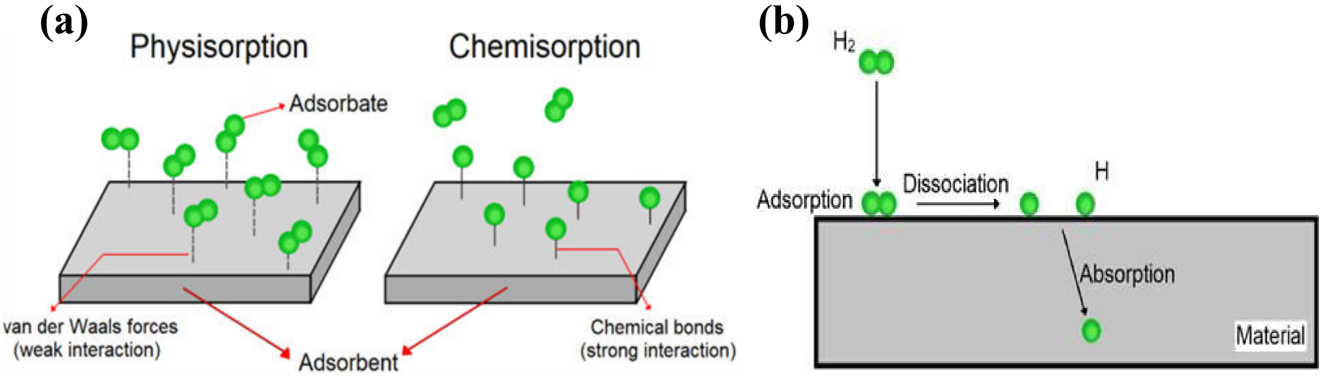

Figure 2. Schematic representation of the (**a**) adsorption and (**b**) absorption mechanisms

2.1.3 Diffusion

Diffusivity, or diffusion coefficient, (D) is a material property that quantifies the rate at which atoms or molecules move within a medium. In the context of metals, hydrogen diffusion is typically modelled using Fick's laws [10], [11]. The Fick's first law relates the diffusive flux J to the concentration gradient ∇C:

$$\mathrm{J} = -D \, \nabla \, C \tag{2}$$

while Fick's second law describes the time evolution of the concentration C:

$$\frac{\partial C}{\partial t} = \mathrm{D} \, \nabla^2 \, \mathrm{C} \tag{3}$$

These equations assume that diffusion is driven by thermal activation and concentration differences. In many experimental studies, hydrogen diffusivity is found to obey an Arrhenius-type relationship [11], [12]:

$$D = D_0 \exp\left(-\frac{E_a}{RT}\right) \tag{4}$$

where, D_0 is the pre-exponential factor, E_a is the activation energy for diffusion, R is the gas constant, and T is the absolute temperature. The value of this coefficient can be calculated experimentally by using the electrochemical permeation test [13].

Hydrogen diffuses predominantly via interstitial pathways because of its lower atomic radius. Within the metal lattice, two primary diffusion pathways are recognized: interstitial diffusion and quantum mechanical tunnelling [3]. Regarding the first one, hydrogen occupies small interstitial sites, typically octahedral or tetrahedral positions, in the metal lattice. The size and energy of these sites depend on the crystal structure (BCC, FCC or HCP). In body-centred cubic (BCC) metals such as pure iron, the proximity of adjacent interstitial sites facilitates higher diffusivity relative to close-packed structures.

Alloying elements can either enhance or hinder hydrogen diffusion. In high-entropy alloys (HEAs), the complex chemical environment can create a rugged energy landscape [14], often resulting in reduced hydrogen diffusivity due to local variations in the energies within the solid solution [15]. Cast materials often contain porosity and second-phase particles that act as trap sites, lowering the effective diffusivity. In contrast, wrought materials with controlled microstructures tend to exhibit "true" diffusivity values that are more predictable [16]. Phase composition is another important factor: dual-phase steels and duplex steel have different diffusivities according to phase present (ferrite/martensite for dual-phase and ferrite/austenite for duplex) [10], [17].

2.1.4 Trapping

Hydrogen atoms, owing to their extremely small size, not only diffuse rapidly through metallic lattices but also interact strongly with various microstructural defects. These interactions lead to the phenomenon known as hydrogen trapping. Traps, ranging from interstitial sites to defects such as dislocations, vacancies, and grain boundaries, capture hydrogen atoms and influence both its effective diffusivity and propensity to induce embrittlement. Trapping is crucial because it can retard diffusion and intensify hydrogen embrittlement by concentrating hydrogen at critical stress–concentration sites.

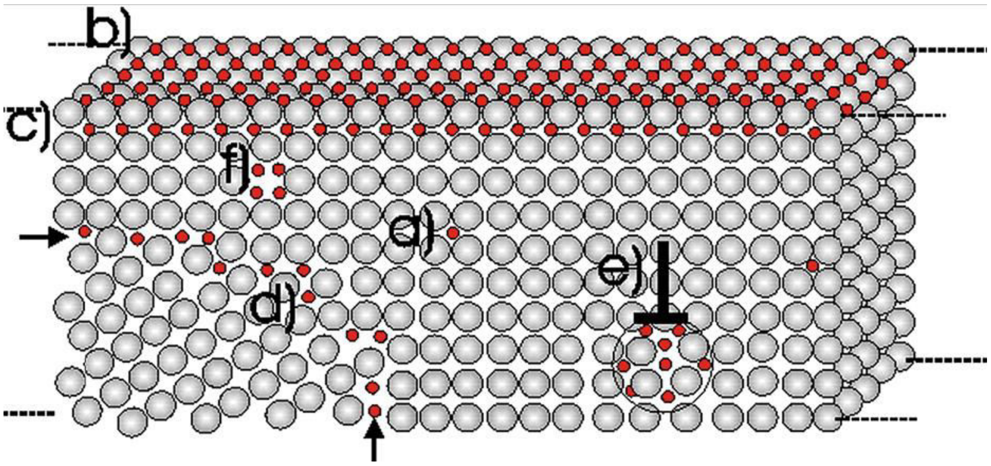

Figure 3. Schematic representation of hydrogen traps: a) interstitial sites; b) surface traps; c) subsurface traps; d) grain boundaries; e) dislocations; f) vacancies [9].

Hydrogen trapping refers to the phenomenon where hydrogen atoms become temporarily or permanently immobilized at microstructural defects. The degree of trapping is characterized by a trap binding energy, E_b, which represents the energy difference between a hydrogen atom in a regular interstitial site and one occupying a trap site. E_b can also be seen as the difference of detrapping E_d and trapping activation energy E_t ($E_b = E_d - E_t$) [18], [19]. This energy governs whether hydrogen can be released (detrapped) during thermal or mechanical loading. In many models, the overall hydrogen concentration C in a metal is expressed as the sum of the lattice (or "diffusible") hydrogen C_L and the trapped hydrogen C_T:

$$C = C_L + C_T \tag{5}$$

The trapping/detrapping kinetics are typically modelled using Oriani's equilibrium theory [20], where the occupancy of traps is described by[18]:

$$\frac{C_T}{N_T - C_T} = \frac{C_L}{N_L} \, exp\left(\frac{E_b}{RT}\right) \tag{6}$$

where N_T being the total trap density, N_L is the total lattice site density, R the gas constant, and T the absolute temperature.

Traps can be broadly classified into two categories: reversible and irreversible (deep) traps [9], [21]. The first ones refer to low-energy sites (e.g., interstitial sites near dislocations or small precipitates), lower than the self-diffusion activation energy of hydrogen in the lattice, allowing hydrogen to detrap and re-enter the lattice at relatively low temperatures [22]. They affect the effective diffusivity but allow hydrogen to eventually contribute to embrittlement under stress. In particular, the strain fields around dislocations provide energetically favourable sites for hydrogen. Hydrogen decoration at dislocations can lead to stress shielding effects and promote localized plasticity. The latter refer to sites such as vacancy clusters, non-metallic inclusions, or interfaces where the binding energy is high enough to prevent hydrogen from detaching under normal service conditions. Although these traps reduce the concentration of diffusible hydrogen, they can also serve as nucleation sites for voids and microcracks. Vacancies offer open volumes that can host hydrogen. Moreover, hydrogen may lower the formation energy of vacancies (a concept described by different theories, such as the HESIV theory [23] and the "defectant theory" [10]), leading to enhanced vacancy concentrations that facilitate trap formation. Grain boundaries, phase boundaries, and precipitate interfaces typically have disrupted atomic arrangements, which can serve as deep traps. These sites are often implicated in intergranular fracture mechanisms. In multiphase alloys, the interfaces between the matrix and secondary phases (or inclusions) act as trapping sites.

Hydrogen trapping plays a dual role in embrittlement: irreversible traps can reduce the concentration of diffusible hydrogen, potentially delaying the onset of embrittlement under service conditions. Conversely, when reversible traps are saturated, the local accumulation of hydrogen at stress concentrators can lead to crack initiation and propagation. The interplay between trap density, binding energy, and applied stress determines the critical conditions for delayed fracture. The spatial distribution of traps is particularly important in high-strength alloys. For instance, in steels, the heterogeneity of trap sites across grain boundaries, dislocation networks, and precipitates is a major factor in localized hydrogen-induced cracking. Face-centred cubic (FCC) structures tend to have lower hydrogen diffusivity and may exhibit different trapping dynamics compared to body-centred cubic (BCC) steels. In pure metals, trapping is generally limited to intrinsic defects such as vacancies or dislocations induced by processing.

A variety of techniques are used to characterize hydrogen trapping. TDS measures the rate of hydrogen release as a function of temperature. The resulting desorption spectra provide information on trap binding energies and densities. By monitoring hydrogen permeation under controlled charging and discharging conditions, one can infer the influence of traps on effective diffusivity. APT offers near-atomic resolution mapping of hydrogen distributions, enabling direct visualization of hydrogen segregation at defects.

3. Hydrogen embrittlement mechanisms

3.1 Hydrogen pressure theory

The hydrogen pressure theory, also referred to as high-pressure bubble formation mechanism [24], originally proposed by Zapffe [25] in 1941, offers a mechanistic explanation for hydrogen embrittlement by focusing on the accumulation and recombination of hydrogen at microstructural defects within metals. According to this theory, atomic hydrogen, which diffuses rapidly through the metal lattice due to its extremely small size, tends to segregate at energetically favourable sites such as micropores, inclusions, and pre-existing microcracks. At these defect sites, hydrogen atoms recombine to form molecular hydrogen (H_2), a process that inherently involves a volumetric expansion since H_2 occupies significantly more space than individual hydrogen atoms. This recombination leads to a localized, high internal gas pressure, which, if it exceeds the local yield strength of the material, can induce the nucleation and propagation of microvoids and cracks. The theory posits that it is not merely the presence of dissolved hydrogen that weakens the metal, but rather the high-pressure build-up generated by the formation of molecular hydrogen at discrete sites that causes embrittlement. In Fig. 4 a schematic representation of this theory is shown.

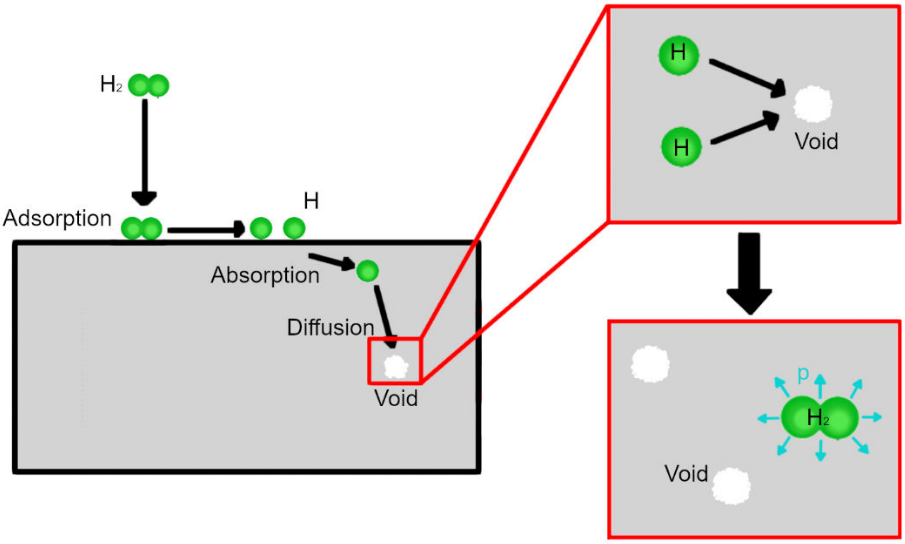

Figure 4. Schematic representation of the hydrogen pressure theory

"Fish-eye" damage in the steels [9], hydrogen-induced cracking and blistering [26] of pipeline steels in the H_2S environment, can be explained by the hydrogen pressure theory.

3.2 Hydrogen-Induced Phase Transformation (HIPT)

This theory was firstly proposed by Westlake in 1969 [27]. The hydrogen-induced phase transformation refers to a phenomenon in which the ingress of hydrogen into a metal drives a change in its crystallographic structure, typically resulting in the formation of a hydride phase that is often markedly more brittle than the parent phase. Due to their high bond energies, certain metals, such as Ti, Zr, Nb, V, and Ta [9], [28], readily react with hydrogen to form brittle hydrides. Based on the hydrogen concentration in the alloys, hydrides can be categorized as either spontaneously formed or stress-induced. At high hydrogen concentrations, hydrogen directly reacts with specific metals to form hydrides without external stress. In contrast, when the initial hydrogen concentration is low, a stress gradient redistributes the hydrogen, leading to the formation of stress-induced hydrides [9]. These hydrides obstruct dislocation movement and lead to stress concentration at crack tips. Once the local hydrogen concentration reaches the solubility of metal, hydrides are precipitated. The presence of stress concentrations further facilitates hydride formation due to the hydrogen atoms from decomposed hydrides diffusing towards them, thereby promoting the continuous growth of cracks into brittle fractures.

The mechanism behind the failure due to the presence of hydride is well established (Fig. 5) and can be summarized in four step: (1) hydrogen diffusion to regions of high hydrostatic stress ahead of crack tips; (2) nucleation and growth of a hydride phase, (3) cleavage of the hydride when it reaches a critical size, and (4) crack arrest at the hydride [9].

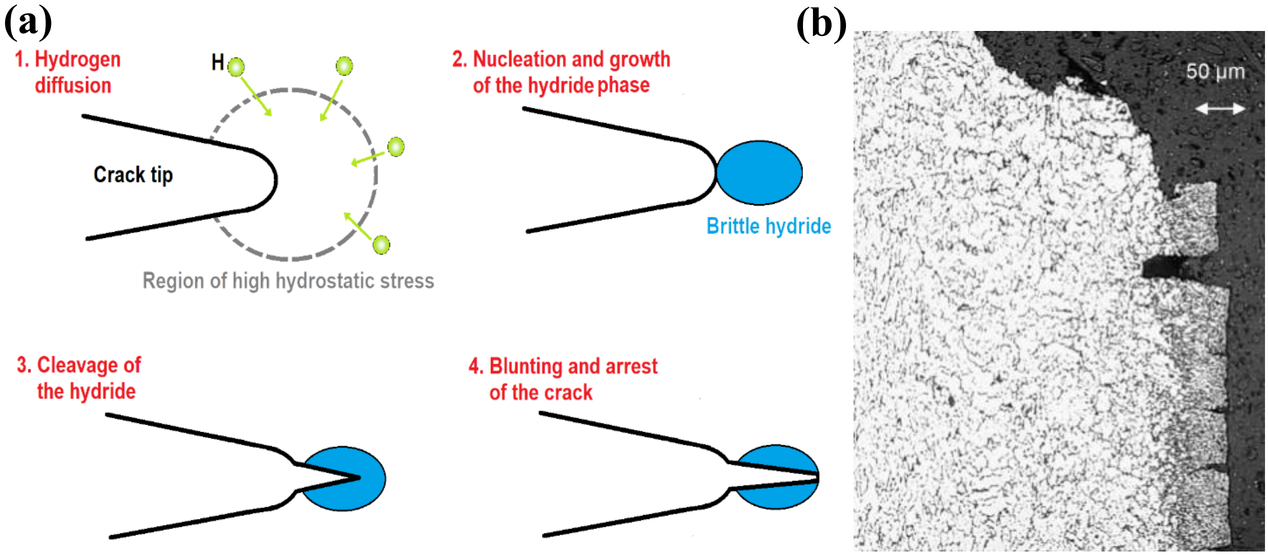

Figure 5. (**a**) Schematic representation of the HIPT mechanism and (**b**) hydride layer and secondary crack on the lateral surface of a Ti Gr-12 specimen [29].

3.3 Hydrogen Enhanced Decohesion (HEDE)

Hydrogen-enhanced decohesion (HEDE) theory is one of the first concepts proposed in the study of hydrogen embrittlement. It postulates the reduction of interatomic cohesion as the primary driver of brittle failure in metals exposed to hydrogen. Originally proposed by Pfeil et al. in 1926 [30] and later refined by others researchers such as Troiano in the late 1950s [31], HEDE suggests that when hydrogen atoms, owing to their small size and high diffusivity, enter a metal, they preferentially accumulate at regions of high tensile stress, such as crack tips, grain boundaries, and other defect sites.

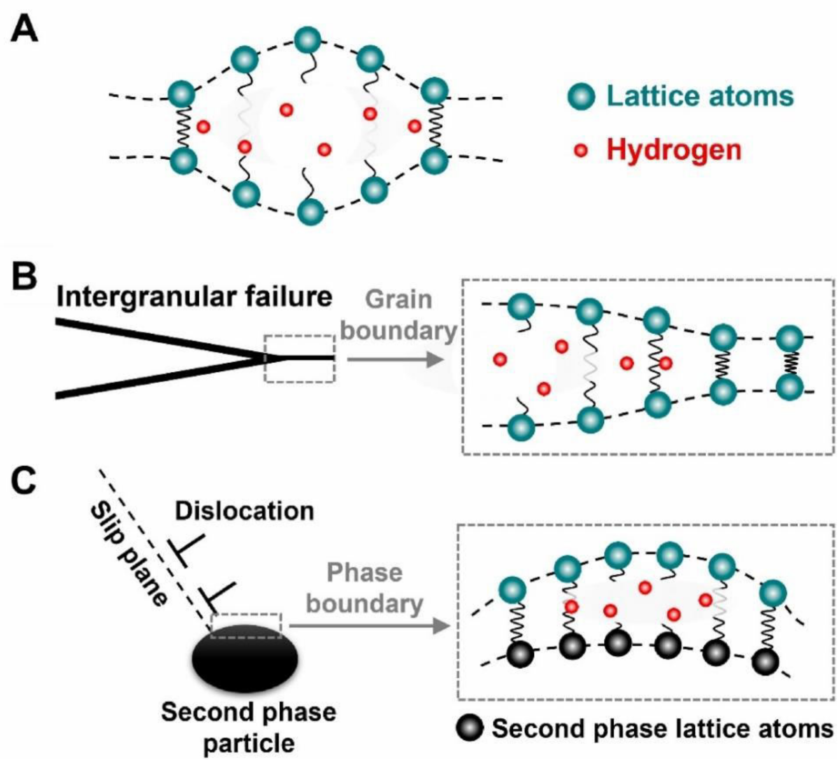

Figure 6. Schematic representation of the HEDE mechanism [32]

At these locations, hydrogen is believed to interfere with the metallic bonding by entering interstitial sites and, in some cases, by transferring its electron to partially fill the unoccupied d-orbitals of the metal atoms. This electronic interaction effectively reduces the cohesive energy of the lattice, thereby lowering the stress required to break atomic bonds and initiate crack propagation. The value of this stress depends on the hydrogen concentration and can be described as [9]:

$$\sigma_{cH} = \sigma_{c0} - \beta C \tag{7}$$

where σ_{cH} is the locally critical cohesive stress at the specific hydrogen concentration C, σ_{c0} is the critical cohesive stress without hydrogen and β is a related parameter for the loss of critical cohesive stress due to hydrogen.

3.4 Hydrogen enhanced local plasticity (HELP)

According to the HELP theory, hydrogen atoms that are absorbed into the metallic lattice preferentially accumulate at stress concentrators, such as crack tips, grain boundaries, and dislocation cores, where they significantly lower the energy barriers for dislocation nucleation and motion. This reduction in activation energy facilitates enhanced dislocation mobility even at relatively low applied stresses, leading to highly localized plastic deformation [33] in a plastic zone that is smaller than normally present in ahead of the crack tip. This results in less blunting of the crack tip, and consequently less reduction of the stress field, that causes the eventual initiation and propagation of cracks under loading conditions where the material should not fail, resulting in the presence of smaller and shallower microvoids.

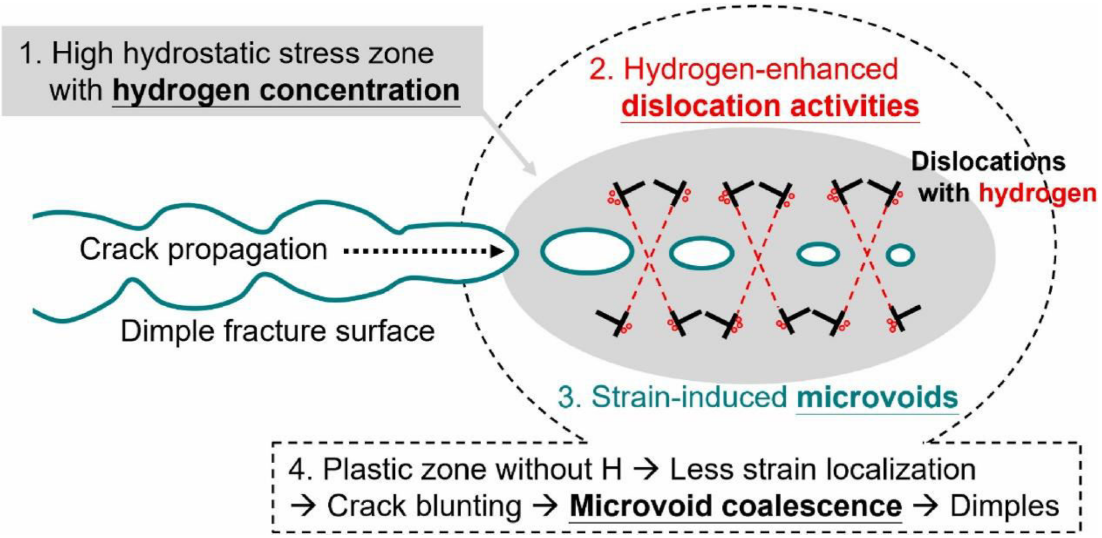

Figure 7. Schematic representation of the HELP mechanism [34]

3.5 Adsorption-induced dislocation emission (AIDE)

According to AIDE, when hydrogen atoms from the environment are adsorbed onto the highly stressed regions at crack tips or grain boundaries, they alter the local electronic structure and reduce the interatomic bond strength. This reduction lowers the energy barrier for dislocation nucleation and emission, effectively “activating” dislocation motion in areas where, under hydrogen-free conditions, dislocation generation would require substantially higher applied stresses. In this way, AIDE combines essential features of both hydrogen-enhanced decohesion (HEDE) and hydrogen-enhanced localized plasticity (HELP): on one hand, the presence of hydrogen weakens the cohesive forces across interfaces, while on the other, it promotes localized plasticity by easing dislocation emission and movement predisposing the material to crack initiation and propagation [33].

3.6 Hydrogen Enhanced Strain-Induced Vacancy (HESIV)

The HESIV theory represents a “newer” approach for the study of hydrogen embrittlement, mainly for steels, developed in the early 2000s [23]. This theory posits that the presence of hydrogen significantly lowers the energy barrier for vacancy formation, thereby enhancing the creation and clustering of strain-induced vacancies [9], [35]. In this framework, hydrogen atoms, occupying interstitial sites during deformation, facilitate the formation of vacancies that would otherwise require higher activation energies in a hydrogen-free environment. These vacancies tend to agglomerate into nanoscale clusters that can serve as nucleation sites for microvoids, which eventually coalesce and lead to either a ductile failure by microvoid coalescence or a quasi-cleavage fracture mode depending on the local stress state [10]. In Fig. 8 a schematic representation of the HESIV theory is shown.

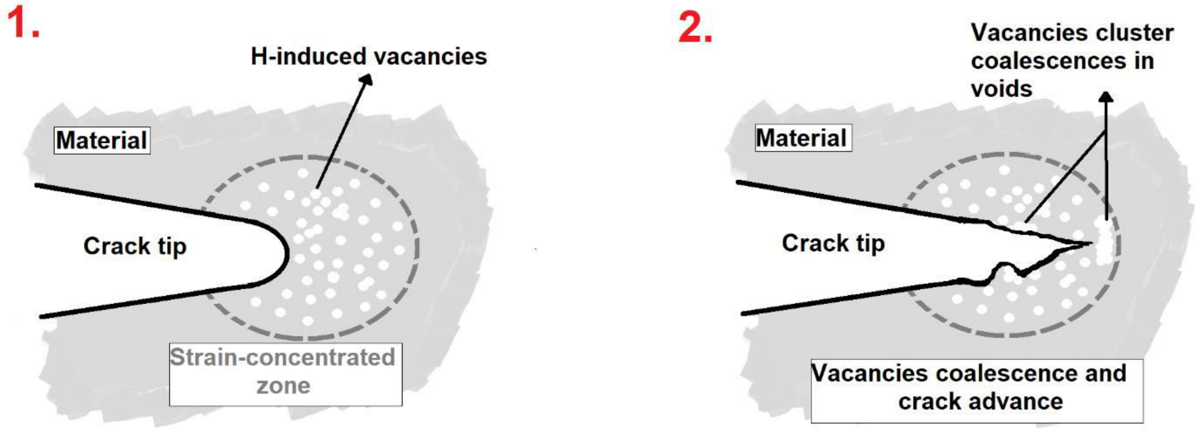

Figure 8. Schematic representation of the HESIV mechanism

3.7 Synergistic effects of HE mechanisms

Recent models [36] advocate a unified perspective in which these two mechanisms operate synergistically, HEDE initiates embrittlement by reducing interatomic cohesion, while HELP exacerbates it by redistributing plastic strain and concentrating deformation at critical regions, effectively lowering the stress threshold for crack initiation [37]. This new proposed model state that at low [H] concentrations, mechanism such as HELP, AIDE, and in general plasticity-enhanced mechanisms are the ones responsible for hydrogen embrittlement, that leads to ductile-like fracture. Increasing the [H] concentration leads to “local decohesion incidents” [38] in spots of the microstructure where the [H] concentration as surpassed a critical C_H concentration, triggering the HEDE mechanism in the form of intragranular microcracks and micro fissures. Interatomic decohesion, due to the HEDE mechanism, is triggered at high [H] concentration, leading to brittle intergranular and transgranular fracture. The simultaneous effects of the two mechanisms can be seen around the C_H critical concentration. In this case, the term "quasi-cleavage” fracture is used to describe a mix of different fracture modes in the ductile-brittle transition, such as transgranular/intergranular brittle fracture due to HEDE mechanism and microvoid coalescence (ductile) fracture due to HELP mechanism [36], [39].

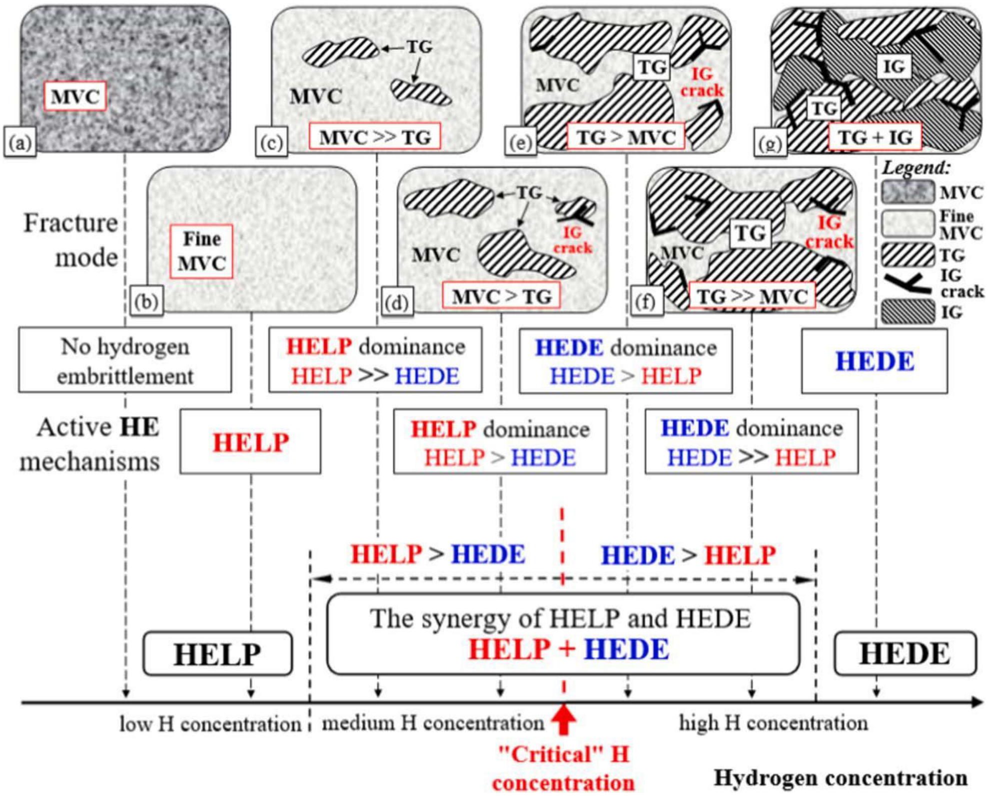

Figure 9. Failure modes of different HE mechanisms as a function of the hydrogen concentration [38]

The HELP+HEDE theory has been confirmed for several materials, such as steel, iron, aluminium alloys and nickel alloys, both experimentally and modelling [37], [40]. The unified HELP+HEDE theory has several key limitations that persist to this day: one of the principal challenges is the lack of experimental techniques capable of measuring local hydrogen concentrations at the Nano or atomic scale in situ. This makes it difficult to verify the assumed threshold concentrations that trigger the transition from HELP-dominated behaviour (enhanced dislocation mobility) to HEDE-dominated behaviour (reduced cohesive strength) reliably [37], [40]. In addition, although the theory suggests a synergistic operation of HELP and HEDE, the relative contribution of each mechanism under varying conditions (e.g., different strain rates, temperatures, and microstructures) is still not clearly defined. The precise conditions under which one mechanism dominates over the other remain ambiguous [36].

4. Hydrogen embrittlement in steel

Steel remains the backbone of modern infrastructure and high-performance engineering applications. However, the ingress of hydrogen, either during processing or in service, can lead to catastrophic failures due to hydrogen embrittlement (HE). Hydrogen is highly mobile in steel due to its small atomic radius. It typically diffuses via interstitial sites in the crystal lattice. In body-centred cubic (BCC) steels, tetrahedral sites are preferred due to their larger free volume, whereas in face-centred cubic (FCC) austenitic steels, octahedral sites often dominate. The solubility of hydrogen in steel is influenced by temperature and alloy composition, and it tends to be low [10], [41], on the order of ppm, but even these concentrations can be critical when coupled with mechanical stresses.

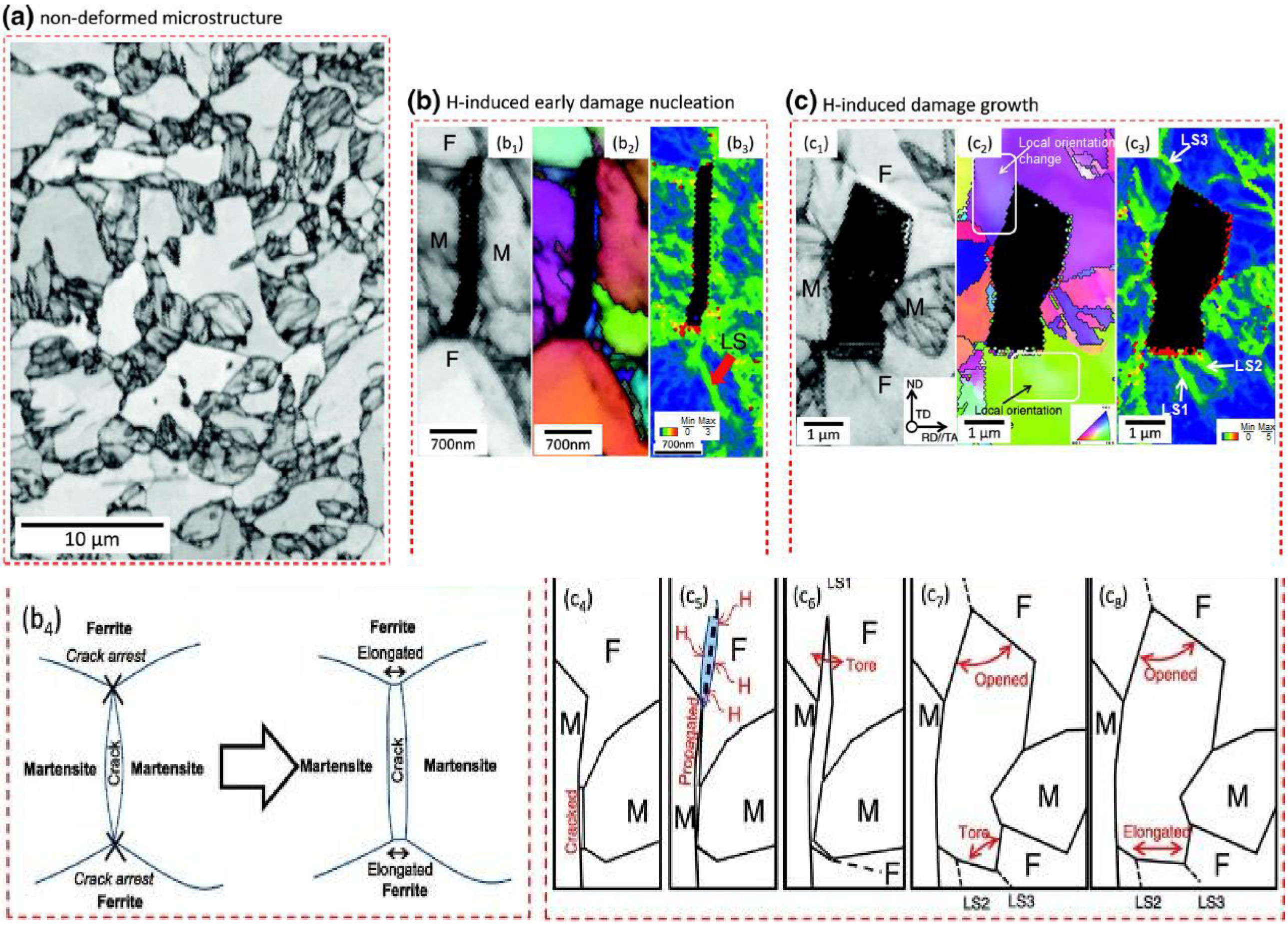

Figure 10. (**a**) EBSD image quality (IQ) map showing the initial non-deformed microstructure of DP steel; (**b**) EBSD IQ, inverse polar figure (IPF) and kernel average map (KAM) **b1-b3** and schematic diagrams **b4** showing the H-induced crack nucleation at prior-austenite grain boundaries; (**c**) EBSD results **c1-c3** and schematic diagrams **c4-c8** showing the H-induced crack propagation inside ferrite. Adapted from [34].

The manifestation of HE is often observed in the fracture behaviour of steel. Cracks propagate along weakened grain boundaries due to localized hydrogen accumulation and decohesion effects, causing intergranular fracture. In some cases, crack propagation occurs through grains, typically when the HELP mechanism is dominant, making the material fail by transgranular fracture. Under cyclic loading or in the presence of a high density of vacancies, microvoids can nucleate and coalesce, leading to a mixed-mode fracture that exhibits features of both ductile and brittle failure.

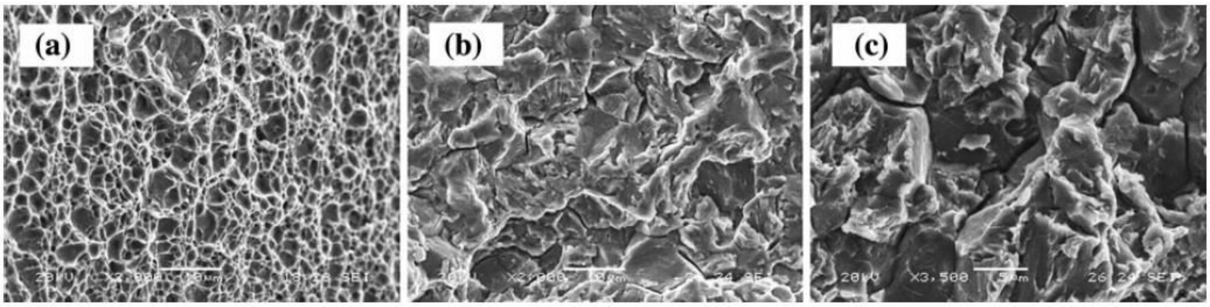

Figure 11. Micrographs of fracture surface of M 1400 steel samples charged with different hydrogen contents. (**a**) Uncharged specimen, (**b**) sample electrochemically charged at 1.2 ppm, and (**c**) sample electrochemically charged at 2.7 ppm [42].

The transition from ductile to brittle behaviour is strongly influenced by local hydrogen concentration, applied stress, strain rate, and microstructural features such as grain size and phase distribution.

5. Hydrogen embrittlement in aluminium

Aluminium is a material of choice in many industries due to its lightweight, high thermal conductivity, and excellent resistance to corrosion. These characteristics made aluminium suitable for hydrogen storage applications, both gaseous and liquid methods [10]. Aluminium and its alloys generally show a much lower susceptibility to hydrogen embrittlement [43], [44]. This reduced sensitivity is primarily attributed to aluminium's rapid formation of a protective oxide layer (Al_2O_3), which limits hydrogen uptake under dry conditions. This implies that the hydrogen uptake is almost absent under conditions where hydrogen is present only in gaseous form, e.g., in service and during gaseous hydrogen charging. It has been proven using the parameter RRA [44] , relative reduction of area, defined as:

$$RRA = \frac{\phi_0}{\phi_H} \tag{8}$$

where ϕ_0 is the reduction of area in air after a SSRT and ϕ_H is the reduction of area in hydrogen environment or after hydrogen charging after a SSRT. Aluminium alloys present a value of RRA close and even greater than 1 [35].

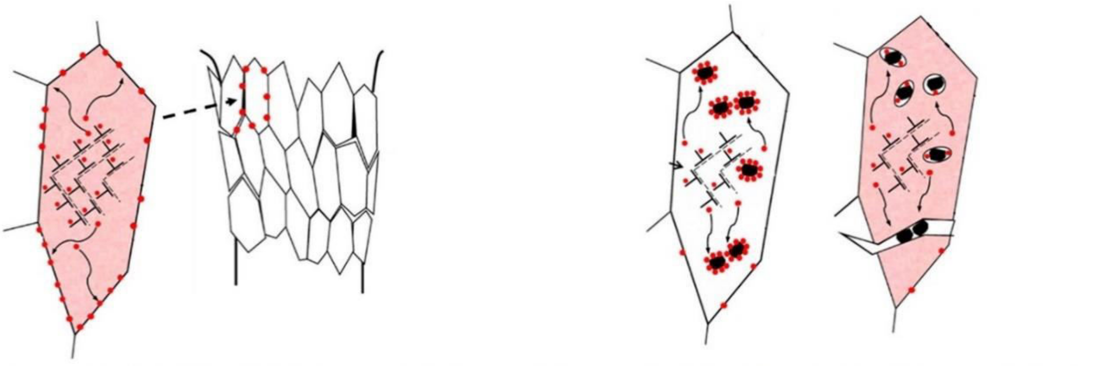

(a) H segregation to GBs leading to intergranular fracture (b) H segregation to inclusions leading to transgranular fracture

Figure 12. Schematic representation of the HE mechanisms for IG and TG fracture in a 7xxx series aluminium alloy [10]

Although the solubility of hydrogen in aluminium is relatively low compared to steels, certain processing conditions, e.g., welding (porosity), casting, or working conditions where aluminium alloy is exposed to moisture [45], high temperatures [46] or when the protective film is disrupted, can lead to local accumulation of hydrogen. Once present, hydrogen can interact with microstructural features such as dislocations, grain boundaries, and second-phase particles [47], ultimately triggering embrittlement.

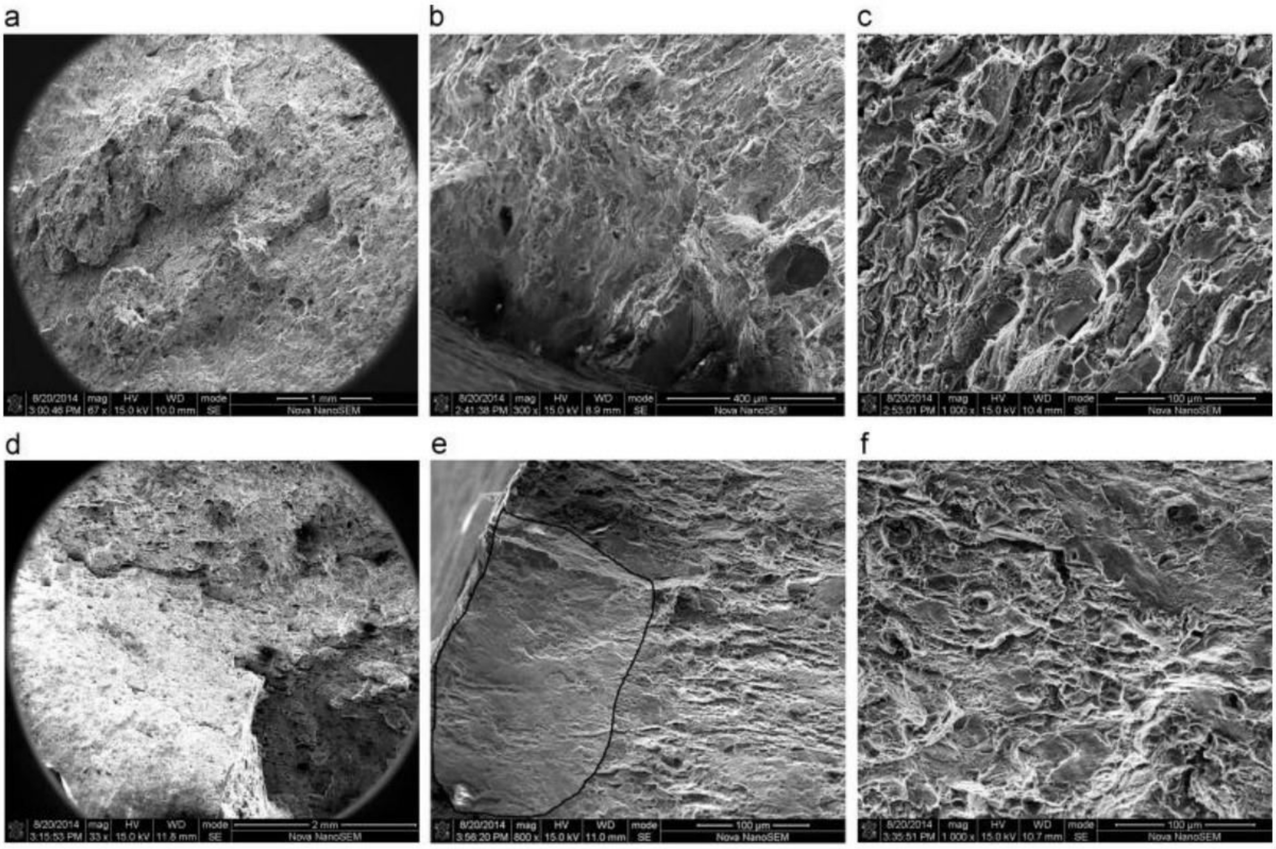

Figure 13. Fractographs of 7075 Aluminium alloy samples tested in 0.01 M NaOH with hydrogenation at a strain rate of 10^{-4} s^{-1}. I_c = 1 mA/cm^2 for **a**, **b** and **c**; I_c = 5 mA/cm^2 for **d**, **e** and **f** [48].

High-strength aluminium alloys, such as the 7xxx series and even some 2xxx series, are mostly affected by HE, as is to be expected from high-strength materials [49], [50], [51]. They present a reduction of ductility, typical of the high-strength materials affected by HE. Compared to other reviewed types of aluminium alloy, the 6xxx series alloys are considered to have good HE resistance[52], [53]. Improving an aluminium 7xxx alloy's resistance to hydrogen embrittlement can be achieved by reducing hydrogen segregation at its grain boundaries[10]. One effective strategy is to introduce precipitates or second-phase particles [54] within the grains that can trap hydrogen more efficiently, thereby promoting a more favourable distribution of hydrogen. So, hydrogen embrittlement also affects aluminium and its alloys, albeit to a far lesser extent than more susceptible metals and under specific working conditions. The limit, on the other hand, is the low strength, that make them not suitable for high-stress components.

6. Techniques to measure hydrogen embrittlement

6.1 Hydrogen charging

6.1.1 Electrochemical (cathodic) charging

Electrochemical hydrogen charging, also known as cathodic hydrogen charging, is a widely used method for introducing hydrogen into materials, particularly metals, and alloys. This technique applies an electrochemical process in which the material under investigation is subjected to a cathodic potential, causing protons (H^+) in the electrolyte to be reduced to atomic hydrogen (H) at the metal-electrolyte interface. This atomic hydrogen then diffuses into the material, mimicking the hydrogen ingress that occurs in real-world environments, such as from corrosion processes or during cathodic protection scenarios

Post-charging analysis techniques such as thermal desorption spectroscopy (TDS), scanning electron microscopy (SEM), and transmission electron microscopy (TEM) are frequently employed to visualize the hydrogen concentration or examine potential formation of micro cracks and voids.

6.1.2 Gaseous charging

Gaseous charging involves exposing a material to high-pressure hydrogen gas, where molecular hydrogen is dissociated at the surface (often by catalytic action) and then diffuses into the material. The specimen is placed in a high-pressure vessel filled with hydrogen gas. The pressure is elevated to levels sufficient to promote hydrogen absorption, and temperature may be adjusted to enhance diffusion. Over time, hydrogen is absorbed into the specimen, simulating service environments like hydrogen pipelines or storage vessels. It's suitable for charging larger specimens or components. High-pressure systems require robust, high-cost equipment and strict safety protocols. In some cases, a catalyst is required to effectively dissociate hydrogen molecules, adding to system complexity. Like the electrochemical charging, several mechanical test can be done during a gaseous charging, in such a way as to simulate what the actual working conditions may be. High-pressure gaseous charging requires stringent safety protocols to manage risks of leaks, explosions, or material failure. Operators must adhere to detailed standards and use specialized equipment to minimize these hazards.

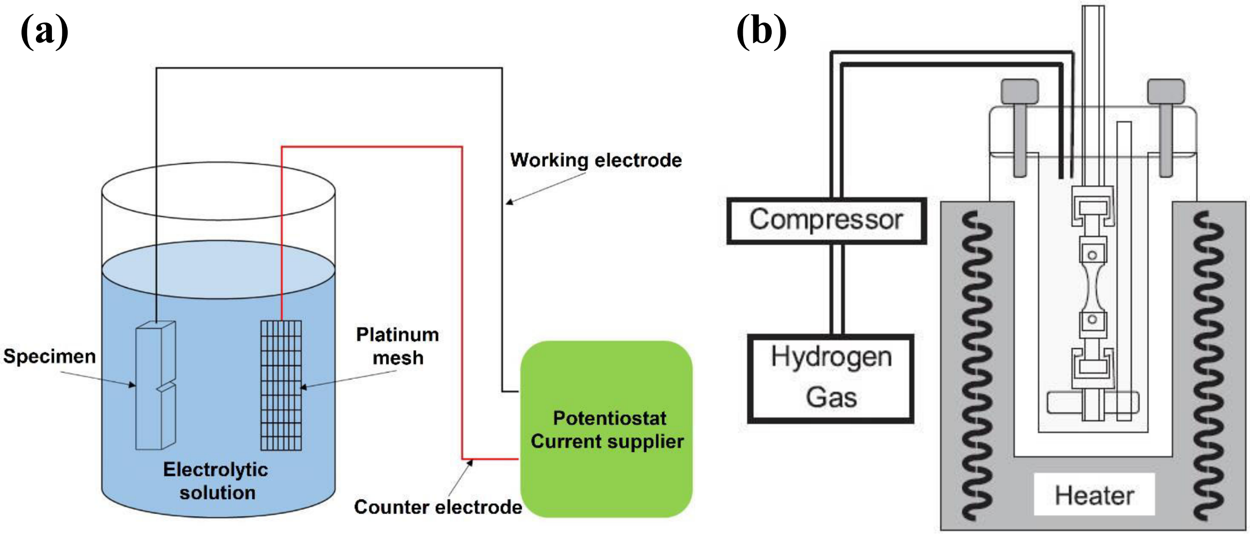

Figure 14. Schematic representation of (**a**) the cathodic hydrogen charging [55] and (**b**) the SSRT performed during the gaseous charging [56].

6.2 Mechanical testing methods

The HE susceptibility of different materials is usually assessed with mechanical testing. Besides the slow strain rate test (SSRT), different other techniques, such as the constant load test (CLT), the rising step loading test (RSLT) are appropriate in most cases. Typically, these tests are performed for hydrogen-free and hydrogen-charged specimens and then the results are compared to assess the influence of hydrogen on mechanical properties, like yield strength, tensile strength and elongation [13].

6.2.1 Slow strain rate rest (SSRT)

Slow strain rate testing (SSRT) has emerged as a powerful experimental technique for evaluating the susceptibility of materials to hydrogen embrittlement because it enables hydrogen diffusion into the specimen during deformation. By loading specimens at very low strain rates, SSRT replicates the conditions under which hydrogen-induced damage can accumulate, thereby serving as a screening tool to rank material performance in hydrogen-rich environments. SSRT involves performing a uniaxial tensile test at a constant, low strain rate (commonly 10^{-5} s^{-1} or lower). This slow deformation rate is used because hydrogen has sufficient time to diffuse from the surface or an in situ charging source into the metal lattice and interact with microstructural features such as dislocations, grain boundaries, and precipitates [13]. Extended exposure at low strain rates can enable sub-critical crack initiation and propagation before final fracture. SSRT metrics, such as time-to-failure, elongation, and reduction in area, are used to quantify the degree of embrittlement. A significant reduction in ductility in a hydrogen environment relative to a hydrogen-free reference indicates high susceptibility to HE. Specimens for SSRT are typically prepared in geometries standardized by ASTM G129 [57] and ISO 7539-7 [58].

6.3 Thermal testing methods

6.3.1 Temperature desorption spectroscopy (TDS)

Thermal desorption spectroscopy (TDS) is a powerful, non-isothermal analytical technique widely employed to quantitatively measure hydrogen in solids, particularly in metals and alloys where hydrogen trapping significantly influences mechanical properties and material performance. In a typical TDS experiment, a hydrogen charged sample is placed in an ultra-high vacuum chamber and subjected to a controlled, programmable temperature ramp, which induces the release of hydrogen from its various trapping sites; these sites may include interstitial lattice positions, dislocations, grain boundaries, microvoids, and precipitate interfaces. As the sample heats, hydrogen desorbs at characteristic temperatures that reflect the binding energies of these traps, and the evolved hydrogen is monitored in real time by a quadrupole mass spectrometer, often yielding a desorption spectrum with multiple peaks corresponding to different trap strengths [59], [60]. In Fig. 15 a schematic of TDS setting is shown.

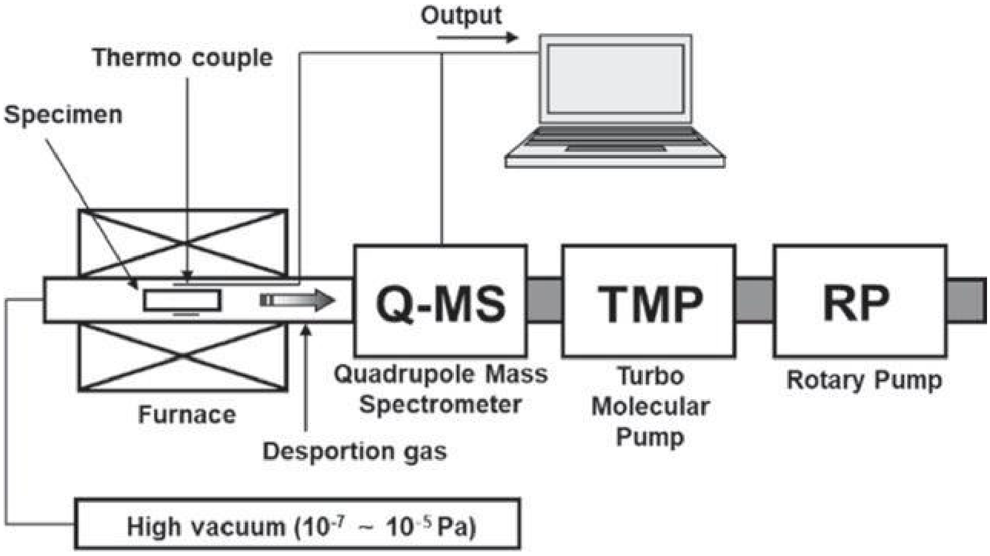

Figure 15. Schematic representation of TDS apparatus [61]

This spectrum not only allows for the accurate quantification of total hydrogen content, often with detection limits in the low ng/g range when properly calibrated [59], [62], but also provides valuable kinetic and thermodynamic data on the hydrogen–material interactions. Owing to its sensitivity and selectivity, TDS has become an indispensable tool in research areas such as hydrogen embrittlement studies, hydrogen storage material development, and catalyst performance evaluation, where understanding the dynamics of hydrogen uptake, diffusion, and release is critical.

6.4 Microscopic and surface analysis methods

6.4.1 Microstructural analysis

Microstructural analysis plays a critical role in unravelling the mechanisms of HE by providing detailed insights into the morphological, crystallographic, and chemical changes induced by hydrogen. The embrittlement process is inherently microstructural: hydrogen interacts with defects and phase boundaries, leading to localized weakening and eventual fracture. To fully understand and mitigate HE, it is essential to examine the microstructure at multiple length scales. Advanced microstructural analysis techniques have become indispensable in this research, offering high-resolution insights into how hydrogen influences dislocation motion, void formation, and crack propagation. Heterogeneous microstructures can lead to uneven hydrogen distribution. Regions with high defect densities are more susceptible to hydrogen accumulation, resulting in localized plasticity and premature crack initiation. Mapping these heterogeneities helps in correlating microstructural characteristics with macroscopic mechanical behaviour [63].

Different techniques are used to study the microstructure of materials. Besides the classic optical microscopy (OM), the most used techniques are scanning electron microscopy (SEM) and transmission electron microscopy (TEM).

6.4.1.1 Scanning electron microscope (SEM)

It is widely used to examine fracture surfaces and cross-sectional morphologies. It reveals features such as brittle cleavage facets, microvoid coalescence, and the presence of secondary cracks. Detailed examination of fracture surfaces often identifies characteristic patterns (e.g., intergranular or quasi-cleavage fractures) associated with HE. SEM operates by scanning the surface of a sample with a focused beam of electrons. These electrons interact with the atoms in the sample, generating various signals including secondary electrons, primarily used for imaging surface morphology with high spatial resolution, backscattered electrons, that provide compositional contrast based on differences in atomic number, and characteristic X-rays [64], [65]. The intensity and energy distribution of these signals provide detailed information about the surface topography, composition, and crystallographic orientation. The specific signals can be used for different SEM-techniques, for example Energy Dispersive X-ray Spectroscopy (EDS) attached to SEM enable elemental analysis. Electron backscatter diffraction (EBSD) it's used to study the crystallographic structure of materials.

6.4.1.2 Transmission electron microscope (TEM)

Provides high-resolution images of dislocation structures, phase boundaries, and nanoscale precipitates. In situ TEM has been particularly useful for observing dislocation movements, hydrogen-induced slip bands and the early stages of void formation, due to hydrogen-stabilized vacancies, that is correlated with regions of localized plasticity. TEM operates by transmitting a highly focused beam of electrons through a thin specimen. The interactions between the electrons and the sample's atoms produce various signals, including transmitted electrons, diffracted electrons, and characteristic X-rays, that are collected to form images and diffraction patterns.

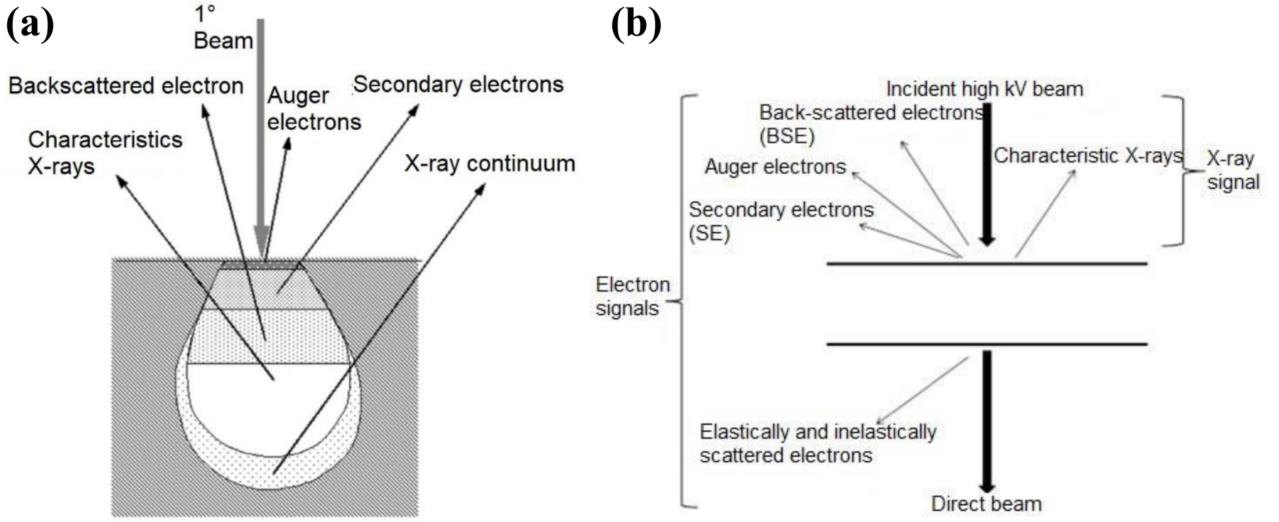

Figure 16. Types of signals emitted from the specimen surface while hit with the beam of electrons in (**a**) SEM [64] and (**b**) TEM [66].

7. Hydrogen embrittlement prevention

Prevention of hydrogen embrittlement can be considered based on several approaches and various aspects such as materials engineering, process control, surface modification, and rigorous quality assurance [9]. This needs to be done to effectively minimize hydrogen ingress and its subsequent deleterious effects on structural integrity. Among the aspects to be considered, where the hydrogen comes from and the mechanism acting in the material are the most important.

7.1 Surface treatments

7.1.1 Surface coating

Different materials are used for surface coatings: Ni, Cd, Al and some complex films such as Al–Ni, Zi-Cd and Ti-Cd can effectively reduce hydrogen infusion, in order to lower the susceptibility to HE. In addition to the elements already mentioned, in steels Ag, Au and Cu have been proved to be effective in opposing the diffusion of hydrogen within the material. Oxides and corrosion products formed on the surface can also act as barrier to hydrogen entry [48], [67], [68]. A key aspect to consider is that the film used must be suitable for that material and it must have appropriate mechanical properties to ensure effective protection.

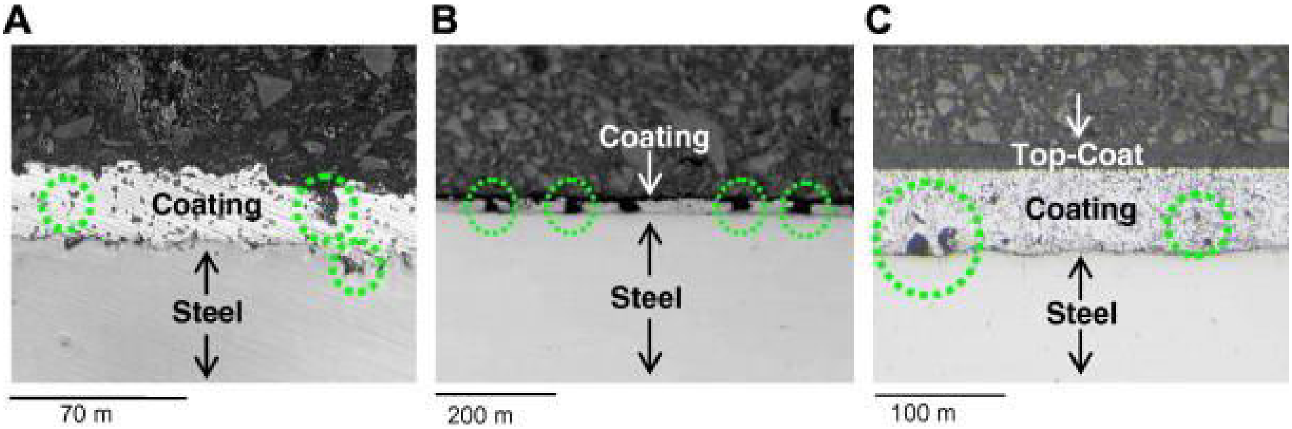

Figure 17. Cross-sections through the coatings showing: (**A**) closed pores in the cadmium; (**B**) through-thickness pores in the zinc–14% nickel and (**C**) closed pores in the SermeTel 1140/962 (circles indicate major discontinuities in the coating) [69].

7.1.2 Surface modification treatments

Several surface modification treatments help enhancing the HE resistance. For example, in surface nitriding and carbonization treatments respectively, the presence of interstitial nitrogen and carbon cause a compressive stress that reduce the lattice spacing, thus preventing the entry of hydrogen. Also, they can stabilize the austenite phase, since austenite is generally less susceptible to hydrogen embrittlement because its face-centred cubic (FCC) crystal structure results in lower hydrogen diffusivity [9]. A similar compressive stress can be achieved by surface peening treatment, which also increases the density of the hydrogen trap sites.

7.2 Modification of the material microstructure

The choice of alloying elements is important. For example, the addition of Mo and Ti reduces the segregation of P at grain boundaries, which would embrittlement them [70] and could cause internal blistering [67]. In addition, Mo, Ti and V are used to form carbides with C, which are irreversible traps for hydrogen and consequently reduce its diffusivity within the material. As for steels, the preferred choice is to use austenitic steels, as these are the ones with lower susceptibility to hydrogen embrittlement than martensitic or bainitic steels [9]. Advanced alloying strategies, such as the introduction of chemical heterogeneity within the microstructure (for example, by dispersing Mn-rich zones in high-strength steels), can serve as local traps that arrest crack propagation and interrupt the embrittlement process without sacrificing strength or ductility [71].

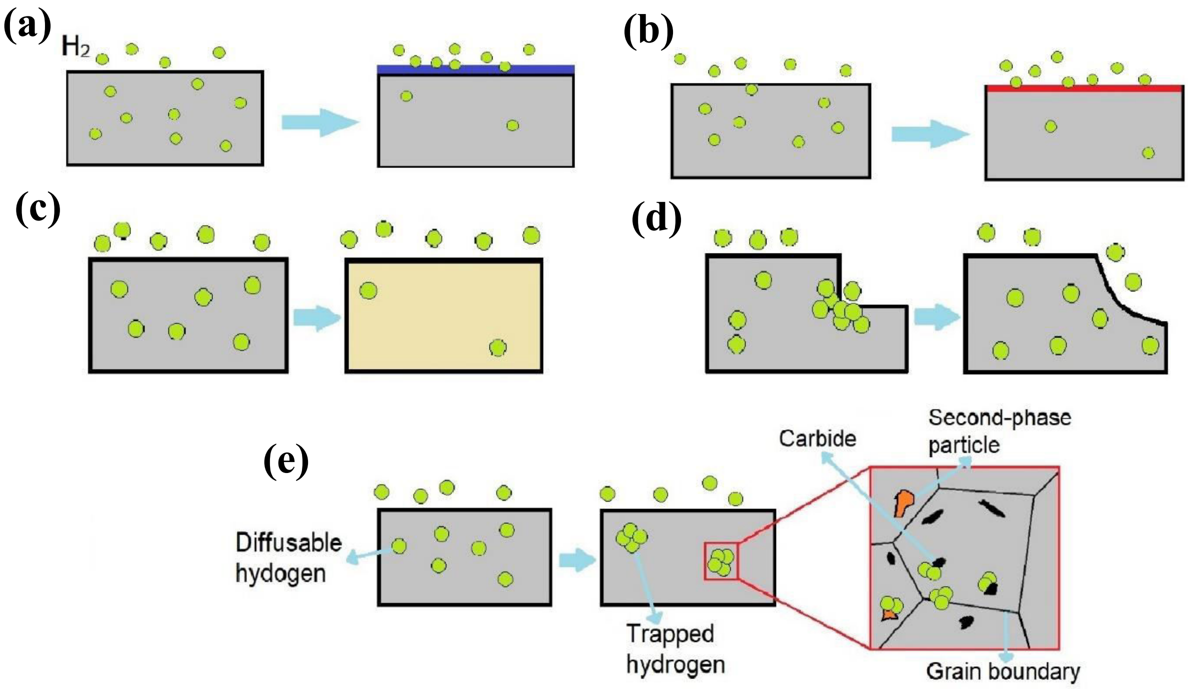

Figure 18. Schematic representation of the HE prevention: (**a**) surface coating, (**b**) surface modification, (**c**) material selection, (**d**) geometrical design and (**e**) microstructure modification.

8. Experimental procedure

8.1 Specimens preparation

The materials used are aluminium and cast iron from various components of a hydrogen-fuelled internal combustion engine, provided by "General Motors" Dumarey. Specifically, the engine head (abbreviated as "EH") and the piston blank ("PB") are made from an Al-Si alloy. The exhaust manifold ("EM") is made of ductile, or spheroidal, cast iron and the engine block ("EB") is made of grey cast iron. The specimens were obtained by machining the various components of the engine, carried out by the operators of the Turin Polytechnic's mechanical workshop, who performed milling operations.

Table 1. Components used for this work

Component	**Abbreviation**	**Material**
Engine head	EH	Al cast alloy
Piston blank	PB	GMW 5 AlSi10Cu4Ni2Mg1-T5 (Al cast alloy)
Exhaust manifold	EM	Si-Mo ductile cast iron
Engine block	EB	GMW4-IR-C-G250 (pearlitic grey cast iron)

Before the hydrogen charging, the specimens were ground using 320, 600 and 1200 grit silicon carbide paper.

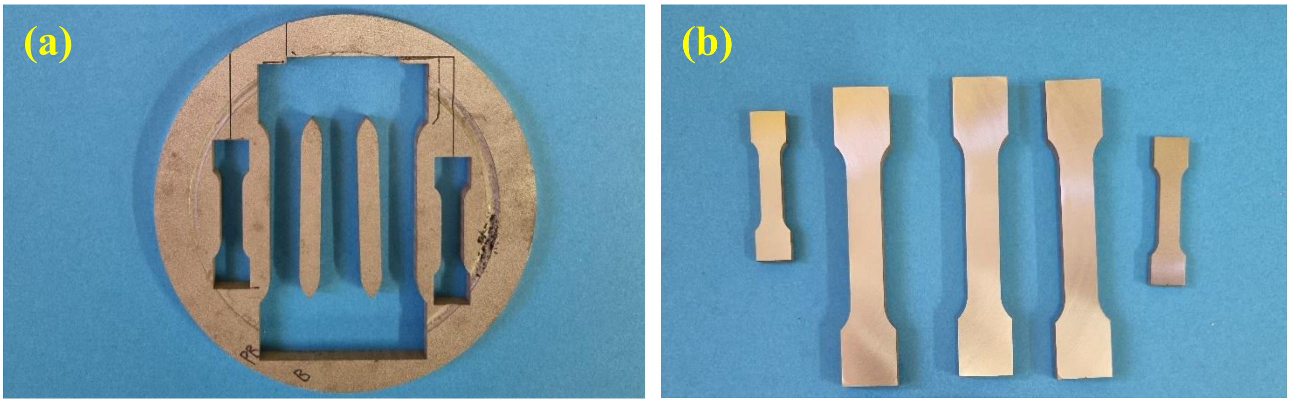

Figure 19. (**a**) Piston blank with specimens removed, (**b**) specimens after the polishing

8.2 Hydrogen charging

The gauge length of the specimens of both cast iron and aluminium were cleaned using an IPA (Isopropyl alcohol) solution just before starting any test to ensure that the surface would not be contaminated from the machining process which could affect the hydrogen uptake. To be charged, each tensile specimen was immersed in a 0.5M aqueous solution of H_2SO_4 at room temperature prior to tensile test, with a cathodic charging current density of -50 and -10 mA/cm^2 for the aluminum and for cast iron, respectively, allowing the hydrogen to diffuse into the specimens, as shown in Fig. 20(a). The hydrogen charging times were 24 h for both the materials. A platinum net was used as an anode and the specimens, either aluminium or cast iron, were used as a cathode. The reduction reaction of hydrogen ions in the solution,

$$2H^+ + 2e \rightarrow H_2 \tag{9}$$

happened over the surface of the specimen. A proportion of the hydrogen escaped into the atmosphere, and part of it diffused into the specimen in atomic form.

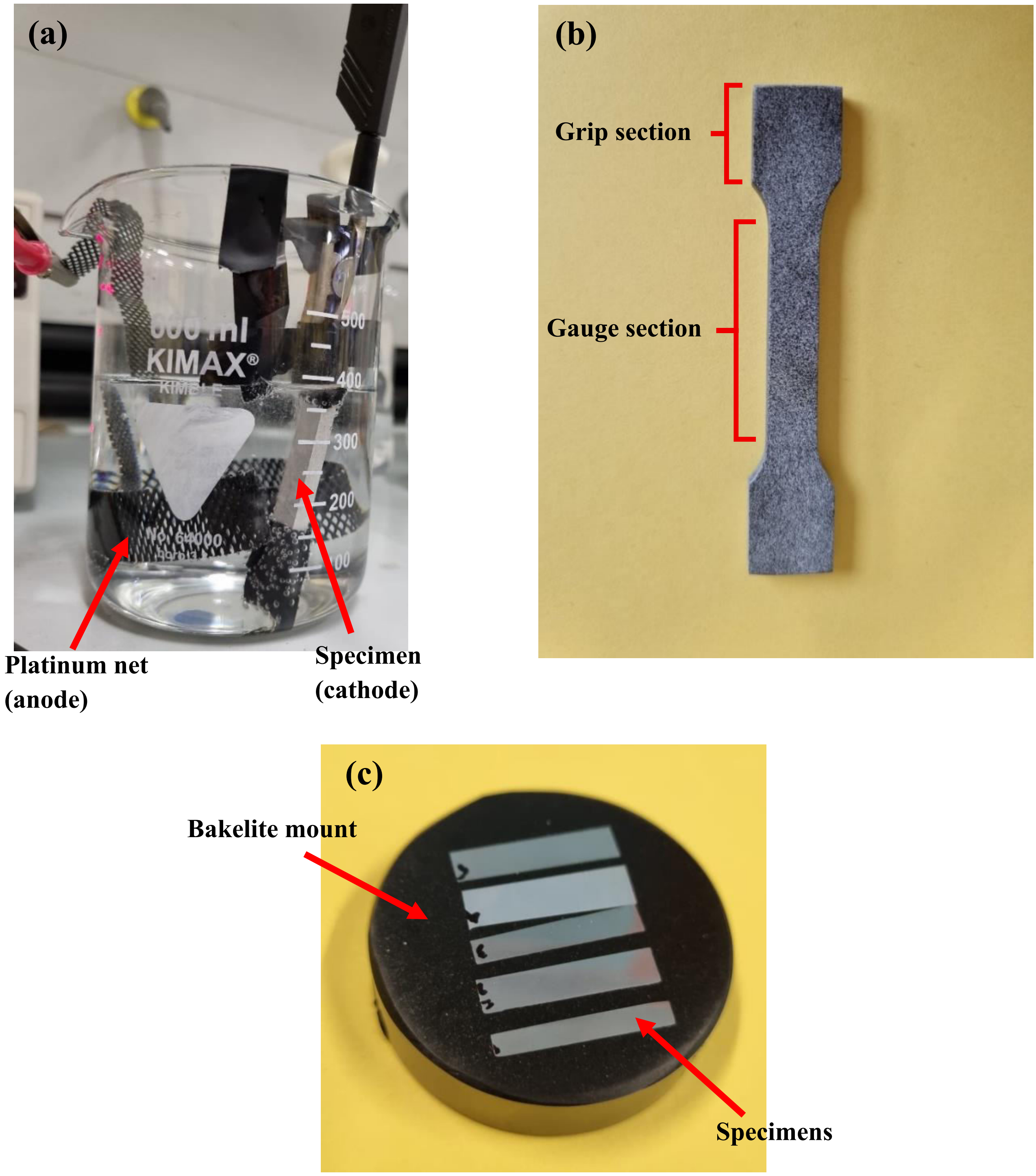

Figure 20. (**a**) Hydrogen charging setup and (**b**) specimen coated with black and white shade before the SSRT. (**c**) Specimens mounted before the microstructural analysis.

Before the tensile test, the specimen is first painted with a uniform coat of white paint and, after it dries, a stochastic pattern of black paint droplets. This is done to ensure digital correlation. The specimen with the paint coating is shown in Fig. 20(b).

8.3 Slow strain rate test

For the tensile characterization of the materials, slow strain rate tests (SSRT) were carried out with an MTS oleodynamic-type tensile and compression machine, with a maximum load of 250 kN. Since the specimens for hydrogen charging was subsize it was adopted Digital image correlation technique to measure the strain with higher accuracy. DIC correlates two images which capture the surface before and after the deformation. In the present study, a white light source is attached with the camera to ensure proper lighting within the system. The maximum value of the correlation coefficient is obtained when the gray-level distribution inside a subset coincides with those inside a local area in the image after deformation. An example of the measurements done by DIC is shown in Fig. 22.

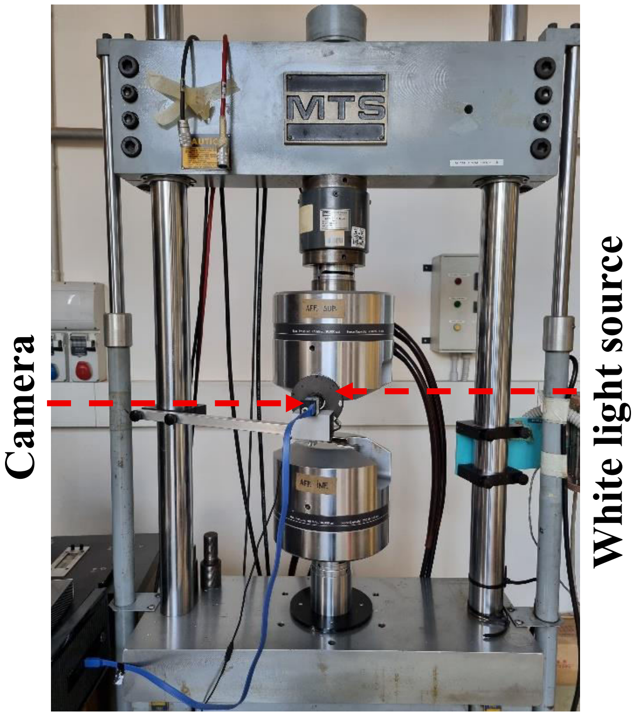

Figure 21. Tensile and compression machine

For this work a strain rate of $5x10^{-5}$ s^{-1} was chosen, as recommended by the standards. The samples were strained to failure while measuring the force with a load cell. The data were exported and stress-strain curves were plotted to calculate the yield stress, ultimate tensile strength and elongation at failure. Ultimate tensile strength is that property of a material which determines how much load it can be withstand until failure. Yield strength is a measure of a material's resistance to plastic deformation, that is a permanent deformation that leaves the material deformed even when the load has been removed. For both the materials used, a yield wasn't well defined, so it was calculated drawing a line with the same slope of the stress-strain curve in the elastic region, with an offset in the strain axis of 0.002.

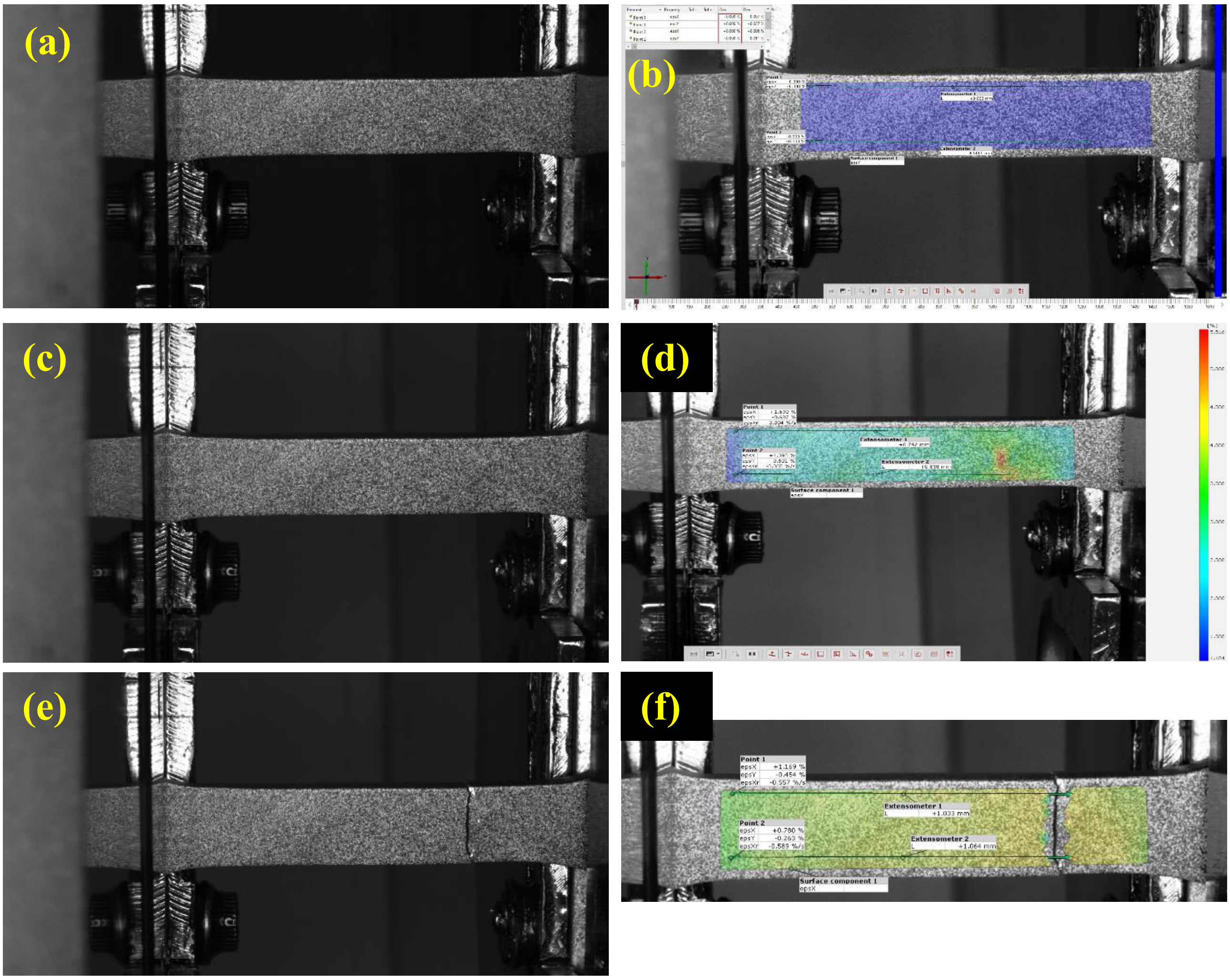

Figure 22. Uncharged "Engine Block" specimen. (**a**) Image and (**b**) Digital image correlation (DIC) of the unstrained specimen. (**c**) Image and (**d**) DIC just before the fracture. (**e**) Image and (**f**) DIC after the fracture.

The tensile tests for both of uncharged (abbreviated as "WHC", i.e. "without hydrogen charging") and hydrogen charged ("HC") specimens were conducted in air at room temperature. After the tensile tests, the fracture surfaces of the specimens were subjected to a detailed analysis via scanning electron microscopy (SEM).

8.4 Microstructure

After the slow strain rate tests, specimens' sections of length approximately 1-1.5 mm was cut off from the grip section using a handsaw. The sections were mounted in bakelite using a LECO PR-36 automatic hot press. Subsequently, mounted specimens were ground using 1200 grit silicon carbide paper and polished with 9, 1 and 0.25 μm diamond suspensions. The mounted specimens are shown in Fig. 21(c). To reveal the microstructural characteristics of the alloys, Keller's reagent (a solution of nitric acid, hydrochloric acid and hydrofluoric acid in distilled water) was used to etch the aluminium alloys and a 2% Nital (ethanol and nitric acid) reagent was used for the cast iron specimens. Final micrographs and corresponding energy dispersive spectroscopy (EDS) were taken using a Zeiss Merlin Field Emission Scanning Electron Microscope equipped with an Oxford X-act energy dispersive X-ray detector.

9. Results and discussion

The results of the slow strain rate tests conducted are shown in Fig. 23 and Fig. 31 and the mechanical property values in Tab. 2 and Tab. 3. The parameters which are used to describe the stress-strain curves are the ultimate tensile strength, yield strength or yield point, elongation at failure and the loss of ultimate tensile strength and ductility. The latter two parameters are defined as:

$$L_\sigma = \frac{\sigma_{UTS} - \sigma_{UTS-H}}{\sigma_{UTS}} \; x \; 100 \; [\%] \tag{10}$$

$$L_\varepsilon = \frac{\varepsilon_{af} - \varepsilon_{af-H}}{\varepsilon_{af}} \; x \; 100 \; [\%] \tag{11}$$

where L_σ and L_ε are the loss of ultimate tensile strength and ductility, respectively, σ_{UTS} it's the ultimate tensile strength of the uncharged specimen, σ_{UTS-H} it's the ultimate tensile strength of the charged specimen, ε_{af} it's the strain, or elongation, at failure of the uncharged specimen and ε_{af-H} it's the elongation at failure of the uncharged specimen.

9.1 Aluminium (Engine head, piston blank)

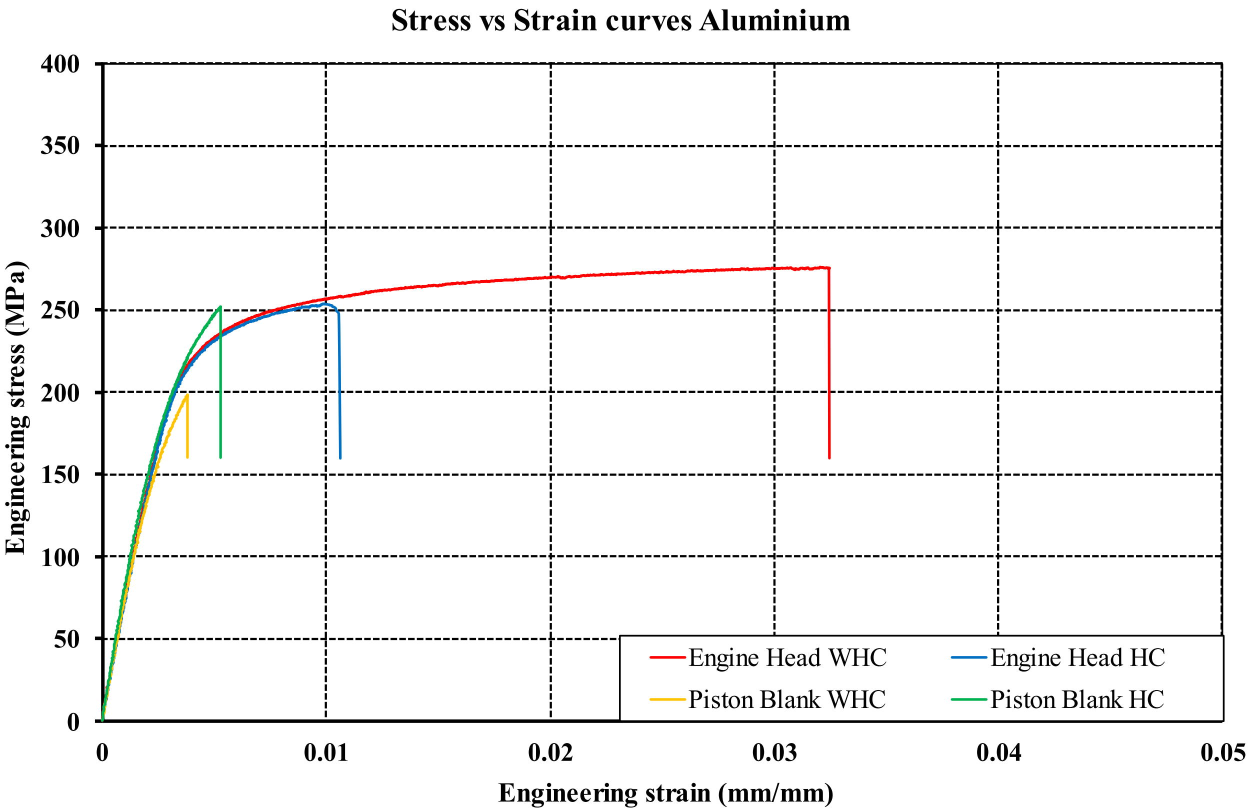

Figure 23. Stress-strain curves of the aluminium specimens

Table 2. Mechanical properties of the aluminium specimens

Specimen	**σ_y [MPa]**	**$\sigma_{y\text{-}H}$ [MPa]**	**σ_{UTS} [MPa]**	**$\sigma_{UTS\text{-}H}$ [MPa]**	**ε_{af} [%]**	**$\varepsilon_{af\text{-}H}$ [%]**	**L_σ [%]**	**L_ε [%]**
Piston Blank	198	250	198	251	0.38	0.53	-27.19	-38.60
Engine Head	236	234	276	256	3.24	1.06	7.95	67.31

9.1.1 Engine Head

The "Engine Head" SSRT curves show an elastic region followed by very limited plasticity. The WHC sample reaches 236 MPa UTS with a 3.24% strain at failure and a yield strength of 236 MPa, whereas the HC sample, with a similar yield strength of 234 MPa, fractures at 1.06% strain with UTS of 256 MPa. Hydrogen charging dramatically reduces ductility (fracture strain is reduced by ~67%) with only a modest reduction of strength. The curves describing the behaviour of the "Engine Head" specimens are consistent with the SEM images of the fracture surfaces shown in Fig. 26.

Al-Si alloys typically contain alloying elements such as copper, magnesium, manganese, zinc, and iron, whose solubility generally increases with temperature. As the alloy cools and solidify or undergoes heat treatments, their solubility decreases leading to the formation of secondary intermetallic phases [72].

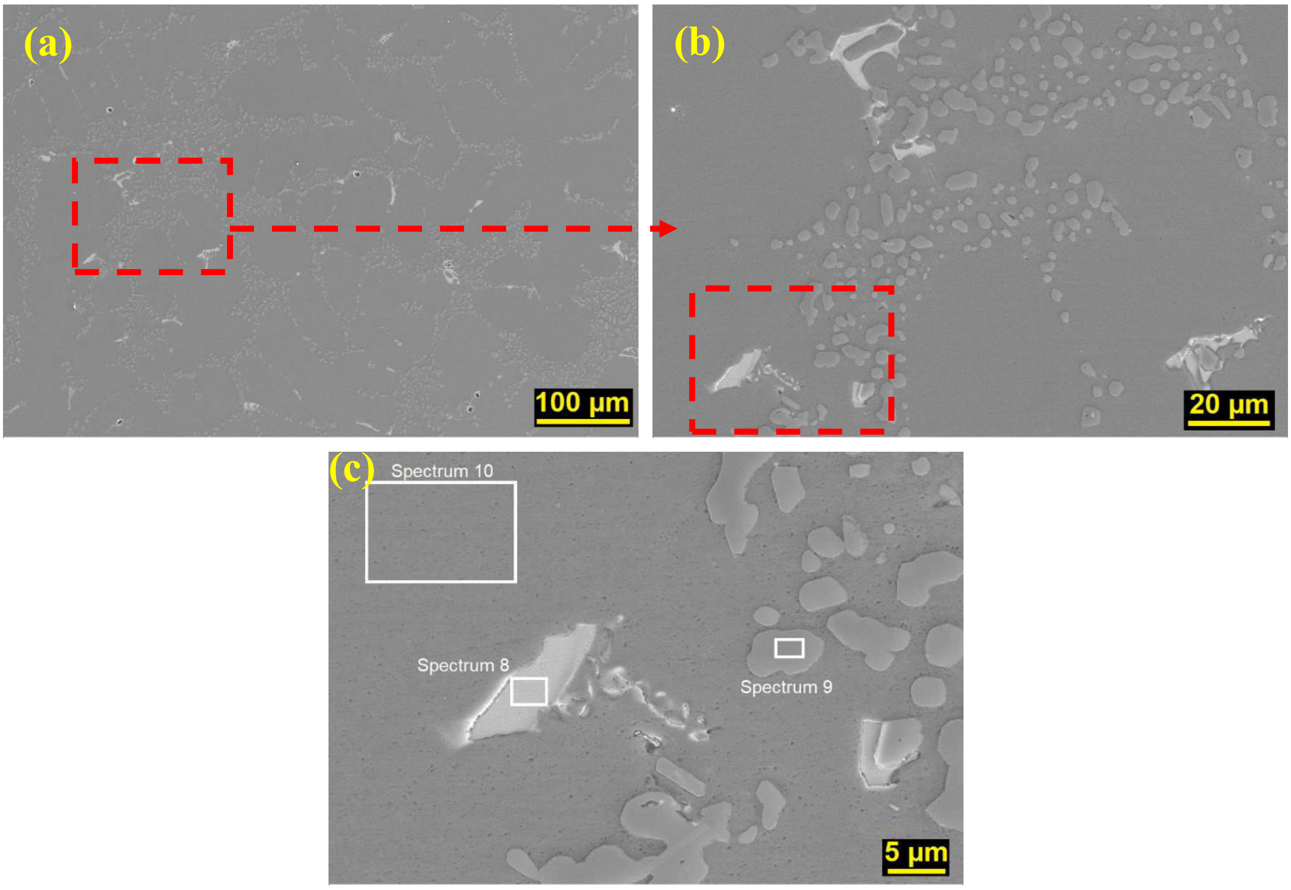

Figure 24. (**a**) SEM micrographs of the microstructure of the "Engine Head" specimen, (**b**) 2000x magnification and (**c**) 5760x magnification indicating the sites for the EDS analysis.

Fig. 24 presents the microstructure of the as-cast Al–Si alloy, consisting in a ductile α-Al matrix interspersed with silicon and various intermetallic phases. In cylinder head aluminium alloys (e.g. near-eutectic Al–Si–Cu–Mg systems), solidification yields primary α-Al dendrites surrounded by a eutectic mixture of Si and intermetallic particles [73]. Fig. 24(a) shows a α-Al phase that have solidified in a dendritic or cellular manner, forming a lighter grey matrix. The interdendritic regions are filled with darker grey eutectic structures and bright, distinct intermetallic particles. The distribution of these secondary phases appears relatively uniform at this scale, though some clustering of intermetallic compounds (IMCs) can be observed. Fig. 24(c), provides the highest resolution view, allowing for detailed observation of the phases targeted for EDS. The light grey α-Al matrix is clearly the dominant continuous phase. The eutectic silicon particles appear as a darker grey phase, with a morphology that seems finer than unmodified eutectic Si, suggesting modification. The bright, angular, and irregularly shaped intermetallic particles are distinctly visible. "Spectrum 8" is targeted at a large, complex-shaped IMC. "Spectrum 9" is focused on the darker grey eutectic phase. "Spectrum 10" is positioned on the α-Al matrix.

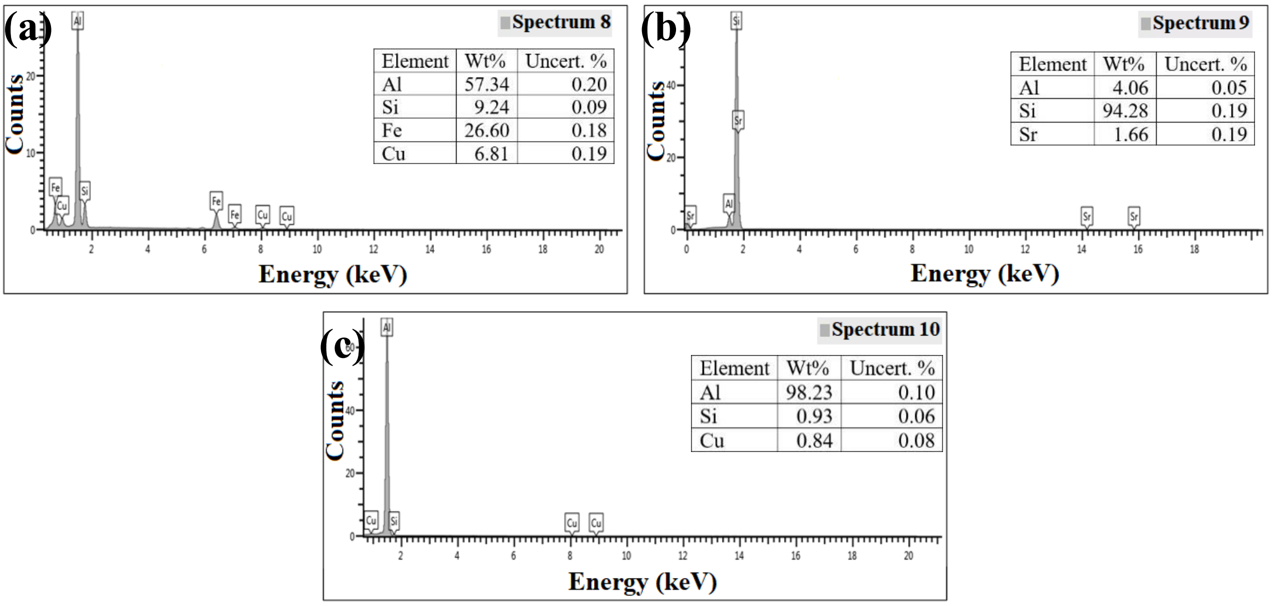

Element	Wt%	Uncert. %
Al	57.34	0.20
Si	9.24	0.09
Fe	26.60	0.18
Cu	6.81	0.19

Element	Wt%	Uncert. %
Al	4.06	0.05
Si	94.28	0.19
Sr	1.66	0.19

Element	Wt%	Uncert. %
Al	98.23	0.10
Si	0.93	0.06
Cu	0.84	0.08

Figure 25. EDS spectra and elemental composition of the different sites shown in Fig. 24(**c**).

Spectrum 8, Fig. 25(a), shows ~57 wt% Al, 27 wt% Fe, 7 wt% Cu and 9 wt% Si, implying an Fe–Cu–Si intermetallic phase. This could be a mixture of Al–Fe–Si and Al–Cu–Fe compounds, or even quaternary Al-Fe-Si-Cu intermetallic or a very fine mixture of intermetallic phase. Common Fe-rich phases include β-Al_5FeSi (or $Al_9Fe_2Si_2$), which is typically needle-like or plate-like, and various α-AlFeSi phases which tend to have more compact morphologies. The blocky morphology observed in the SEM images is more consistent with an α-type AlFeSi phase than the typically acicular β-phase. The phase Al_7Cu_2Fe is a known ternary intermetallic, rich in copper and iron. The EDS analysis shows high Fe (26.60 wt%) and a considerable amount of Cu (6.81 wt%). Spectrum 9, Fig. 25(b), is ~94 wt% Si (with ~4 wt% Al and 1.7 wt% Sr), corresponding to a nearly pure silicon particle, either primary Si (formed before the eutectic) or coarse eutectic Si. The presence of Sr at this site suggests that silicon crystallized with Sr-modified morphology. Strontium is a well-known modifier for Al-Si alloys; its addition transforms the morphology of eutectic Si from coarse, acicular flakes (which are detrimental to mechanical properties) to a fine, fibrous or lamellar structure [74], [75]. Spectrum 10, Fig. 25(c), is ~98 wt% Al with ~1 wt% Si and Cu, indicating the α-Al matrix (aluminium with a small amount of dissolved Si/Cu).

These EDS data match common Al–Si casting phases: the aluminium-solid-solution matrix, silicon particles, and iron and copper-containing IMCs. These phases play distinct roles in engine performance. The α-Al matrix provides the primary load-bearing structure and ductility. The hard Si particles increase strength, wear resistance, and reduce thermal expansion (important in hot combustion environments) but are intrinsically brittle. Fine, fibrous eutectic Si (due to Sr) improves toughness and distributes stress more uniformly. In contrast, Fe-rich IMCs (β-Al_5FeSi, α-Al(Fe)Si, etc.) are hard and thermally stable but severely reduce ductility; needle-like β-Al_5FeSi especially acts as a crack initiation site under stress [73].

Aluminium–silicon (AlSi) alloys typically exhibit ductile fracture behaviour under tensile loading, with fracture surfaces characterized by numerous dimples from microvoid coalescence. Silicon particles (eutectic Si or intermetallics) in the alloy act as internal stress concentrators; voids often nucleate at these brittle Si particles or at particle–matrix interfaces [76]. The presence of hydrogen, however, can dramatically alter mechanical behaviour and fracture morphology. Hydrogen embrittlement in aluminium alloys is known to reduce ductility and shift the fracture mode from a tough, dimpled rupture to a more brittle mechanism [77], [78].

The uncharged AlSi specimen's fracture surface shown in Fig. 26(a) is dominated by ductile dimple rupture features. The surface is uniformly ragged and textured with numerous pits and protrusions, typical of a ductile failure. Zooming in to a higher magnification, Fig. 26(b), it can be seen that most of the fracture areas were covered by equiaxed dimples. These dimples are the imprint of microvoids that nucleated and coalesced during fracture. Each dimple often nucleated around a second-phase particle (such as a silicon particle or intermetallic), which either de-bonded or broke free from the matrix, and it expands towards the final fracture surface. The dimples in the uncharged specimen are relatively large and deep, indicating substantial plastic flow as the voids grew and merged. This is consistent with a high ductility fracture: the material underwent significant local necking between voids before final separation. Notably, some broken particle fragments may be observed inside the dimples (visible as brighter facets or clusters in the SEM image). These are cracked Si particles or other inclusions that acted as void nucleation sites. In Al–Si casting alloys, the morphology of eutectic Si strongly influences this ductile behaviour: coarse, acicular Si leads to easier crack initiation and lower ductility [76], whereas finer, modified Si would improve ductility. Here, the uncharged specimen appears to have undergone ductile tearing around the Si phase, requiring considerable strain to cause fracture.

In contrast, the hydrogen-charged specimen's fracture surface shown in Fig. 26(c) exhibits a mix of brittle and ductile features, reflecting hydrogen's embrittling effect. The fracture surface looks less uniformly fibrous and shows flatter facets or cleavage-like areas with smaller dimples. Also, Large, planar regions can be seen, which are smooth facets compared to the rough dimpled background. These facets suggest sections of the crack that propagated in a brittle manner, possibly along grain boundaries or through the silicon-rich phase, rather than by extensive microvoid growth. The overall appearance is one of a mixed fracture mode: part of the crack advanced suddenly with little plastic deformation (creating flat facets), while other regions still show void coalescence albeit on a smaller scale. At higher magnification, Fig. 26(d), fine details of the hydrogen-charged fracture become clearer. The dimples present here are smaller and shallower than in the uncharged case, indicating that void growth was more limited before failure. The surrounding fracture surface between dimples is noticeably smoother. In some areas, one can observe quasi-cleavage features: these are flat, cleaved-looking patches often bordered by torn edges. Such quasi-cleavage suggests that the crack may have cut through or along brittle constituents (like silicon particles or possibly along crystallographic planes in the aluminium matrix) under the influence of hydrogen. There may also be evidence of intergranular fracture: for instance, if some regions show the outline of grain boundaries or if clusters of second-phase particles have separated together from the matrix, leaving behind cavity-like outlines. This implies the crack in the charged specimen preferentially went along the particle–

matrix interface (debonding it) rather than through the matrix with a dimple, a behaviour consistent with hydrogen weakening the interface.

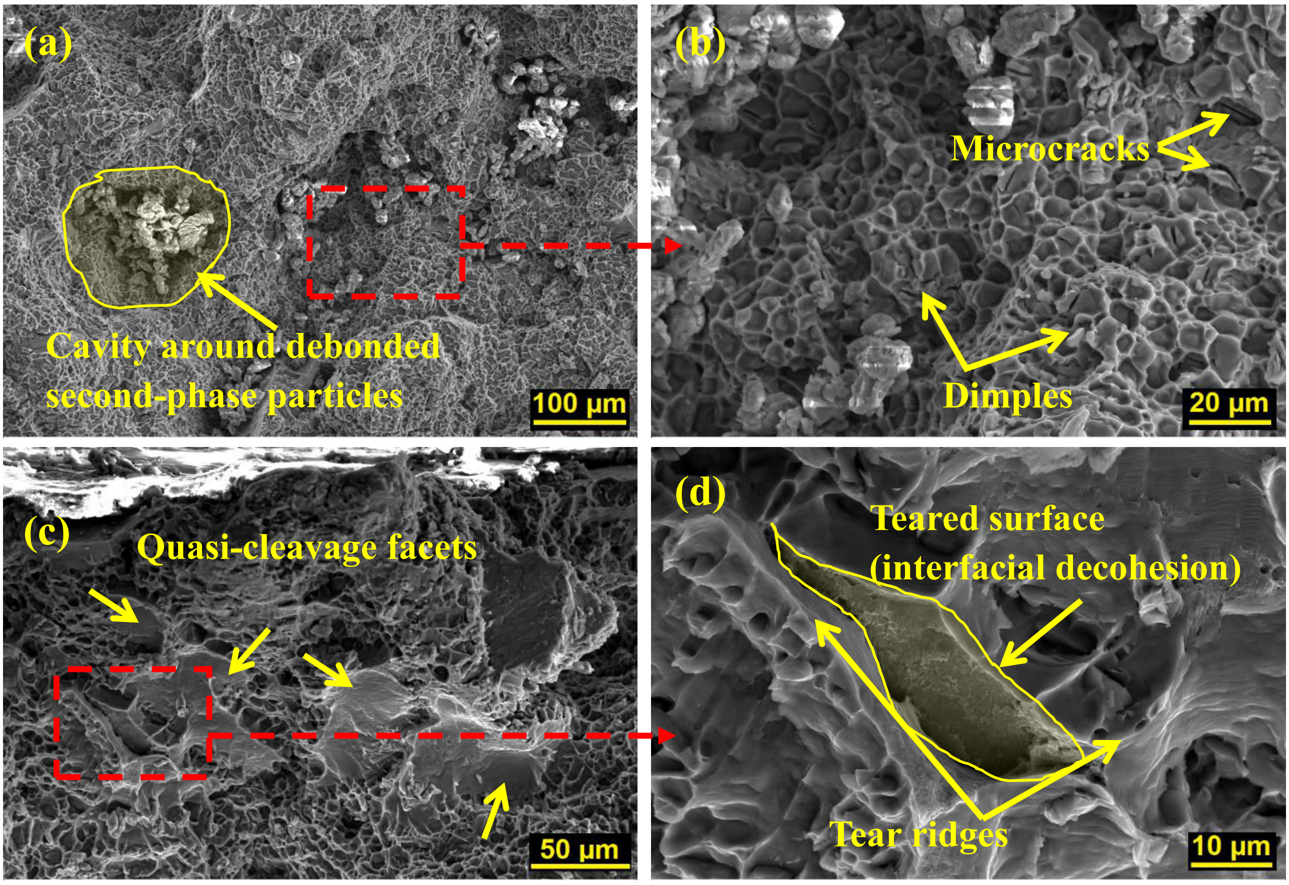

Figure 26. SEM micrographs of the fracture surfaces (**a**, **b**) of the uncharged "Engine Head" specimen at different magnification and (**c**, **d**) of the charged "Engine Head" specimen at different magnification.

The hydrogen-charged fracture surface also contains more secondary cracks or fissures spreading from the main fracture, as hydrogen facilitates crack initiation. Some irregular tears and cracks are visible in the SEM images, especially at high magnification as shown in Fig. 26(d). These fine cracks revealed that the material is affected by hydrogen and was less able to plastically blunt or arrest growing cracks, resulting in multiple crack fronts. In contrast, the uncharged surface is more uniform, with cracks tending to localize only in the final dimpling process.

Both specimens failed via a microvoid mechanism to some extent: hydrogen did not eliminate ductile processes but rather introduced brittle features alongside. The coexistence of small dimples with brittle facets in the charged sample indicates a combined mode of fracture. Such combinations are commonly observed in hydrogen embrittled aluminium: some regions undergo localized plastic void growth (HELP mechanism), while others fail by interface separation (HEDE mechanism), as discussed next. In the charged Al-Si specimen, the small dimples and micro-voids observed may result from HELP: hydrogen allowed dislocations to move easily around hard Si particles, creating tiny voids or micro-cracks there which quickly coalesced. Aluminium is not prone to forming hydrides at room temperature, so the embrittlement is primarily via HEDE and HELP rather than hydride formation. The fracture surface features suggest a combination: interfacial decohesion (brittle facets) plus localized ductile failure (small dimples).

9.1.2 Piston Blank

The SSRT curves for the “Piston Blank” specimens are nearly linear in the elastic region, with the non-charged (WHC) sample reaching 198 MPa UTS at 0.38% strain and the hydrogen-charged (HC) sample reaching 251 MPa at 0.53% strain. The yield strength (0.2% offset) of the specimens corresponds to the ultimate tensile stress (to be precise in the case of the HC specimen is 250 MPa) for both. In the case of the uncharged specimen, the curve does not even reach the 0.2% offset line. This very low elongation is much smaller than typical ductile aluminium alloys, indicating severely limited plasticity. This is justified by the fact that the alloy is intrinsically brittle due to its microstructure, which consist of coarse and hard second phases. The parameters shown before, loss of ultimate tensile strength and ductility, provide negative values indicating that the material properties do not appear to have been affected by the presence of hydrogen, being these higher in the specimen subjected to the hydrogen charging. This is an atypical observation, as hydrogen exposure in many aluminium alloys, particularly cast Al-Si alloys, typically leads to a reduction in ductility. This may be justified by the fact that the hydrogen did not have sufficient time to enter and diffuse into the specimen. Another possible explanation is that hydrogen at very low concentrations can temporarily increase dislocation mobility [37] (HELP effect) and raise apparent strength. In any case, the key feature is the brittle-like fracture: both curves end abruptly at very low strain as shown in Fig. 23. In other words, the overall shape (minimal elongation, little uniform plasticity) matches the fracture evidence of a cleavage-like failure mode. However, the higher flow stress of the charged sample is unusual and suggests experimental scatter or localized effects. In general, literature on Al alloys indicates hydrogen charging reduces overall plasticity and often lowers strength slightly [77]. Therefore, one should interpret the green curve with caution. Overall, though, the qualitative mechanical behaviour (high strength-to-ductility ratio and abrupt failure) is consistent with the SEM images of the fracture surfaces as shown in Fig. 30.

The SEM images at increasing magnification in Fig. 27 shows the characteristic microstructure of hypoeutectic Al-Si alloys with added alloying elements. During solidification primary dendrites of Al-rich solid solution form first, followed by (α-Al+β-Si) eutectic at lower temperature. Alloying additions (Cu, Ni, Fe) segregate into the last-solidifying liquid, forming intermetallic compounds. These features are highly characteristic of cast Al-Si alloys specifically designed for piston applications [79]. Fig. 27(a), at 1000× magnification, shows large globular dendritic cells (~tens of µm) that are outlined by a spider-web network of Si-rich eutectic and intermetallic (Cu and Ni) lamellae. These lamellae appear as light-grey rods and platelets connecting the dendrite cores. Fig. 27(b) at a magnification of 5000×, allows for a more detailed examination of the interdendritic constituents. The eutectic Si morphology is clearly resolved as relatively coarse and acicular or plate-like. The intermetallic phases exhibit a range of morphologies and contrast levels (appearing in various shades of grey and white in the backscattered electron image, indicative of different average atomic numbers). Some IMCs are distinctly elongated or needle-like, while others present more equiaxed, script-like, or complex branched morphologies. In Fig. 27(c), at 20,000×, the Al matrix shows fine cellular substructure, and numerous bright sub-micron particles appear. These are second-phase precipitates. Finally, at 100,000×, Fig. 27(d), these precipitates are clearly nanoscale IMC (e.g., fine Al_2Cu, Al_3Ni or Al-Cu-Ni precipitates) or dispersoids formed during solidification or any subsequent thermal treatments. If present in sufficient density, these fine precipitates would not only contribute to the alloy's strength via precipitation hardening but also introduce a high density of additional hydrogen trapping sites due to their large surface area-to-volume ratio.

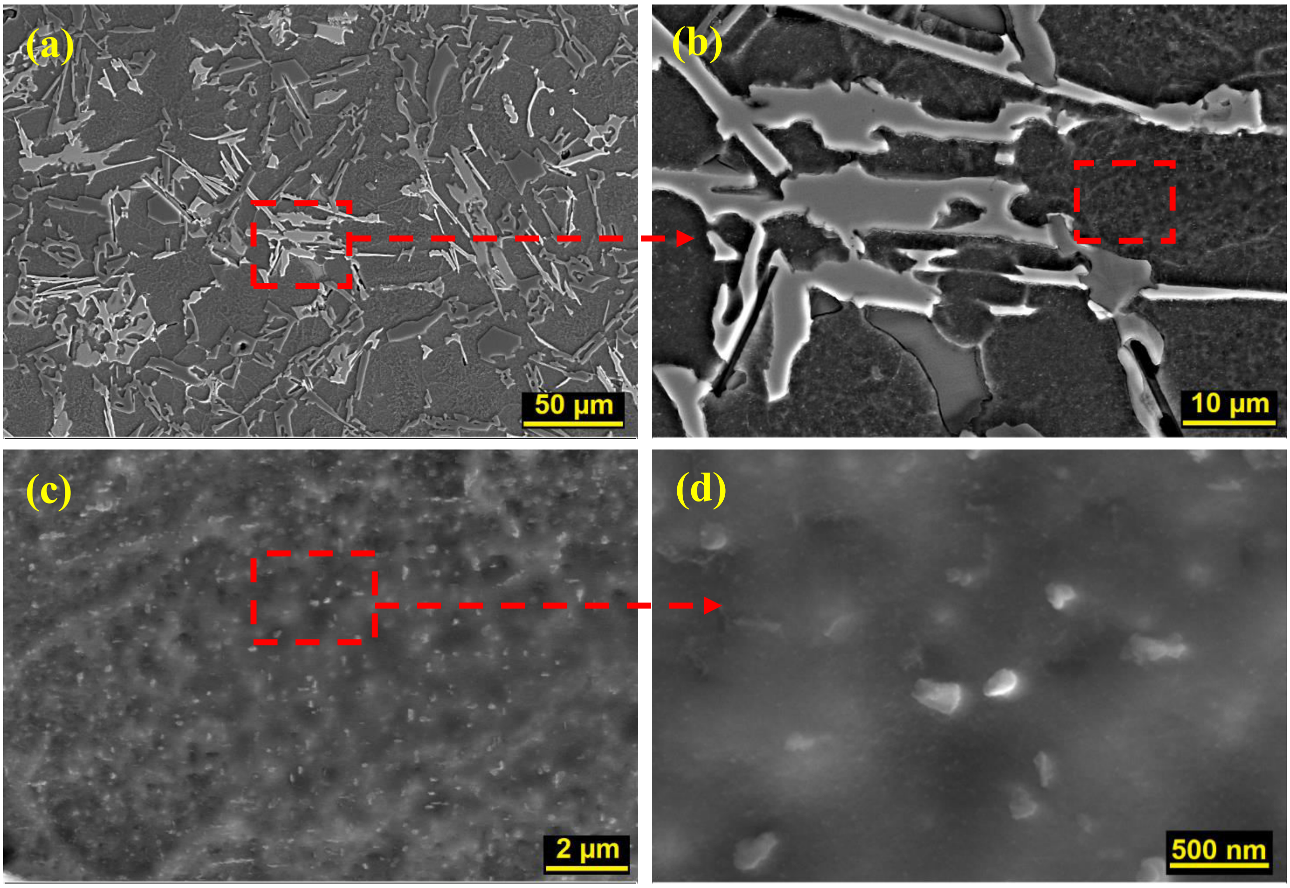

Figure 27. SEM micrographs of the "Piston Blank" specimen at different magnifications. (**a**) 1000x, (**b**) 5000x, (**c**) 20000x, (**d**) 100000x.

Fig. 28 shows the EDS elemental maps of the dendritic field and confirms the phase distribution. The Al map, Fig. 28(b), is bright in the large dendrite cores, confirms that aluminium is the dominant element, forming the continuous matrix phase, consistent with an α-Al solid solution. The Si map shown in Fig. 28(c) highlights the light lamellae between dendrites (high Si concentration in the eutectic). Nickel, Fig. 28(d), is shown to be concentrated in specific interdendritic particles. The spatial distribution of Ni exhibits a strong visual correlation with that of copper (Fig. 28(e)). This co-localization is a strong indicator of the presence of Al-Ni-Cu ternary intermetallic compounds or at least the co-precipitation of distinct Al-Ni and Al-Cu phases in very close proximity. Iron, Fig. 28(f), is present in generally smaller quantities compared to Cu and Ni and, based on the composition of the alloy, it could be considered as an impurity, that's very common in aluminium alloys. It forms discrete, relatively fine intermetallic particles that are also located within the interdendritic regions. Some of these Fe-rich particles appear in the same regions of the main Ni-rich and Cu-rich phases, suggesting the presence of Al-Ni-Fe or Al-Cu-Fe intermetallic compounds while others appear distinct from them. Given the Al-Si matrix and the presence of Fe, these are most likely Al-Fe-Si compounds. As extensively documented, acicular or platelet-like phases, such as β-Al_5FeSi, act as significant stress concentrators and can severely compromise the alloy's ductility and fracture toughness by providing easy paths for crack initiation and propagation [80].

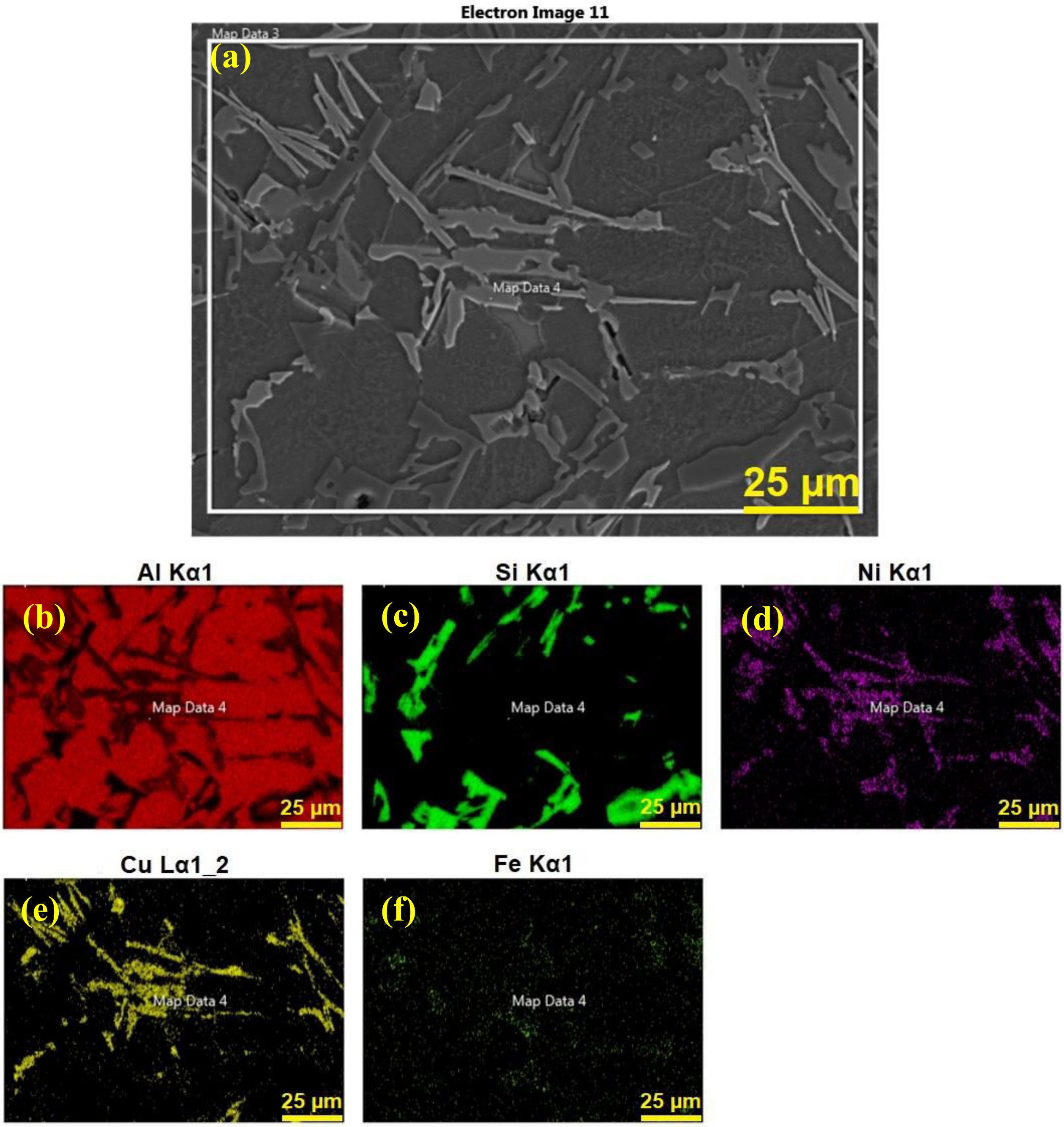

Figure 28. (**a**) SEM micrograph and (**b-f**) EDS elemental distribution maps of the "Piston Blank" microstructure.

Fig. 29(a) shows the EDS line scan across a dendrite/interdendritic region (~30 µm span) that confirms this segregation. The Al signal, Fig. 29(c) is high in the matrix, with sharp drops precisely where Ni, Fig. 29(e) and Cu, Fig. 29(f), show strong peaks. For example, simultaneous Ni+Cu peaks around 5 and 25 µm coincide with near-zero Al, indicating Ni-rich rod-like IMCs (e.g. ε-Al_3Ni or γ-Al_7Cu_4Ni) [81]. Other peaks (10–20 µm) with pronounced Cu but low Ni suggest Cu-rich compounds (θ-Al_2Cu or δ-Al_3CuNi [81], [82]). In contrast, the Si signal in Fig. 29(d) is relatively flat along this line, with some peaks at the phase boundaries between IMCs and the Al matrix, implying that the scan crossed Al and intermetallic rich areas rather than large pure Si plates. Overall, these profiles show Al-dendrite cores alternating with low-Al, Cu/Ni-bearing precipitates, consistent with the SEM morphology of interdendritic intermetallic networks.

A second line scan, Fig. 29(b), at much higher magnification (~0.6 µm span) over submicron precipitates reveals complementary behaviour. The Al signal in Fig. 29(g) dips sharply at locations where the Cu Fig. 29(h) and Si Fig. 29(i) signals spike. This indicates very fine particles rich in Cu and Si within the Al matrix. Such a signature is characteristic of Cu–Al–Si intermetallics (for instance, the θ-Al_2Cu phase or related Si-bearing Cu–Al compounds) known to form in Al–Si alloys [73], [83]. Indeed, the Cu peaks (~180 cps) and Si peaks (~150 cps) in the scan are much higher than the background, confirming these precipitates' Cu/Si enrichment and reduced Al content. These submicron particles likely crystallized late from the Cu/Si-enriched residual melt (possibly a Q-phase or θ-phase), embedding brittle intermetallic precipitates in the dendritic channels.

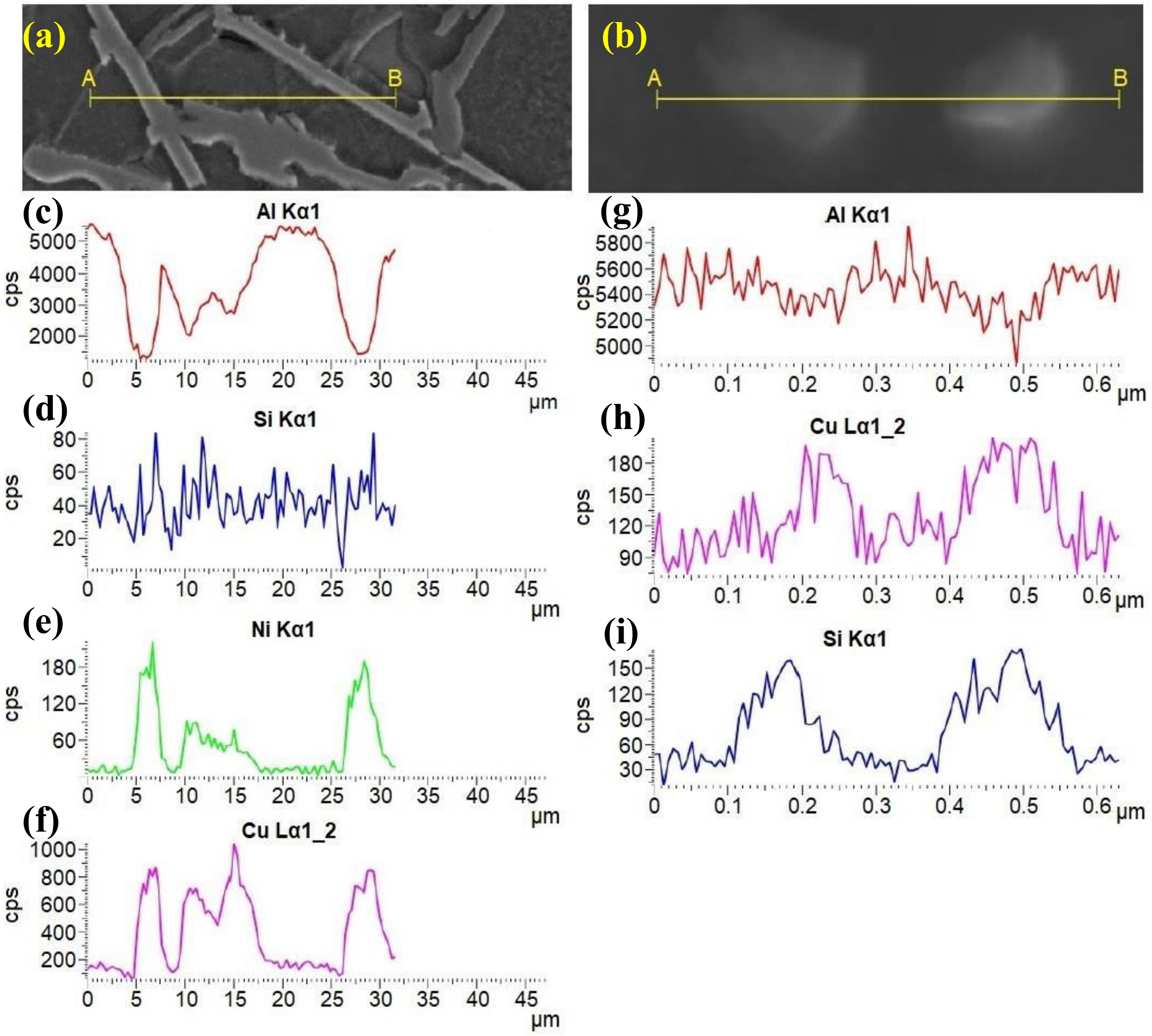

Figure 29. SEM micrographs and linear EDS elemental distribution of (**a**, **c**-**f**) interdendritic structures and (**b**, **g**-**i**) nano particles of the "Piston Blank" specimen.

Fig. 30 shows the SEM micrographs of the fracture surfaces of the AlSi10Cu4Ni2Mg1-T5 "Piston Blank" alloy following Slow Strain Rate Testing (SSRT) in both the uncharged and hydrogen-charged conditions.

The fracture surface of the uncharged specimen, Fig. 30(a), is indicative of a predominantly brittle failure mode, which is consistent with the very low macroscopic ductility (~0.4% elongation) observed in the SSRT data (Fig. 23). The overall topography of the fracture surface mirrors the as-cast dendritic microstructure. The crack distinctly followed the interdendritic zones, which are filled with a network of large and brittle secondary phases. The surface is dominated by sharp, flat facets of varying sizes. These facets correspond to the brittle fracture of the coarse microstructural constituents. Given the alloy's composition, these fractured particles are the eutectic silicon (Si) and the complex, hard intermetallic compounds (IMCs) such as the Ni- and Cu-rich phases that form the interdendritic network. The fracture of these hard phases requires minimal plastic deformation, explaining the low overall ductility. There is a conspicuous lack of ductile dimples, which are the hallmark of failure by microvoid coalescence. This confirms that the ductile α-Aluminum matrix did not undergo significant plastic deformation prior to failure. Instead, the strain incompatibility between the soft matrix and the rigid, brittle second-phase network leads to crack initiation at these particles at very low applied strains. In essence, the uncharged alloy fails via a low-energy fracture path that exploits the inherent brittleness of its as-cast interdendritic network. The failure is controlled by the fracture strength of the Si and IMC particles and the cohesive strength of their interfaces with the matrix.

At first glance, the fracture surface of the hydrogen-charged specimen, Fig. 30(b), appears remarkably like its uncharged counterpart, exhibiting a fundamentally brittle character. The fracture path still follows the interdendritic network, the features appear more defined and three-dimensional. There is more pronounced evidence of decohesion around the second-phase particles, rather than just cracking through them. The surfaces of the exposed facets appear somewhat cleaner and more representative of the original particle morphology, suggesting that the crack has propagated along the particle-matrix interface. The brittle characteristics are intensified. There are no signs of increased ductility at the microscopic level; on the contrary, the fracture appears to be even more localized to the brittle phase network.

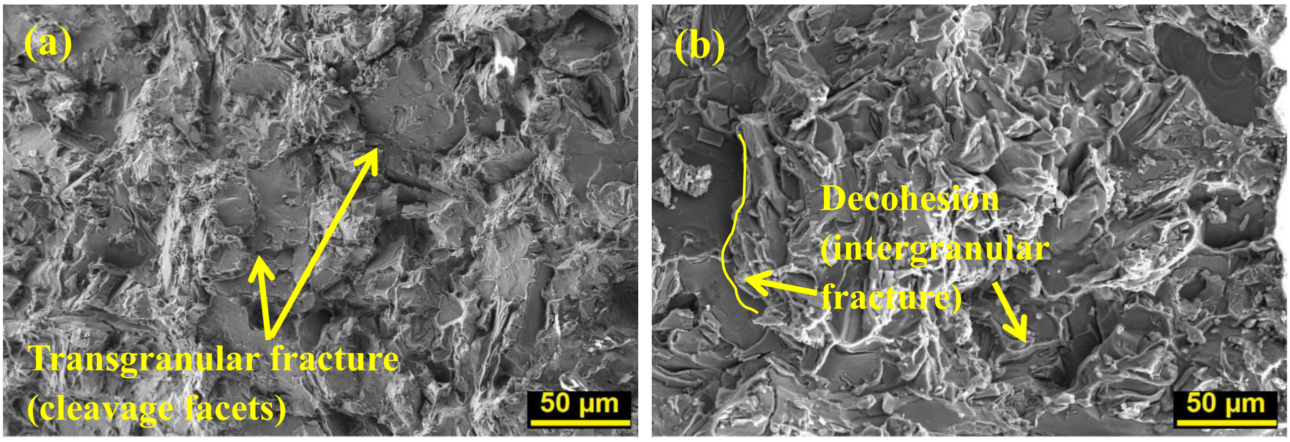

Figure 30. SEM micrographs of the fracture surfaces of the (**a**) uncharged and (**b**) charged "Piston Blank" specimens.

The comparison of the two fracture surfaces provides a clear insight into the effect of hydrogen on this specific alloy. Unlike a classic ductile-to-brittle transition, the AlSi10Cu4Ni2Mg1-T5 alloy is intrinsically brittle. Therefore, hydrogen does not introduce a new failure mode but rather exacerbates the pre-existing brittle mechanisms. The operative mechanism is Hydrogen-Enhanced Decohesion (HEDE). During electrochemical charging, hydrogen atoms diffuse into the alloy and segregate to energetically favorable "trap" sites. The most potent traps in this microstructure are the interfaces between the α-Al matrix and the numerous second phases (eutectic Si and the complex Al-Cu-Ni-Mg IMCs). These incoherent or semi-coherent interfaces represent regions of high lattice strain and disorder, making them ideal locations for hydrogen accumulation. According to the HEDE theory, the high concentration of hydrogen at these interfaces weakens the interatomic bonds between the matrix and the second-phase particles. During tensile loading, these hydrogen-weakened interfaces become the path of least resistance for crack propagation. The critical stress required for interfacial decohesion is significantly lowered. As a result, the crack preferentially initiates and propagates along these interfaces rather than requiring the higher stress needed to fracture the particle itself or deform the surrounding matrix. This explains the subtle morphological differences. The more pronounced relief and evidence of interfacial separation on the charged specimen's fracture surface are direct consequences of the HEDE mechanism providing an "easier" fracture path around the particles.

Typically, hydrogen, upon entering an aluminium alloy, does not remain uniformly dispersed within the solvent lattice. Instead, it tends to segregate to specific microstructural locations known as "traps." First, one must consider lattice defects within the α-Al matrix: these include point defects like vacancies, line defects such as dislocations (both edge and screw types), and planar defects like grain boundaries and phase boundaries. Monovacancies in the Al lattice are known to be relatively strong traps for hydrogen, with studies [84] that report a value of ~ 29 kJ/mol, while grain boundaries, with ~ 24 kJ/mol and dislocations, between 10 and 18 kJ/mol depending on the type of dislocation, offer weaker traps for hydrogen.

Based on the microstructures of both the Al-Si alloys studied, i.e. the “Engine Head” (Fig. 24 and Fig. 25) and the “Piston Blank” (Fig. 27, Fig. 28 and Fig. 29), different features can be identified as hydrogen traps. Studies demonstrated that interfaces between α-Al matrix and eutectic Si particles significant hydrogen trapping, resulting in a binding energy of ~51 kJ/mol [85], making them a strong trap for hydrogen. In the case of the “Engine Head”, the role of strontium modification is particularly relevant here. The morphological change drastically increases the total Al/Si interfacial area per unit volume within the alloy. If the Al/Si interface is indeed a strong hydrogen trap, then the increased interfacial area resulting from Sr modification could substantially enhance the alloy's overall capacity to trap hydrogen at these sites. This presents a complex scenario: while Sr modification is beneficial for mechanical properties by altering Si particle shape, it might inadvertently create a more extensive network of relatively strong hydrogen traps at the Al/Si interfaces. This could lead to higher local hydrogen concentrations at these interfaces, potentially influencing susceptibility to interface-related fracture mechanisms if hydrogen reaches critical levels. No direct studies specifically calculating the hydrogen trapping energy at Sr-modified Al/Si interfaces were found in the available literature.

The various IMCs present in the alloy are prime candidates for hydrogen trapping, both at their interfaces with the Al matrix and potentially within their bulk crystal structures, where internal defects or crystal structures can accommodate hydrogen. Binding energy for Al-Cu IMCs, such as Al_2Cu, has been measured at ~18 kJ/mol [86] which makes them fairly weak traps. Al-Fe-Cu IMCs like Al_7FeCu_2 are known to be strong hydrogen traps. Their values for binding energy have been measured [87] between ~40 and 54 kJ/mol. Other IMCs such as Al-Ni (e.g. Al_3Ni, Al_3Ni_2), Al-Cu-Ni (e.g., Al_3CuNi, Al_7Cu_4Ni), Al-Fe-Si (e.g., β-Al_5FeSi) have been studied for different reasons about their interaction with hydrogen, but data for binding energies aren’t available in literature. Likewise, the nano-particles identified likely Al-Cu or Al-Cu-Si based, and their interfaces with the matrix can trap hydrogen. Al-Cu precipitates (Al_2Cu) binding energy has been reported above.

Considering the stress strain-curves in Fig. 23 of the both these Al-Si alloys specimens, some considerations can be done. The “Engine Head” curves clearly show how hydrogen reduced mechanical properties, causing a decrease in ductility and ultimate tensile strength. One possible explanation may be that the distribution of traps was not evenly distributed, favouring the presence of weak traps which, once saturated after hydrogen charging, caused the diffusible hydrogen to move within the material and contribute to embrittlement. “Piston Blank” curves instead, do not allow a clear relationship between the presence of these traps, which are more or less strong and therefore more or less able to reduce the presence of diffusible hydrogen and mechanical properties. In fact, the curve of the hydrogen charged specimen presents an unexpected increase of these properties, which cannot be attributed to the presence of traps but to the fact that hydrogen did not have the possibility of interacting significantly with the material.

9.2 Cast iron (Exhaust manifold, engine block)

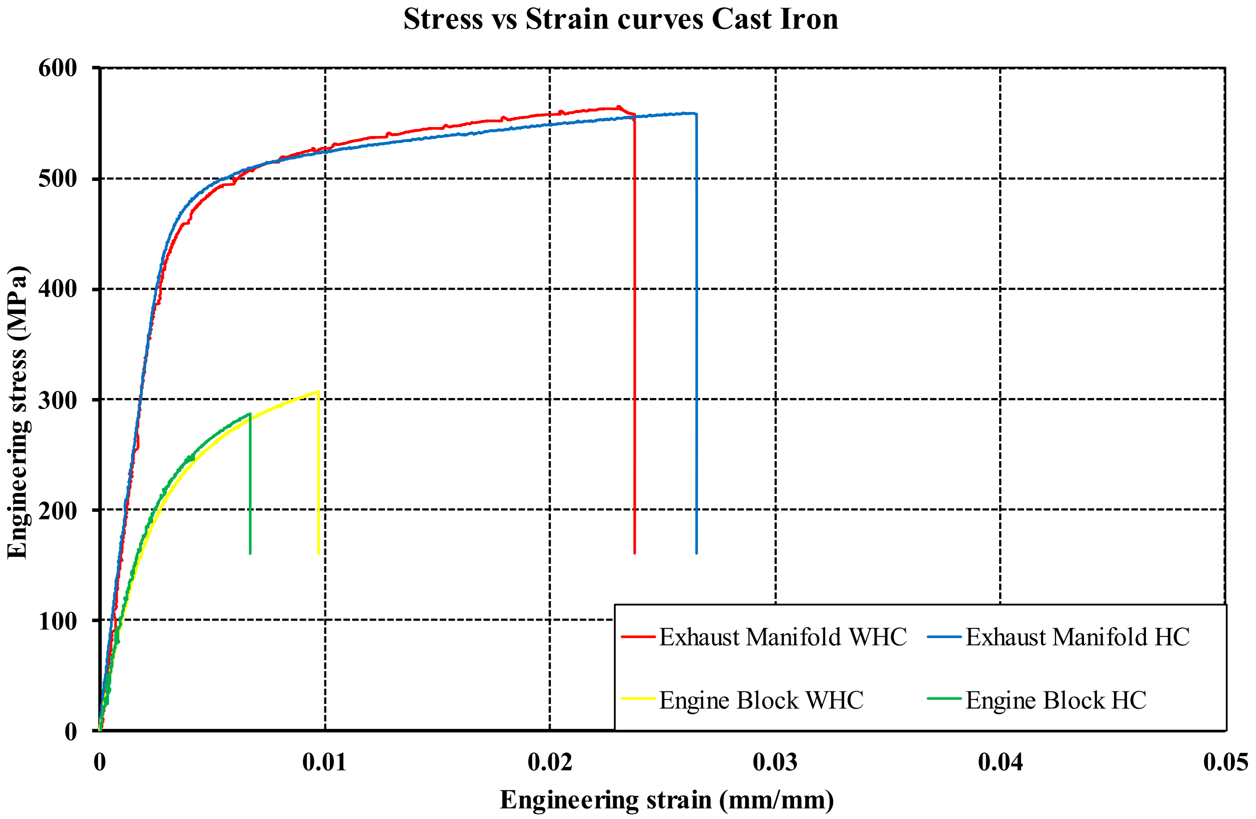

Figure 31. Stress-strain curves of the cast iron specimens

Table 3. Mechanical properties of the cast iron specimens

Specimen	**σ_y [MPa]**	**$\sigma_{y\text{-H}}$ [MPa]**	**σ_{UTS} [MPa]**	**$\sigma_{UTS\text{-H}}$ [MPa]**	**ε_{af} [%]**	**$\varepsilon_{af\text{-H}}$ [%]**	**L_σ [%]**	**L_ε [%]**
Exhaust Manifold	489	495	575	559	2.3	2.65	2.88	-15.36
Engine Block	252	254	307	286	0.97	0.67	6.64	31.44

The yield strength of the uncharged and of the charged specimens is similar. This applies to both the specimens made of ductile cast iron, “Exhaust Manifold”, and the ones made of grey cast iron, “Engine Block”. The ultimate tensile strength of the materials was reduced in the SSRT under hydrogen charging. The elongation to failure was reduced by over the 30% in the grey cast iron specimens, while the elongation to fracture of the ductile cast iron specimens is found to be increased by 15%, showing an increase in ductility contrary to expected results and the scientific literature [88], [89].

9.2.1 Ductile cast iron (Exhaust manifold)

The ductile cast iron “Exhaust Manifold” specimens exhibit much higher strength and ductility than the grey cast iron: the WHC specimen yields at 489 MPa and has a UTS of 575 MPa with ~2.3% strain to fracture; the HC curve is nearly overlapping, indicating minimal loss in this tensile test. Perhaps unexpectedly, the engineering strain at fracture for the HC sample appears to be slightly greater than that of the WHC sample. This observation deviates from the classical manifestation of hydrogen embrittlement in many ferrous alloys, where a significant reduction in ductility (elongation to failure) is typically a primary indicator. The values of elongation at failure are still low compared to what is normally expected from this material [90]. All this also is confirmed by SEM images of the surface fracture, shown in Fig. 35 where, despite the formation of voids where graphite nodules are present, the matrix of the material shows brittle behaviour in both charged and uncharged specimens. To analyse these specimens towards hydrogen embrittlement, charging time has to be increased.

Ductile cast iron (DCI) is characterized by the morphology of its graphite, made up of discrete spheroids or nodules. This spheroidal graphite structure is achieved through a specific melt treatment process involving the addition of spheroidizing elements, such as magnesium or cerium, prior to casting. Graphite nodules behave more like crack arrestors, imparting superior ductility, toughness, and tensile strength to the cast iron. Fig. 32 shows the microstructure of the ductile cast iron used in this work and the corresponding EDS analysis of its surface. In Fig. 32(a) the micrograph reveals the characteristic features of DCI: numerous dark, generally spherical to slightly irregularly shaped graphite nodules are dispersed within a lighter-toned metallic matrix. These nodules appear reasonably well-formed, indicating effective spheroidization treatment, although some exhibit minor deviations from perfect sphericity. Fig. 32(b), at higher magnification, offers a clearer depiction of the graphite nodules embedded in the metallic matrix. At this magnification, the matrix itself appears relatively homogeneous and largely featureless, which could imply a predominantly ferritic constitution. In addition to the primary graphite nodules, some smaller, dark features are discernible; these could represent microporosity, smaller graphite particles, or non-metallic inclusions.

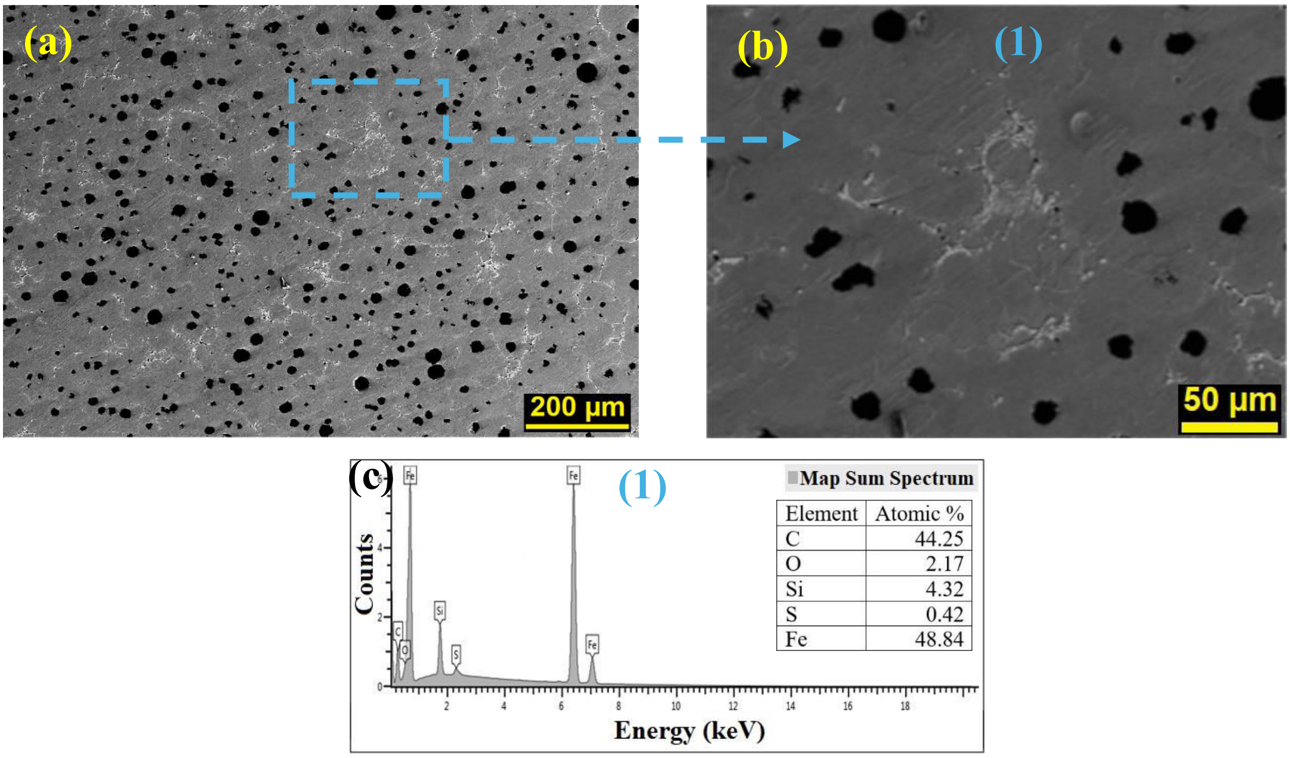

Element	Atomic %
C	44.25
O	2.17
Si	4.32
S	0.42
Fe	48.84

Figure 32. (**a**) SEM micrograph of the microstructure of the "Exhaust Manifold" specimen, (**b**) higher magnification and (**c**) EDS spectrum and analysis composition of the region

Fig. 32(c) shows the EDS spectrum of the region shown in Fig. 31(b) and provides an average elemental composition of the analysed region. The carbon content is consistent with the classification of the material as a cast iron. The significant silicon concentration is a typical feature of high-silicon ductile irons, often referred to as Si-Mo grades, that are specifically designed for high-temperature applications [91]. It is a potent graphitizer element and generally promotes the formation of a ferritic matrix. The detection of oxygen suggests the presence of oxides, such as SiO_2, which could exist as discrete inclusions within the microstructure or as a surface oxidation layer. This silica-rich surface layer confers excellent oxidation resistance at high temperatures [92]. The sulphur content is notable.

Fig. 33(a) shows a region of the microstructure in Fig. 32. It focuses on a specific region within the DCI microstructure, where a cluster of lighter-phase particles exhibiting a complex, somewhat skeletal or script-like morphology, embedded within the surrounding matrix is present. Fig. 32(b) and Fig. 32(c) provides a magnified view of the particles from the aforementioned cluster and the sites where the EDS analysis was taken.

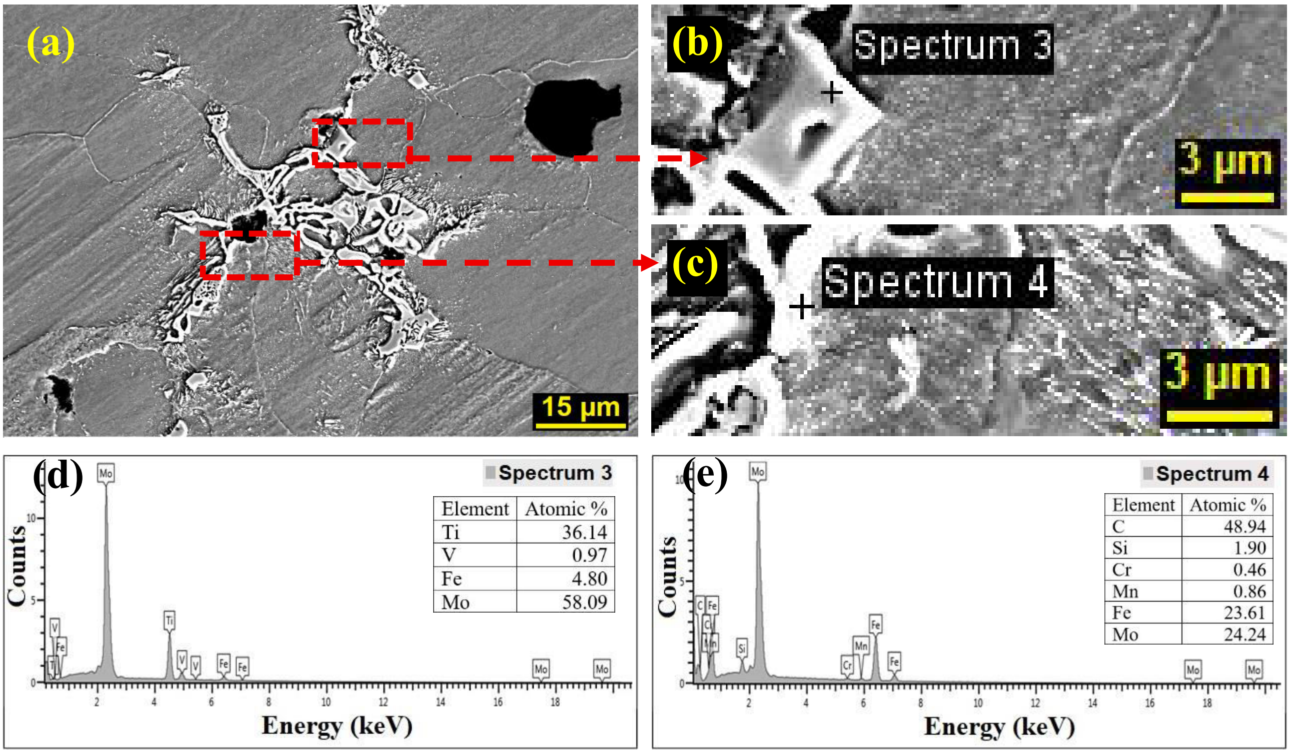

Spectrum 3

Element	Atomic %
Ti	36.14
V	0.97
Fe	4.80
Mo	58.09

Spectrum 4

Element	Atomic %
C	48.94
Si	1.90
Cr	0.46
Mn	0.86
Fe	23.61
Mo	24.24

Figure 33. (**a**) Micrograph of a region in Fig. 31(**a**), (**b**, **c**) higher magnification indicating the sites for the EDS analysis and (**d**, **e**) the corresponding EDS spectra and elemental composition.

Fig. 33(d) shows the EDS spectrum and the element composition of the "Spectrum 3" spot. This site is characterized by very high molybdenum and significant titanium content, which are potent carbide stabilizers, strongly indicates the presence of a complex carbide or intermetallic phase. Molybdenum is a potent alloying element in cast irons, known to increase strength, hardness, and toughness [93]. It is also a powerful pearlite promoter, refining the lamellar spacing of pearlite. Given the overall carbon-rich nature of cast iron, these particles are highly likely to be (Mo,Ti)C mixed carbides. Fig. 33(e) shows the EDS spectrum and the element composition of the "Spectrum 4" spot. The high carbon content might be influenced by proximity to unresolved fine carbides or even a nearby graphite phase. The molybdenum content in this region is significant, suggesting that molybdenum is not exclusively confined to the large, discrete Ti-Mo rich particles observed in Fig. 33(b). Instead, Mo also appears to be present in considerable amounts within the surrounding matrix or forms other distinct Mo-rich phases or finer precipitates. The detection of chromium and manganese in this spectrum is also noted.

Fig. 34(a) presents an SEM micrograph of a region displaying several microstructural features. Dark, irregularly shaped graphite nodules are visible, with one prominent nodule situated in the lower-left portion. The metallic matrix exhibits distinct morphological variations. A significant area, particularly in the upper right, displays a lamellar structure, which is characteristic of pearlite. Other regions of the matrix appear more uniform and equiaxed, consistent with ferrite. The accompanying EDS elemental maps provide crucial information regarding the spatial distribution of the elements.

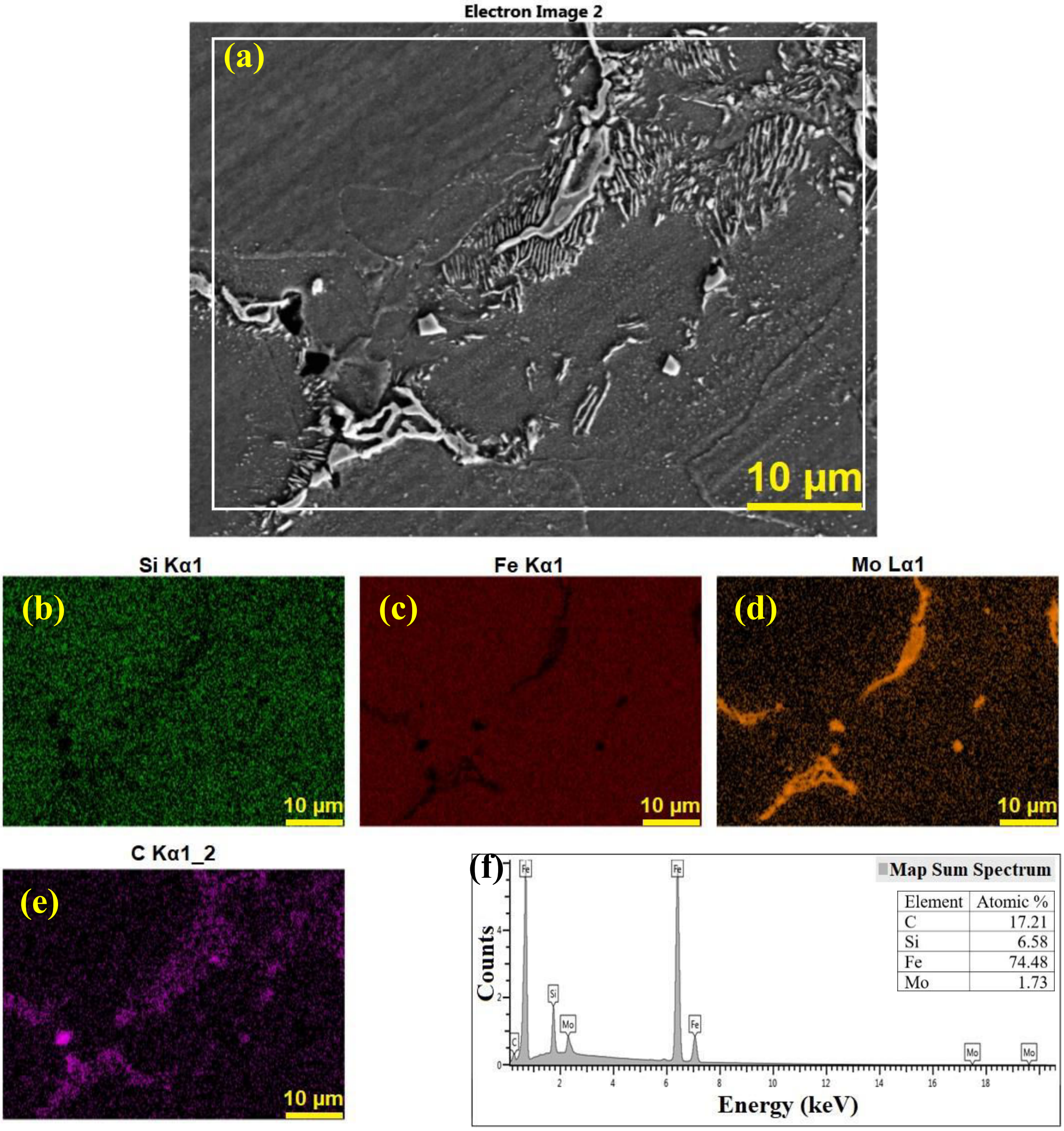

Element	Atomic %
C	17.21
Si	6.58
Fe	74.48
Mo	1.73

Figure 34. (**a**) SEM micrograph, (**b** – **e**) EDS elemental distribution maps of the "Exhaust Manifold" microstructure and (**f**) the corresponding EDS spectrum and elemental composition.

Silicon, Fig. 34(b), is concentrated in the matrix regions surrounding the graphite nodules and the intermetallic regions. This distribution is consistent with silicon's role as a ferrite stabilizer and its tendency to partition preferentially to the ferritic phase. Iron, Fig. 34(c), is ubiquitously distributed throughout the matrix, following the distribution of Si. Slight variations in its intensity may occur, inversely correlating with the concentration of other alloying elements or phases. Molybdenum, Fig. 34(d), exhibits distinct segregation patterns. It is notably concentrated along features that appear to be intermetallic second phases. Some discrete, Mo-rich spots might also be present, suggesting fine Mo-containing precipitates. Carbon, Fig.34(e), shows high concentrations within the graphite nodules. It is also present at elevated levels in the lamellar (pearlitic) region, where it forms part of the cementite (Fe_3C) lamellae that alternate with ferrite lamellae. Fig. 34(f) shows the EDS spectrum and the corresponding element composition and abundance. The silicon content in this mapped area is higher than that reported in the bulk analysis from Fig. 32. This difference may arise if the selected region for mapping is fortuitously richer in ferrite, where silicon preferentially segregates. The molybdenum content in this area confirms its status as a significant alloying element. The combined evidence from the maps confirms that the matrix of this DCI is not purely ferritic but possesses a mixed ferritic-pearlitic microstructure. The observed segregation of molybdenum suggests that Mo may be forming complex carbides or influencing the formation kinetics and stability of pearlite. These Mo-enriched regions or distinct Mo-containing phases represent additional potential sites for hydrogen trapping.

The detailed analysis of the provided SEM images and EDS data reveals a complex microstructure in the ductile cast iron sample, with several features identified as potential hydrogen trapping sites. The strength and density of these traps determine the overall hydrogen accumulation and distribution. Besides the tetrahedral and octahedral sites of BCC iron, which are the reference sites for defining binding energy, lattice defects such as vacancies, dislocations and grain boundaries can act as hydrogen traps. The binding energy values of these traps for ferritic iron (α), that is the predominant phase in our specimen, have been collected in the work of Bhadeshia [94]. Vacancies have the highest values, ranging from 49 to 78 kJ/mol, making a strong trap for hydrogen. Dislocations possess a lower value of binding energy, ranging from 23 to 27 kJ/mol for dislocation strain field, even though dislocation core/ have been measured with a higher value, up to 60 kJ/mol. Other studies [95], indicate a value of ~ 29 kJ/mol for edge dislocation and ~44 kJ/mol for screw dislocations. General grain boundaries binding energy has a value of 32 kJ/mol. Regions of pearlite, characterized by their lamellar structure of alternating ferrite and cementite, were clearly observed. Regarding this phase, hydrogen can occupy interstitial sites within the cementite lattice with binding energies of 33 kJ/mol [96]. These are considered weak to moderate traps. However, some experimental evidence suggests that cementite can act as an irreversible trap, implying either stronger binding or significantly hindered diffusion out of the trap [97]. Defects such as grain boundaries within polycrystalline cementite or carbon vacancies could act as stronger traps. Higher binding energy values have been measured in interfaces between ferrite and cementite. It has been reported [96] a value of 39 kJ/mol. For DCI, the presence of graphite nodulus, and consequently the interface between graphite nodules and the ferrite matrix is of particular importance. Different studies measured the value of the binding energy for the spheroidal graphite that was always in the order of ~ 60 kJ/mol. This makes graphite in cast iron act as a strong hydrogen trap. The presence of (Mo,Ti)C carbides have significant implications for hydrogen trapping. Literature extensively documents that TiC precipitates are potent hydrogen traps, exhibiting binding energies that can range from 80 to 105 kJ/mol, particularly when trapping occurs at carbon-site vacancies within the TiC lattice [98]. The (Mo,Ti)C particles observed are therefore prime candidates for strong, potentially irreversible, hydrogen trapping sites. While some studies [99] on nanosized (Ti,Mo)C precipitates report a binding energy of around 28.9 kJ/mol, the particles in Fig. 33(b) appear substantially larger. It has been suggested that larger, undissolved carbides, such as those observed here, can trap hydrogen strongly. The presence of molybdenum, not only within the large (Mo,Ti)C particles but also at significant concentrations in the area analysed by Spectrum 4 (Fig. 33(e)) suggests a broader role for this element in the material's hydrogen trapping behaviour. Molybdenum could be forming finer carbides, for example Mo_2C, which has been identified as a potential weak trap with a binding energy value of 11-12 kJ/mol [94], be in solid solution within the ferrite, or segregate to various interfaces. Furthermore, significant Mo content was detected in matrix-like regions (Fig. 33(d)). The presence of oxygen, even if modest, could suggest the possibility of oxide inclusions. The interface between them and ferrite matrix can act as strong hydrogen trap [94].

Looking at the stress-strain curves of the ductile cast iron specimen "Exhaust Manifold" shown in Fig. 31, the presence of hydrogen slightly affected the mechanical properties of the material, resulting in a very minor loss of the ultimate tensile strength and an unexpected increase of ductility. Considering this, is it realistic to think that a homogeneous distribution of the hydrogen traps reduced the concentration of diffusible hydrogen, but without allowing it to accumulate excessively in critical areas, which could have led to crack nucleation.

The fracture surface images of ductile iron specimens, Fig. 35(a) and Fig. 35(b) show similar images, confirming the SSRT results. Under tensile loading, uncharged ductile cast iron typically fails in a ductile manner via microvoid coalescence, owing to its notable tensile ductility. In contrast, the presence of dissolved hydrogen can embrittle the material, significantly reducing ductility and altering the fracture mode. In this case, instead, both specimens show a mix ductile-brittle cleavage, or quasi-cleavage, fracture. The ductility, present, but not in typical values of ductile cast irons [88], [100], can be attributed to growth of several large voids or cavities on the fracture surface, corresponding to the locations of graphite nodules. Ductile cast iron's graphite nodules typically act as void nucleation sites: under tensile stress, the graphite/matrix interface can decohere, or the graphite itself (being brittle) may fracture or dislodge, leaving a roughly spherical cavity. The brittle aspect of the fracture can be attributed to the presence brittle cleavage-like facets in the matrix, among the graphite nodules remaining on the surface and the cavities left where these nodulus have been detached. These facets are flat, shiny regions on the fracture surface, signifying that portions of the matrix failed by cleavage (transgranular brittle fracture) rather than by microvoid. growth. Under the SEM, these facets may appear as large, flat patches often bounded by jagged edges where they intersect other facets. Some facets may show subtle river patterns or feather markings that indicate crack propagation direction within a grain.

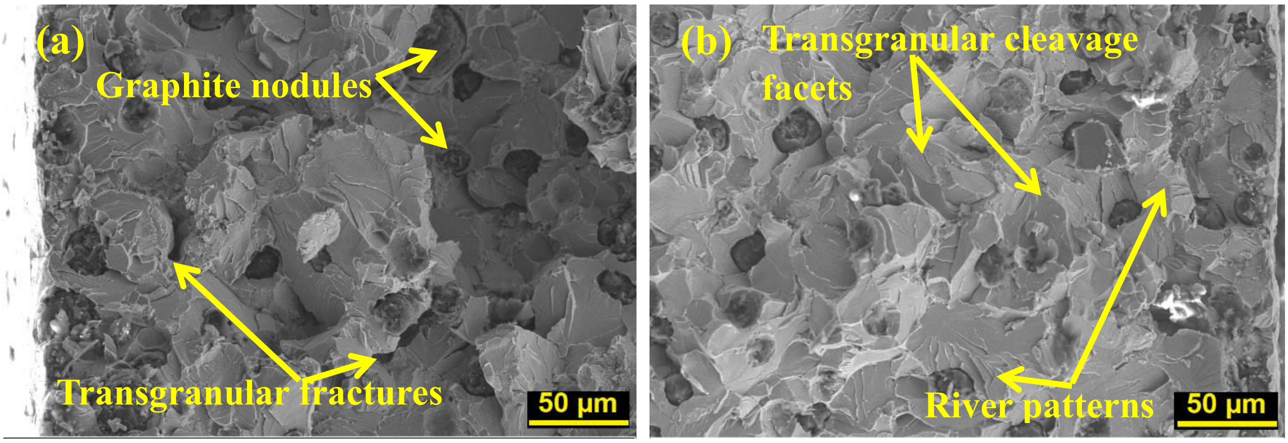

Figure 35. SEM micrographs of the fracture surfaces of the (**a**) uncharged and (**b**) charged "Exhaust Manifold" specimens.

Upon examining the fracture surface, one can observe scattered tiny cracks on some cleavage facets or between dimples. The presence of these secondary cracks is a telltale sign of hydrogen embrittlement: they indicate that multiple brittle crack fronts initiated and propagated independently before merging, or that the main crack spawned side-cracks due to local brittleness. The fractographic features above point to a significant influence of hydrogen on the failure mode.

Two primary hydrogen embrittlement mechanisms can explain these observations: Hydrogen-Enhanced Decohesion (HEDE) and Hydrogen-Enhanced Localized Plasticity (HELP). In addition, a hydrogen-induced internal pressure effect at the graphite interfaces may contribute. These mechanisms are not mutually exclusive, hydrogen's effect on fracture is often a combination of several processes. The observations support both hydrogen-enhanced decohesion (HEDE) and hydrogen-enhanced localized plasticity (HELP) operating in tandem. Hydrogen atoms embrittled internal interfaces and likely lowered cohesive strength at the atomic level, leading to cleavage facets and easy nodule debonding (a HEDE effect) Simultaneously, hydrogen promoted highly localized deformation at crack tips (HELP), enabling voids to nucleate but then rapidly propelling cracks with little further plasticity. The possibility of hydrogen gas forming at the nodule interfaces also contributed to the interfacial crack propagation.

9.2.2 Grey cast iron (Engine block)

The grey cast iron "Engine Block" specimens show a brittle behaviour: the WHC specimen yields at 252 MPa and has a UTS of 307 MPa with only 0.97% elongation at failure, while the HC specimen yields at 254 MPa and fractures with a 0.67% elongation and reaches a UTS of 286 MPa. Both curves are steep and short, reflecting the inherently low ductility of grey iron. This is also demonstrated by the values of L_{σ} and L_{ε}. Compared to Al–Si alloys, grey iron fails in a more brittle manner. In summary, the "Engine Block" SSRT curves (with and without hydrogen) reflect a largely brittle matrix controlled by graphite flakes; hydrogen accelerates fracture slightly, but the fracture features (cleavage through the ferrite regions) are dominated by the graphite structure.

Grey cast iron (GCI) is a prominent engineering alloy belonging to the family of cast irons, primarily composed of iron, carbon (typically >2 wt.%), and silicon (commonly 1-3 wt.%). It is distinguished by its microstructure, in which a significant portion of the carbon content exists as graphite flakes. Fig. 36 shows a detailed view of the microstructure of a grey cast iron sample. In Fig. 36(a) there is low-magnification overview of the GCI microstructure. The dominant features are the dark, elongated, and in some case curved graphite flakes, randomly oriented and dispersed within a lighter-contrast metallic matrix. According to the ISO 945-1:2019 [101] the observed morphology, characterized by a uniform distribution and random orientation of flakes, is consistent with Type A. Fig. 36(b) provides a magnified view of the matrix from the region indicated in Fig. 35(a). The characteristic lamellar structure of pearlite is clearly resolved. Pearlite consists of alternating lamellae of ferrite (α-Fe, appearing darker) and cementite (Fe_3C, appearing lighter). A distinct, irregularly shaped particle, approximately 2-3 μm in size and exhibiting a brighter contrast than the pearlite, is identified as a MnS inclusion.

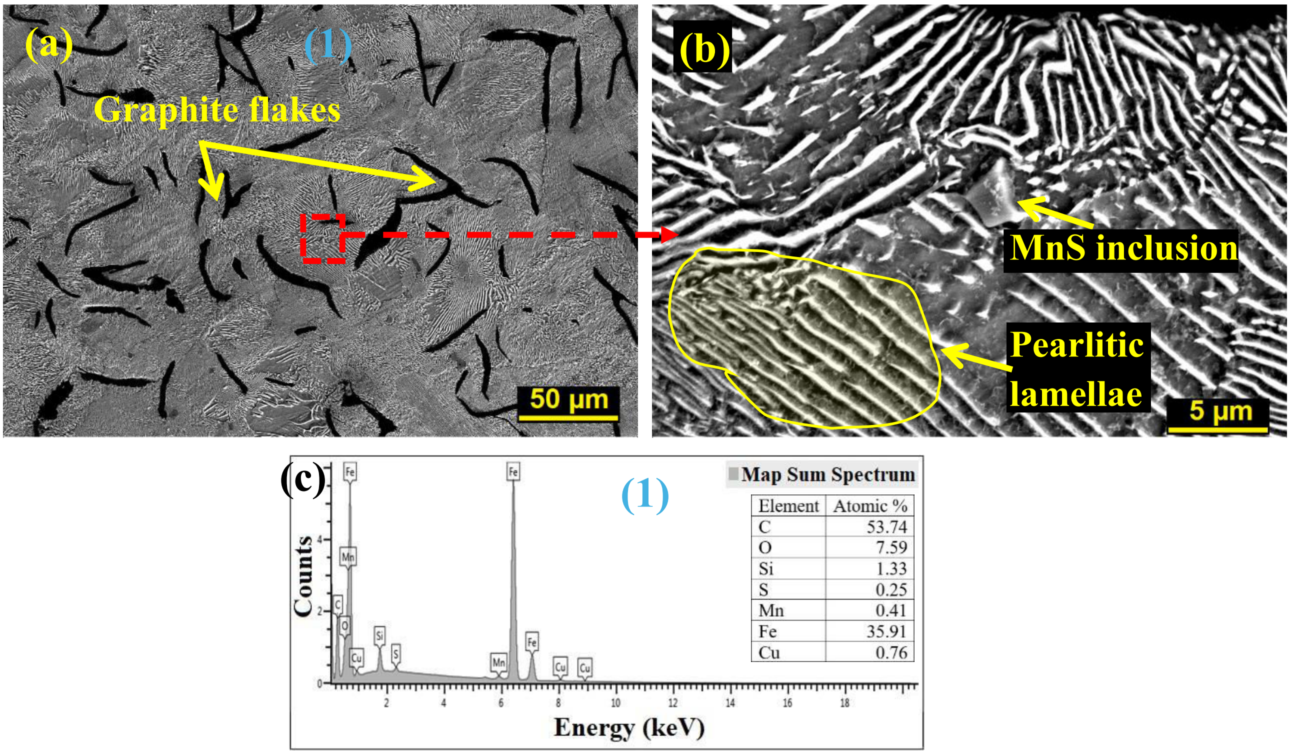

Map Sum Spectrum

Element	Atomic %
C	53.74
O	7.59
Si	1.33
S	0.25
Mn	0.41
Fe	35.91
Cu	0.76

Figure 36. (**a**) SEM micrograph, (**b**) higher magnification of the microstructure of the "Engine Block" specimen and (**c**) the corresponding EDS spectrum and the elemental composition.

The EDS spectrum in Fig. 36(c) represents the area of shown in Fig. 36(a), encompassing multiple graphite flakes and the surrounding pearlitic matrix. The high carbon content is attributed to the significant volume fraction of graphite flakes within the analysed area. Iron is the main component of the metallic matrix phases (ferrite and cementite). Silicon is a key alloying element in GCI, promoting graphitization and typically dissolving in ferrite. The presence of manganese and sulphur suggests the potential formation of manganese sulphide (MnS) inclusions. Copper is present as a minor alloying element or an impurity. The oxygen signal may arise from surface oxidation, oxygen-containing inclusions not clearly resolved in the low-magnification SEM image, or analytical artifacts.

Fig. 37(a) displays a higher magnification view of the pearlitic lamellae. A yellow line, designated A-B, indicates the path for an EDS line scan, traversing several ferrite and cementite lamellae over approximately 10.5 µm.

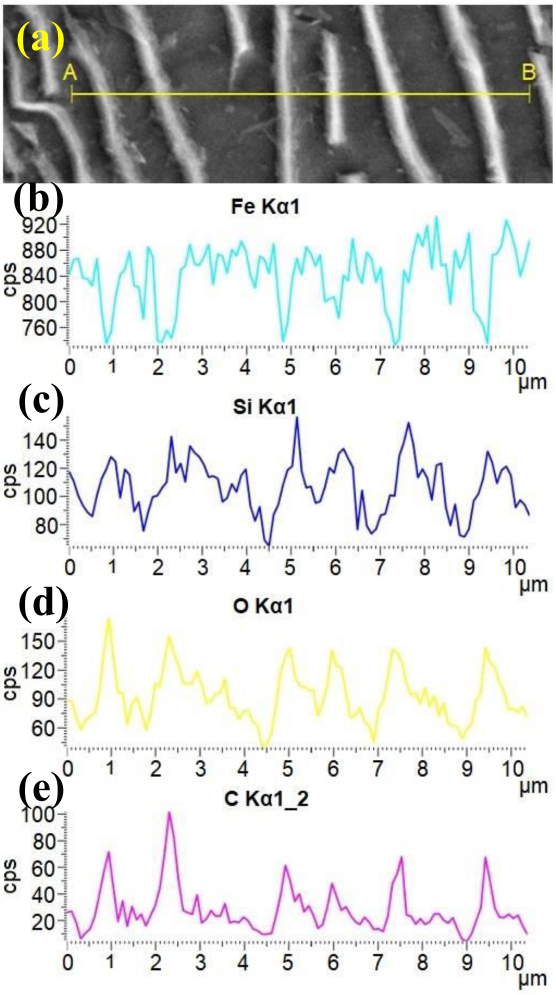

Figure 37. (**a**) SEM micrographs and (**b** – **e**) linear EDS elemental distribution of the pearlitic structure of the "Engine Block" specimen.

The Fe signal, Fig. 37(b) shows relatively consistent high counts across the scan, as both ferrite and cementite are iron-based phases. Minor fluctuations may exist due to the differing Fe content per unit volume in ferrite versus cementite (which contains 6.67 wt% C). The Si profile, Fig. 37(c), exhibits distinct peaks and troughs. Silicon has significantly higher solubility in ferrite than in cementite. The peaks in Si concentration correspond to the interfaces between ferrite and cementite lamellae, sign that it precipitates at phase boundary. The oxygen signal, Fig. 37(d), shows some fluctuations but does not strongly correlate with the primary phases. This could be due to minor, uniformly distributed surface oxidation or noise. The carbon profile, Fig. 37(e) shows an inverse relationship with the iron profile. Higher carbon concentrations are expected in the cementite lamellae (Fe_3C) and very low concentrations in the ferrite lamellae. The distinct chemical difference between the lamellae, evident from the elemental partitioning, could lead to localized variations in hydrogen solubility and diffusivity at a very fine scale. This may also influence the nature of the ferrite/cementite interface as a hydrogen trap.

Fig. 38(a) shows another region of the GCI, highlighting locations where EDS analyses were performed. "Spectrum 14", Fig. 38(b), was acquired from an angular, greyish particle embedded within the pearlitic matrix. "Spectrum 15", Fig. 38(c) was taken from a graphite flake.

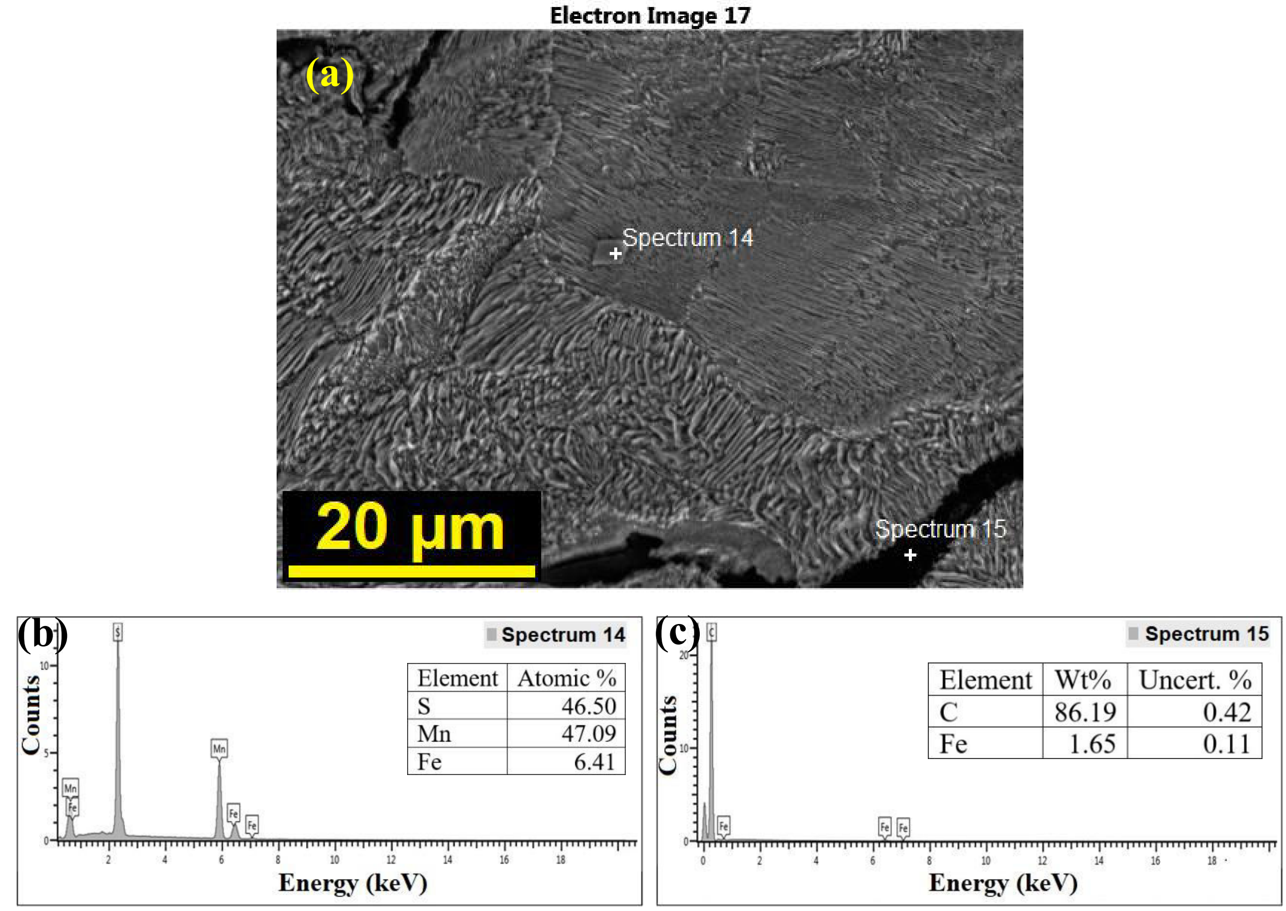

Element	Atomic %
S	46.50
Mn	47.09
Fe	6.41

Element	Wt%	Uncert. %
C	86.19	0.42
Fe	1.65	0.11

Figure 38. (**a**) SEM micrograph indicating the sites for the EDS analysis and (**b**, **c**) the corresponding EDS spectra and elemental composition.

The elemental composition for the spectrum of Fig. 38(b) shows a nearly 1:1 atomic ratio between manganese and sulphur, that strongly indicates that this inclusion is manganese sulphide (MnS). MnS inclusions are common in cast irons and steels and are known to influence mechanical properties and machinability. The minor iron signal could be due to excitation of the surrounding matrix by the electron beam or some limited solubility of iron in the MnS. The clear identification of MnS inclusions is significant, as literature strongly suggests that MnS can act as an effective hydrogen trap. In the spectrum shown in Fig. 38(c) the preponderance of carbon confirms that this feature is a graphite flake. The small percentage of iron detected is likely due to interaction of the electron beam with the underlying or adjacent matrix material.

Hydrogen trapping occurs when hydrogen atoms segregate to microstructural defects or interfaces where their chemical potential is lower than in the regular lattice interstitial sites. Trapping sites, such as vacancies, dislocations and grain boundaries and their binding energies values relative to α-Ferrite, pearlite and graphite have already been reported when discussing their effects on ductile cast iron. There aren't specific studies on graphite flakes in grey iron, but by analogy the trap energies should be like those of spheroidal graphite. Inclusion, such as MnS present in Fig. 38, can act as a trap for hydrogen. Studies [94] on the binding energy of MnS in a ferritic matrix report values of 72 kJ/mol for both a generic MnS entity, such as an inclusion, and for the interface between the inclusion and the ferritic matrix, resulting in a very strong trap for hydrogen.

Based on the stress-strain curves of the gray cast iron specimen "Engine Block" shown in Fig. 31, the presence of hydrogen resulted in a loss of mechanical properties. Considering the brittle behavior of both specimens, it is possible to think that the presence of relatively strong traps, rather than limiting the presence of diffusible hydrogen, it may have caused an increase in the concentration of hydrogen at the graphite lamellae and their interfaces with the perlite matrix, causing them to detach or promoting the growth and propagation of microcracks from them, which under normal conditions would not have occurred.

Fig. 39 (a) reveals a morphology consistent with brittle fracture of grey cast iron. They appear as irregular, flat or slightly concave regions often darker in the SEM (due to the carbon material or cavities left by detached flakes). The fracture likely initiated at a graphite flake, or at multiple flakes almost simultaneously. Graphite flakes act as built-in crack starters: their sharp tips concentrate stress and are known initiation sites under tensile load [102]. In grey cast iron, fracture occurs mostly along graphite flake boundaries; in other words, the crack path preferentially travels through or around the graphite flakes, since these are the weak links in the structure. On the SEM image, the graphite regions may be discerned by their shape (elongated, sharp-edged outlines) and a relatively smoother texture compared to the metal matrix. Between the graphite flakes, the iron matrix has failed in a brittle manner, showing cleavage facets. The presence of abundant flat facets and river markings confirms that the crack propagated in a brittle, transgranular fashion (cleavage-like). However, the concurrent observation of tear ridges and dimple-like microvoid areas means the fracture was not a single uninterrupted cleavage plane. The dominance of quasi-cleavage facets confirms the very low ductility of the fracture: the matrix did not undergo significant plastic void growth but instead cracked abruptly. Based on the above evidence, the fracture in this grey cast iron sample can be classified as quasi-cleavage. Though grey cast iron is predominantly brittle, microvoids (dimples) can be present in isolated regions of the fracture, typically in the small “ligaments” of metal that were between graphite flakes, as shown in Fig. 39(b). These are dimples resulting from microvoid coalescence, a ductile fracture mechanism. In grey iron tensile fractures, the matrix ligaments between flakes may undergo limited plastic deformation before breaking, forming microvoids around the tips of the graphite or other inclusions. Overall, the fracture surface is not dominated by a fibrous or dimpled aspect, instead the dimples appear only in localized patches, reinforcing that the primary fracture mode was brittle cleavage with only minor ductile tearing in constrained areas. In conclusion, the fractographic features (cleavage facets with river patterns, plus intervening ridges and microvoid textures) and the known behaviour of grey cast iron support that the failure occurred by quasi-cleavage. The crack propagated in a brittle fashion through the matrix but was repeatedly blunted or diverted by the graphite flakes, resulting in cleavage-like facets separated by small tearing steps. This classification is consistent with the brittle yet non-ideal nature of fracture in grey cast iron: it is very brittle, but not a textbook single-plane cleavage fracture. The observed fracture morphology, cleavage dominated but with slight plasticity features, is thus well explained as quasi-cleavage, aligning with the metallurgical principles of how grey cast iron fails in tension.

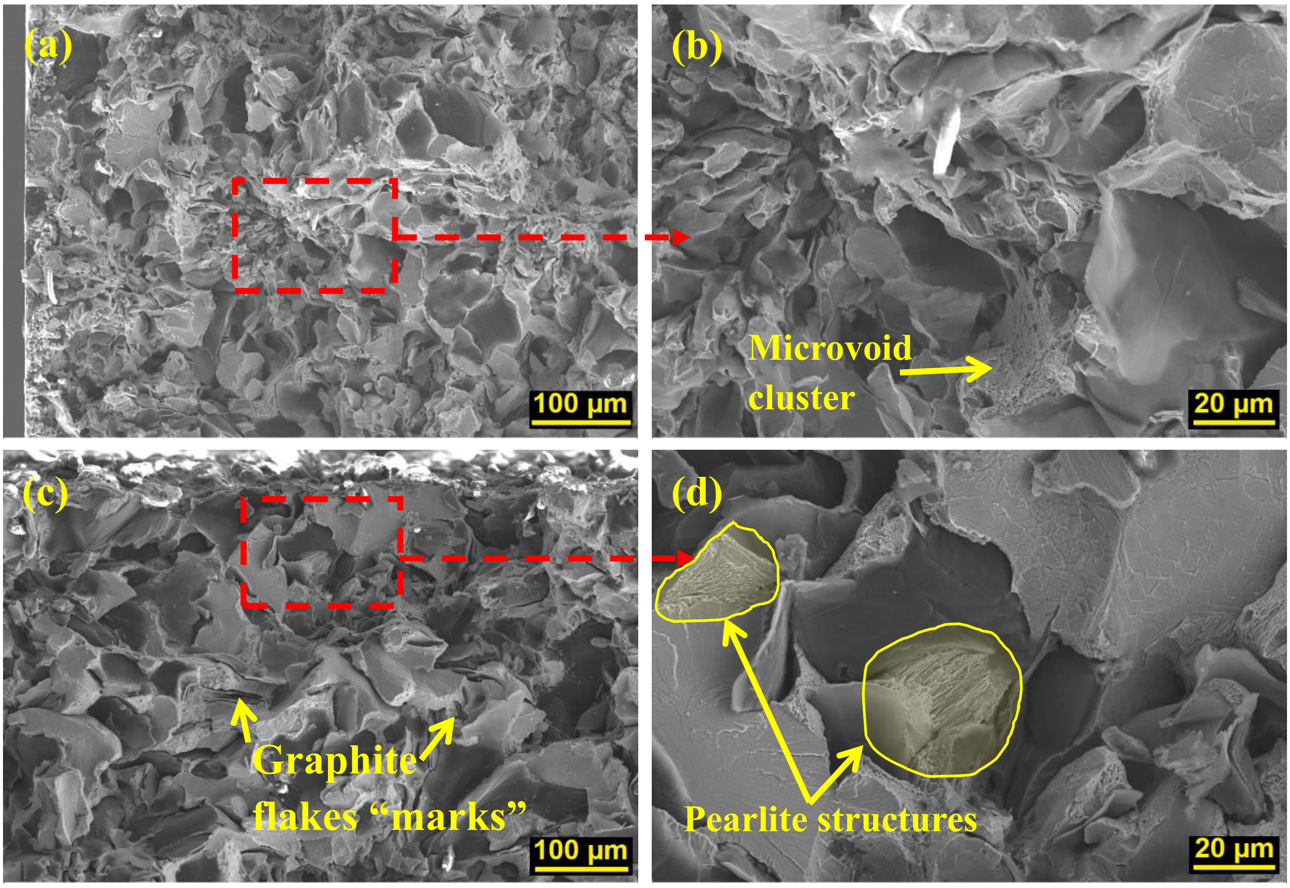

Figure 39. SEM micrographs of the fracture surfaces (**a**, **b**) of the uncharged “Engine Block” specimen at different magnification and (**c**, **d**) of the charged Engine Block specimen at different magnification.

The hydrogen charged grey cast iron fracture surface shown in Fig. 39(c) looks very similar to the uncharged one, with the same mix of cleavage and quasi-cleavage features; only very subtle changes are apparent. Large, planar facets cover much of the surface, indicative of cleavage-like fracture in the metal matrix. These facets are relatively smooth in appearance, suggesting the crack propagated rapidly through the matrix with little plastic deformation. Graphite flake interactions are evident as well: and one can discern cavity-like regions or indentations where graphite flakes were embedded. Many graphite flakes appear to have detached from the matrix during fracture, leaving behind voids or smooth impressions of their shape. The surrounding matrix between flakes failed by transgranular cracking; the facets often terminate or initiate at the sites of the graphite flakes. There is an absence of the fine dimpled texture associated with ductile microvoid coalescence. The overall appearance is a jagged, rock-like fracture surface composed of cleavage facets and stepwise features, with cracks having branched and linked between graphite flakes (some crack deflection occurs as cracks navigate from one flake to the next, but locally the fracture path between flakes is fairly straight on cleavage planes). There is no clear evidence of intergranular fracture (grain boundary separation) on this surface; the crack path runs through the matrix rather than along grain boundaries, albeit often along the graphite/matrix interface. In summary, the hydrogen-charged sample’s fracture surface is characterized by brittle, cleavage-dominated fracture with graphite flakes acting as crack initiation and propagation sites, producing faceted cavities and sharply defined crack surfaces. The high-magnification image, Fig. 39(d) of the hydrogen-charged grey cast iron fracture surface, shows brittle fracture features. At this scale, the fracture surface is dominated by large, flat cleavage facets in the iron matrix. These facets are separated by jagged tear ridges and step-like features: elevations between adjacent facets where cracks from different planes have joined. In some areas the crack has split into multiple paths (crack bifurcation), evident where a cleavage facet forks into two. Upon close examination, one can also see small microvoids (tiny dimples) along certain facet edges and near former graphite locations, indicating limited micro-ductile tearing. Additionally, there are smooth regions or cavity-like impressions corresponding to graphite interface decohesion: places where graphite flakes pulled out or separated from the iron matrix, leaving behind voids or flat imprints on the fracture surface. The combination of these features indicates a quasi-cleavage fracture mode rather than a perfectly planar cleavage. The facets appear cleavage-like but exhibit fine-scale ridges and occasional dimples, characteristics of hydrogen-induced quasi-cleavage. In hydrogen-embrittled grey cast iron, absorbed hydrogen weakens the iron matrix and the graphite–matrix interfaces, promoting brittle crack propagation through the matrix (forming cleavage-like facets) and along graphite interfaces (causing decohesion). The observed tear ridges and crack branching suggest the crack front was deflected by microstructural obstacles (such as graphite flakes or grain boundaries), with slight plastic deformation needed to link neighbouring facets.

The uncharged grey cast iron specimen's fracture surface shares some broad similarities with the hydrogen-charged sample, yet clear differences in detail reflect the influence of hydrogen. Both samples show a rough fracture profile governed by the cast iron's graphite flake structure: in each case, cracks initiated at graphite flakes and propagated through the iron matrix, resulting in a grey, matte fracture surface typical of grey cast iron. In both fractographs, we see a network of overlapping facets and flakes: the sharp, irregular shape of the features is due to fracture passing through the matrix around the graphite. The presence of microvoids (dimples from void coalescence) is more apparent in the uncharged fracture (though still quite limited, given grey cast iron's inherent brittleness) and much less so in the hydrogen-charged fracture. In the uncharged sample, if one were to examine at higher magnification, one might find small microvoid dimples nucleated at the tips of graphite flakes or around other second-phase particles. These microvoids coalesced to form the final fracture between flakes, giving the fracture surface a slightly fibrous texture in some areas. In the charged specimen instead, hydrogen directly suppresses this void growth by facilitating easier crack propagation before voids can coalesce.

This aligns with the concept of hydrogen-enhanced localized plasticity (HELP) and hydrogen-enhanced decohesion (HEDE) mechanisms: hydrogen can either promote dislocation motion at very small scales (causing localized slip that leads to void nucleation) or, more commonly in brittle matrices, reduce cohesive strength (leading to cleavage before noticeable void growth). In grey cast iron, the embrittlement is dominated by HEDE at the graphite interfaces and within the ferritic lamellae, so the usual microvoid process is curtailed. The result is the lack of ductile dimples in the hydrogen-charged fracture surface, as observed. Neither sample shows pronounced intergranular fracture characteristics at the scale of observation: the fracture in both appears to cut through the matrix rather than follow grain boundaries.

In conclusion, the hydrogen-charged grey cast iron failed in a more brittle fashion compared to the uncharged specimen. The hydrogen introduced prior to testing led to enhanced embrittlement: it weakened the iron matrix (promoting cleavage fracture), and the graphite flake interfaces (causing early separation and crack initiation at those sites). Consequently, the hydrogen-charged fracture surface shows larger cleavage facets, more frequent graphite-matrix interface failures, and fewer ductile features, whereas the uncharged fracture surface, while still generally brittle, retains slightly more evidence of ductile crack growth (smaller facets, minor microvoid coalescence between flakes).

10. Case study

Spark plugs are critical components in internal combustion engines, responsible for igniting the air-fuel mixture within the combustion chamber. In hydrogen-fuelled engines, the unique combustion characteristics of hydrogen, such as its wide flammability range and high flame speed, pose distinct challenges to spark plug materials and design. Moreover, the presence of hydrogen can lead to material degradation phenomena, notably hydrogen embrittlement, which compromises the mechanical integrity of metallic components.

This case study examines the effect of the working conditions of the spark plug and the engine head of a H_2ICE after using hydrogen as fuel. Scanning Electron Microscopy (SEM), Energy Dispersive Spectroscopy (EDS) and microhardness testing have been used to characterize microstructural changes and elemental distributions post-exposure.

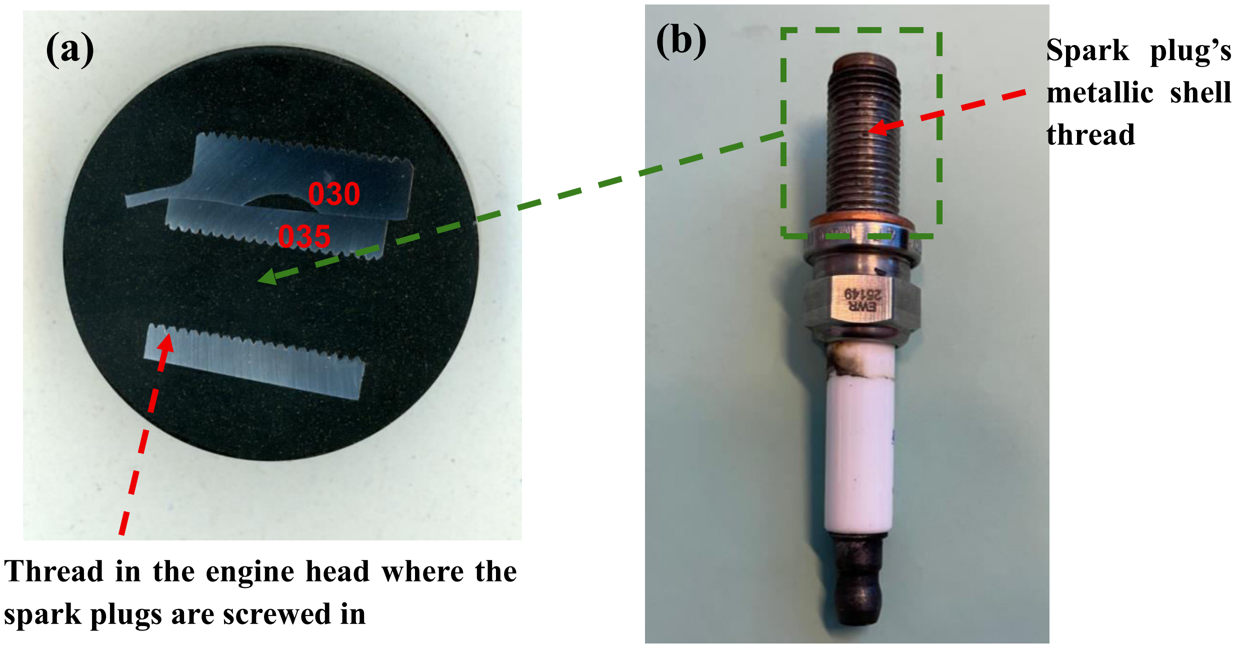

Figure 40. (**a**) Specimens cut from the engine head and mounted. (**b**) Spark plug

Fig. 40(a) shows different specimens, labeled "030", "035", which were extracted from the engine head. These specimens feature the threaded profile corresponding to the spark plug bore. Specimen "30", was subjected to further detailed analysis, including hardness testing. Fig. 40(b) displays the spark plug post-service. The ceramic insulator shows some light brownish discoloration, typical of exposure to combustion environments. The metallic shell, particularly the threaded portion, appears to have accumulated some deposits and exhibits a dull, slightly discolored surface. The threads themselves are the primary area of interest for subsequent detailed analysis due to their direct engagement with the engine head.

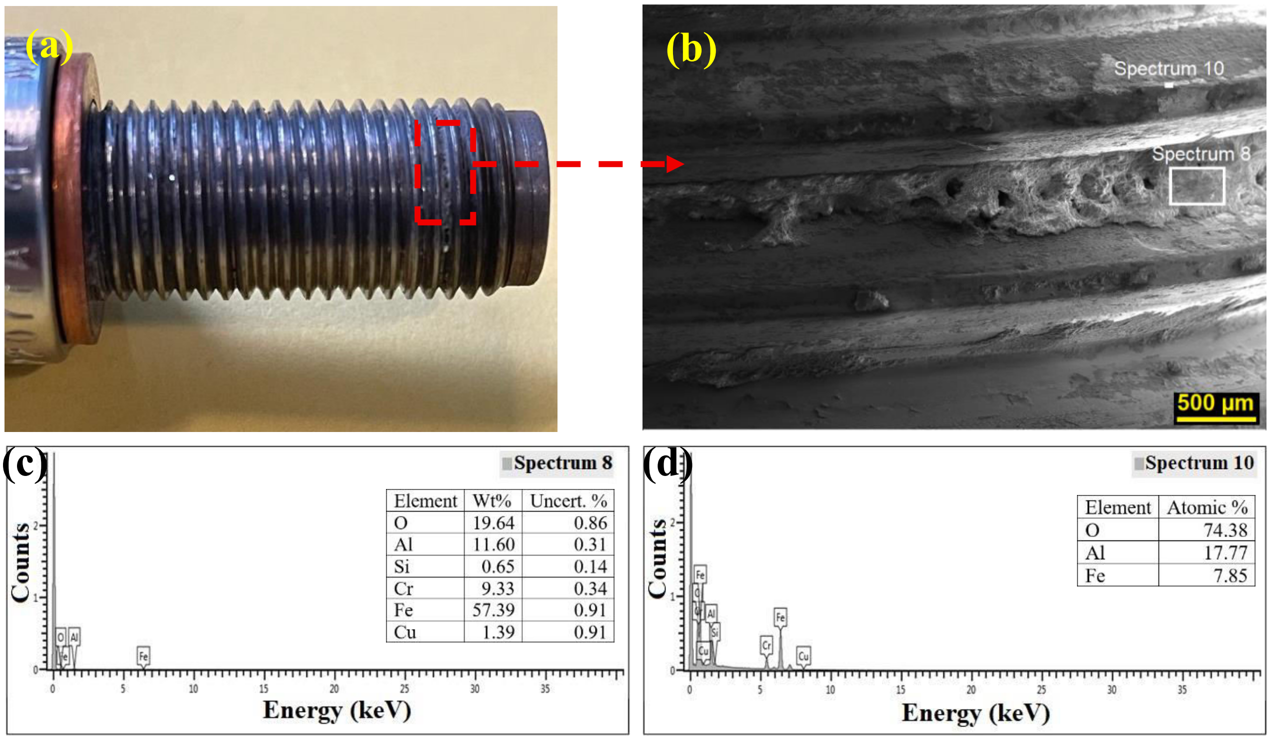

Spectrum 8

Element	Wt%	Uncert. %
O	19.64	0.86
Al	11.60	0.31
Si	0.65	0.14
Cr	9.33	0.34
Fe	57.39	0.91
Cu	1.39	0.91

Spectrum 10

Element	Atomic %
O	74.38
Al	17.77
Fe	7.85

Figure 41. (**a**) Metallic shell and (**b**) SEM magnification. (**c**, **d**) EDS spectra and elemental distribution

Fig. 41(a) provides a closer view of the spark plug's metallic shell thread. Visible accumulations of foreign material are evident on the thread flanks and within the thread roots. The areas highlighted by red dashed boxes indicate regions with more substantial build-up, suggesting material transfer or localized reaction product accumulation. The SEM micrograph in Fig. 41(b), taken at a 500 µm scale, reveals the morphology of the deposits and the underlying thread surface. The material on the threads, particularly in the regions designated for Spectrum 8 and Spectrum 10, appears porous, somewhat clumpy, and irregularly distributed. The underlying thread surface exhibits considerable roughness and evidence of mechanical damage, consistent with wear processes.

Spectrum 8, Fig. 41(c), with significant Fe and Cr, clearly point to the spark plug as a Fe based alloy. The presence of Al and Si in this spectrum indicates material transfer from the Al-Si engine head. The substantial oxygen content across both spectra signifies that these metallic elements have undergone oxidation, a process accelerated by the high temperatures and water vapor present in the H_2ICE combustion chamber. Spectrum 10, Fig. 41(d), being rich in Al and O, further reinforces the transfer of aluminum from the engine head and its subsequent oxidation. The detection of copper in Spectrum 8 is also noteworthy, as Cu is present in the engine head alloy.

The primary chemical byproduct of hydrogen combustion is water vapor. At the high operating temperatures characteristic of an ICE, the Al-Si alloy engine head will inevitably undergo oxidation. The presence of high concentrations of water vapor can significantly influence this oxidation process, often accelerating it compared to oxidation in dry air or less humid environments [103]. Al-Si alloys are known for their propensity to oxidize at high temperatures, primarily forming a surface layer of aluminum oxide (Al_2O_3). The interaction between aluminum and water vapor at high temperatures can not only lead to oxide formation but also contribute to hydrogen absorption by the alloy. The stainless-steel surface itself would typically be protected by a thin, passivation layer of chromium oxide (Cr_2O_3). However, the mechanical interaction during spark plug installation/removal and potentially during engine operation (due to vibration and thermal expansion differences) can disrupt this passivation layer.

The spark plug's metallic shell is also exposed to the hydrogen-rich environment. If HE were to occur in the stainless-steel threads, it would typically manifest as a loss of ductility, a reduction in fracture toughness, and an increased rate of fatigue crack growth under cyclic loading. Hydrogen atoms can be absorbed from the gaseous environment, especially at elevated temperatures, and diffuse into the steel lattice. The thread, being subjected to both assembly stresses and cyclic operational stresses (thermal and mechanical), could be vulnerable if the material's resistance to hydrogen is compromised.

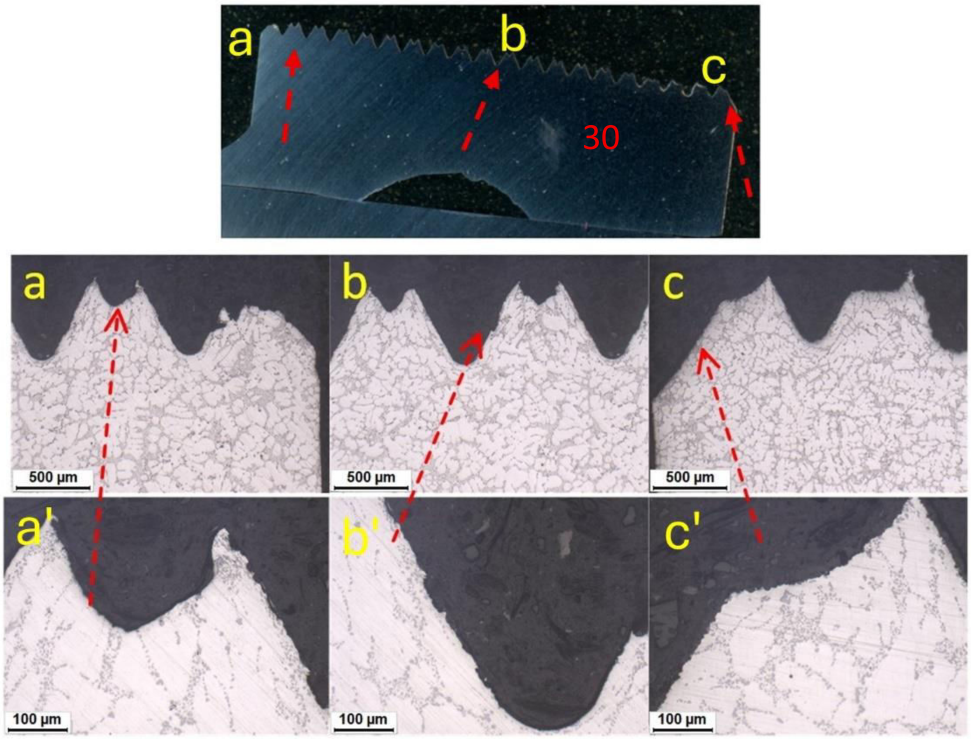

Figure 42. Engine head specimen. (**a**, **b**, **c**) SEM micrographs in different sites and (**a'**, **b'**, **c'**) corresponding magnifications.

Fig. 42 presents the micrographs of a thread profile from one of the engine head specimens. The top overview image indicates three locations (a, b, c) chosen for higher magnification views. The magnified images (a, b, c, and further enlargements a', b', c') reveal the microstructure at the thread root and flank. A typical cast Al-Si alloy microstructure is evident, characterized by lighter-etching α-Al dendrites and darker grey, interdendritic eutectic Si particles. Notably, location 'b' at the thread tip seems to exhibit some degree of deformation or wear, suggesting mechanical interaction during service or spark plug installation/removal.

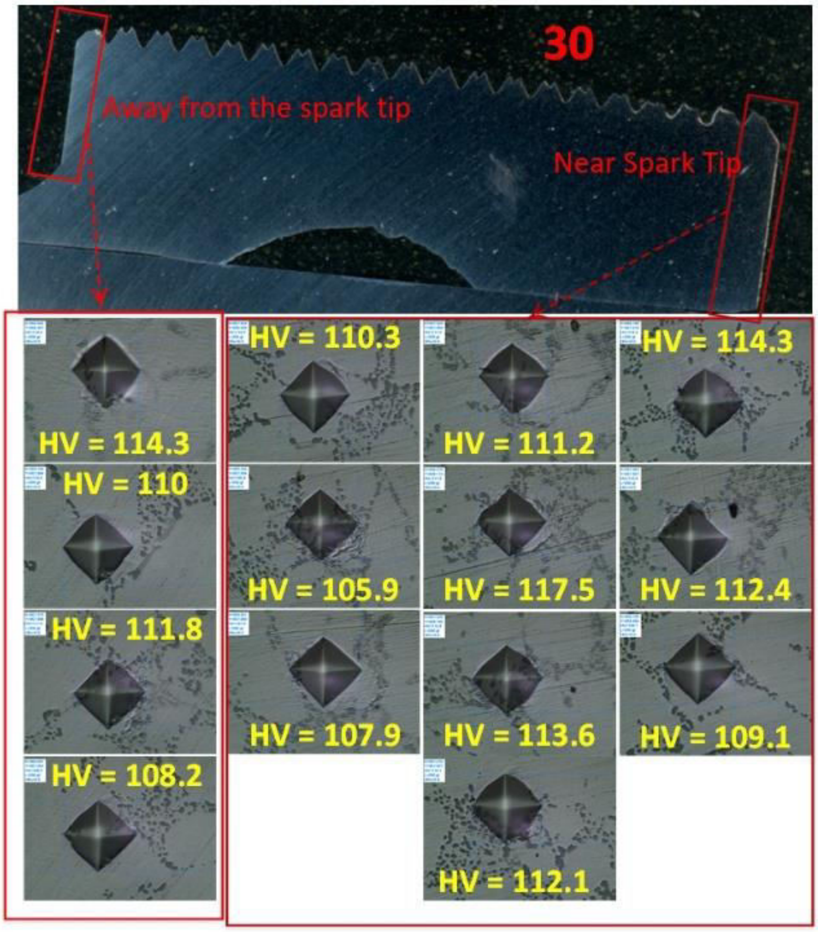

Figure 43. Engine head specimen and result from the microhardness test in different sites.

Fig. 43 shows the Vickers microhardness tests that were conducted on specimen "30" from the engine head, with indentations made in two distinct regions: "Away from the spark tip" and "Near Spark Tip". The average Vickers microhardness in the region "Near Spark Tip" (111.4 HV) is almost identical to that in the region "Away from spark tip" (111.1 HV). The difference in average hardness is only 0.3 HV. Given the standard deviations (2.6 HV for "Away" and 3.3 HV for "Near") and the inherent variability in microhardness measurements on heterogeneous materials like cast Al-Si alloys, this extremely small difference is highly unlikely to be statistically significant. This suggests that, based on the current hardness measurements, there is no clear evidence of substantial localized hardening or softening in the region near the spark tip compared to an area further away.

11. Conclusion

This investigation evaluated the hydrogen embrittlement (HE) susceptibility of specific Al-Si alloy and cast iron components sourced from a hydrogen-fuelled internal combustion engine.

1. The "Engine Head" specimens demonstrated significant susceptibility to HE. Hydrogen charging resulted in a substantial reduction in ductility by ~ 67.31% while the ultimate tensile strength (UTS) just decreased slightly, about 7.95%. Fractographic analysis of the uncharged material revealed a ductile fracture mode characterized by dimple rupture. In contrast, the hydrogen-charged specimens exhibited a mixed-mode fracture.
2. The "Piston Blank" displayed an atypical response to hydrogen charging showing an increase in both the UTS (27.19%) and in elongation at failure (38.60%) after hydrogen charging. It is crucial to note, however, that both uncharged and charged specimens exhibited very low intrinsic ductility. The thesis suggests that this unexpected behaviour might be attributed to insufficient hydrogen diffusion into the bulk during the charging period. Despite the increased tensile parameters, the fractographic analysis shown that the fracture mode in both conditions was predominantly brittle-like as expected by the presence of coarse and hard second phases particles and IMCs.
3. The cast iron components also showed distinct behaviours. The ductile cast iron (DCI) specimens shown minimal change in UTS, by ~ 2.88% but, unexpectedly, a slight increase in elongation at failure (15.36%) after hydrogen charging. The overall elongation values, however, were still low for a typical DCI. Fractographic analysis revealed a mixed ductile-brittle (quasi-cleavage) fracture mode for both uncharged and charged conditions.
4. The grey cast iron (GCI) "Engine Block" specimens, an inherently more brittle material, showed a clear degradation in mechanical properties upon hydrogen charging, with a reduction of UTS of by ~ 6.64% and a significant reduction in ductility by about 31.44%.
5. Despite the lack of a significant measured hardness difference, the area immediately surrounding the spark plug tip is subjected to the most extreme conditions within the combustion chamber. Hydrogen from combustion can diffuse into aluminum alloys, especially at elevated temperatures. The formation of substantial deposits on the spark plug threads, composed of material transferred from the engine head (Al, Si, Cu) and elements from the spark plug itself (Fe, Cr), all subsequently oxidized, is a direct consequence of adhesive wear, specifically galling. This process is exacerbated by the high mechanical loads experienced during spark plug installation and the demanding operational environment.

12. Limitations and future perspectives

1. Several limitations should be acknowledged when interpreting the findings of this research. The study primarily utilized a single set of electrochemical hydrogen charging parameters and one slow strain rate. HE susceptibility can be highly sensitive to hydrogen concentration, charging method (e.g., gaseous vs. electrochemical), strain rate, and temperature. The number of specimens tested for each condition have been limited, which can affect statistical confidence, particularly for the atypical results observed. Quantitative characterization of hydrogen content within the specimens post-charging was not reported, making it difficult to directly correlate observed mechanical effects with specific hydrogen concentrations. The study focused on base material properties; the influence of manufacturing features like welds or surface treatments was not investigated.
2. Based on the findings and limitations of this study, there are some suggestions that can be followed for possible future research. First, investigate the effect of varying hydrogen charging conditions (e.g., different current densities, charging times, use of gaseous hydrogen charging to simulate engine environments more closely) and a wider range of strain rates and temperatures on the HE susceptibility of these alloys.
3. Conduct dedicated studies to understand the mechanisms behind the increased strength/ductility observed in the "Piston Blank" Al-Si alloy and the increased ductility in the ductile cast iron after hydrogen charging. This should include careful control of experimental variables and detailed microstructural investigation at various stages of hydrogen exposure and deformation. These anomalies may point to complex hydrogen-trap interactions at specific hydrogen concentrations or microstructural states.
4. Employ techniques such as Thermal Desorption Spectroscopy (TDS) to quantify the amount of hydrogen absorbed and to characterize the binding energies and densities of different trap sites within the microstructures. This would allow for a more direct correlation between hydrogen content, trap characteristics, and mechanical behavior. Utilize advanced techniques such as Electron Backscatter Diffraction (EBSD) for detailed crystallographic analysis of fracture paths and hydrogen-induced deformation, and Transmission Electron Microscopy (TEM) for observing hydrogen interactions with dislocations and nanoscale features in-situ or ex-situ.
5. If feasible, conduct more tests on actual components or sub-assemblies under conditions that more closely simulate the complex stress states, thermal cycles, and hydrogen environment experienced in an operating H_2ICE. Develop or apply existing models to simulate hydrogen diffusion, trapping, and its effect on mechanical behavior in these complex alloys to complement experimental findings and guide material design.
6. Following the results obtained from the case study, other specific recommendations are proposed to enhance the durability and reliability of components in H_2ICEs. Further investigate alternative material pairings for the spark plug and engine head thread to minimize galling, implement surface coatings or treatments on either the Al-Si engine head thread or the spark plug thread, emphasize the critical importance of using appropriate anti-seize compounds or lubricants during spark plug installation and conduct more targeted investigations into the HE susceptibility of the specific materials used.
7. Looking ahead, H_2ICEs present a pragmatic and economically viable route to decarbonize sectors where battery-electric solutions face significant hurdles, such as long-haul trucking

and off-road applications. A key advantage for sustainability is the ability to leverage existing manufacturing infrastructure, with studies showing that up to 90% of conventional engine parts can be repurposed for hydrogen use, thus lowering initial investment costs and facilitating a smoother industrial transition. However, as this thesis demonstrates, material durability is a critical bottleneck. The future success of H_2ICEs is contingent on overcoming the HE challenges identified in key components. This necessitates a focus on advanced materials science. Promising developments, such as novel aluminum alloys engineered with complex nanoprecipitates that effectively trap hydrogen while simultaneously boosting strength, offer a direct solution to the trade-offs observed in this research. For cast irons, optimizing graphite morphology and alloying elements to create a high density of benign hydrogen traps is a crucial strategy. Ultimately, the long-term sustainability of H_2ICEs is intrinsically linked to the maturation of the broader hydrogen economy. Continued investment and innovation in low-cost green hydrogen production, coupled with the development of robust infrastructure for high-density hydrogen storage and distribution, are essential. By addressing both the material-specific challenges and the systemic infrastructure needs, H_2ICE technology can be firmly established as a cornerstone of a future, sustainable, and decarbonized transportation ecosystem.

Bibliography

[1] C. Battersby, “Hydrogen Industry Trends and Projections for 2025.” Accessed: Jun. 08, 2025. [Online]. Available: https://gibsonwatts.com/hydrogen-industry-trends-and-projections-for-2025/

[2] D. R. Prasser, “Hydrogen Economy Outlook 2025: Key Data & Innovations.” Accessed: Jun. 08, 2025. [Online]. Available: https://www.startus-insights.com/innovators-guide/hydrogen-economy-outlook/

[3] Q. Li, H. Ghadiani, V. Jalilvand, T. Alam, Z. Farhat, and M. A. Islam, “Hydrogen Impact: A Review on Diffusibility, Embrittlement Mechanisms, and Characterization,” Feb. 01, 2024, *Multidisciplinary Digital Publishing Institute (MDPI)*. doi: 10.3390/ma17040965.

[4] M. Swarnkar, “Hydrogen as a Fuel for IC Engines: Challenges, Opportunities, and Future Prospects,” *International Journal of I.C. Engines and Gas Turbines*, vol. 10, no. 2, 2024, doi: 10.37628/IJICEGT.

[5] N. Armaroli and V. Balzani, “The hydrogen issue,” Jan. 17, 2011, *Wiley-VCH Verlag*. doi: 10.1002/cssc.201000182.

[6] William Lee Jolly, “Hydrogen,” Encyclopedia Britannica. Accessed: Apr. 02, 2025. [Online]. Available: https://www.britannica.com/science/hydrogen

[7] M. Králik, “Adsorption, chemisorption, and catalysis,” 2014, *De Gruyter Open Ltd*. doi: 10.2478/s11696-014-0624-9.

[8] A. Da, “Adsorption from theory to practice,” 2001.

[9] X. Li, X. Ma, J. Zhang, E. Akiyama, Y. Wang, and X. Song, “Review of Hydrogen Embrittlement in Metals: Hydrogen Diffusion, Hydrogen Characterization, Hydrogen Embrittlement Mechanism and Prevention,” Jun. 01, 2020, *Chinese Society for Metals*. doi: 10.1007/s40195-020-01039-7.

[10] H. Yu *et al.*, “Hydrogen Embrittlement as a Conspicuous Material Challenge─Comprehensive Review and Future Directions,” May 22, 2024, *American Chemical Society*. doi: 10.1021/acs.chemrev.3c00624.

[11] Y. Fukai and H. Sugimoto, “Diffusion of hydrogen in metals,” *Adv Phys*, vol. 34, no. 2, pp. 263–326, Jan. 1985, doi: 10.1080/00018738500101751.

[12] B. Bal, B. Okdem, F. C. Bayram, and M. Aydin, “A detailed investigation of the effect of hydrogen on the mechanical response and microstructure of Al 7075 alloy under medium strain rate impact loading,” *Int J Hydrogen Energy*, vol. 45, no. 46, pp. 25509–25522, Sep. 2020, doi: 10.1016/j.ijhydene.2020.06.241.

[13] D. Rudomilova, T. Prošek, and G. Luckeneder, “Techniques for investigation of hydrogen embrittlement of advanced high strength steels,” Sep. 25, 2018, *De Gruyter*. doi: 10.1515/corrrev-2017-0106.

[14] B. Chen, S. Li, H. Zong, X. Ding, J. Sun, and E. Ma, “Unusual activated processes controlling dislocation motion in body-centered-cubic high-entropy alloys,” *PNAS*, vol. 117, no. 28, pp. 16199–16206, 2020, doi: 10.1073/pnas.1919136117/-/DCSupplemental.

[15] K. Y. Tsai, M. H. Tsai, and J. W. Yeh, “Sluggish diffusion in Co-Cr-Fe-Mn-Ni high-entropy alloys,” *Acta Mater*, vol. 61, no. 13, pp. 4887–4897, Aug. 2013, doi: 10.1016/j.actamat.2013.04.058.

[16] P. N. Anyalebechi and P. N. Anyalebechi, “Critical Review of Reported Values of Hydrogen Diffusion in Solid and Liquid Aluminum and its Alloys,” 2015. [Online]. Available: https://www.researchgate.net/publication/268369590

[17] Z. Wang, J. Liu, F. Huang, Y. J. Bi, and S. Q. Zhang, “Hydrogen Diffusion and Its Effect on Hydrogen Embrittlement in DP Steels With Different Martensite Content,” *Front Mater*, vol. 7, Dec. 2020, doi: 10.3389/fmats.2020.620000.

[18] A. Díaz, I. I. Cuesta, E. Martínez-Pañeda, and J. M. Alegre, “Influence of charging conditions on simulated temperature-programmed desorption for hydrogen in metals,” *Int J Hydrogen Energy*, vol. 45, no. 43, pp. 23704–23720, Sep. 2020, doi: 10.1016/j.ijhydene.2020.05.192.

[19] C. Hurley, F. Martin, L. Marchetti, J. Chêne, C. Blanc, and E. Andrieu, “Numerical modeling of thermal desorption mass spectroscopy (TDS) for the study of hydrogen diffusion and trapping interactions in metals,” *Int J Hydrogen Energy*, vol. 40, no. 8, pp. 3402–3414, Mar. 2015, doi: 10.1016/j.ijhydene.2015.01.001.

[20] R. A. Orianit, “THE DIFFUSION AND TRAPPING OF HYDROGEN IN STEEL*.”

[21] H. Chen, L. Zhao, S. Lu, Z. Lin, T. Wen, and Z. Chen, “Progress and Perspective of Ultra-High-Strength Martensitic Steels for Automobile,” Dec. 01, 2022, *MDPI*. doi: 10.3390/met12122184.

[22] W. Li, X. Zhu, J. Yao, X. Jin, and X. Ding, “Hydrogen traps and hydrogen induced cracking in 20CrMo steel,” *ISIJ International*, vol. 57, no. 1, pp. 170–175, 2017, doi: 10.2355/isijinternational.ISIJINT-2016-281.

[23] M. Nagumo, “Hydrogen related failure of steels - A new aspect,” Aug. 2004. doi: 10.1179/026708304225019687.

[24] J. G. Sezgin, C. Bosch, A. Montouchet, G. Perrin, and K. Wolski, “Modelling of hydrogen induced pressurization of internal cavities,” *Int J Hydrogen Energy*, vol. 42, no. 22, pp. 15403–15414, Jun. 2017, doi: 10.1016/j.ijhydene.2017.04.106.

[25] C. A. Zapffe and C. E. Sims, “Hydrogen embrittlement, internal stress and defects in steel,” *Trans. Aime*, vol. 145, no. 1941, pp. 225–271, 1941.

[26] F. D. Fischer and J. Svoboda, “Formation of bubbles by hydrogen attack and elastic-plastic deformation of the matrix,” *Int J Plast*, vol. 63, pp. 110–123, 2014, doi: 10.1016/j.ijplas.2013.10.007.

[27] D. G. Westlake, “GENERALIZED MODEL FOR HYDROGEN EMBRITTLEMENT.,” Argonne National Lab., Ill., 1969.

[28] P. Cotterill, “THE HYDROGEN EMBRITTLEMENT OF METALS.”

[29] V. Madina and I. Azkarate, “Compatibility of materials with hydrogen. Particular case: Hydrogen embrittlement of titanium alloys,” *Int J Hydrogen Energy*, vol. 34, no. 14, pp. 5976–5980, Jul. 2009, doi: 10.1016/j.ijhydene.2009.01.058.

[30] “The Effect of Occluded Hydrogen on the Tensile Strength o f Iron.” [Online]. Available: https://royalsocietypublishing.org/

[31] A. R. Troiano, “The Role of Hydrogen and Other Interstitials in the Mechanical Behavior of Metals: (1959 Edward De Mille Campbell Memorial Lecture),” *Metallography, Microstructure, and Analysis*, vol. 5, no. 6, pp. 557–569, Dec. 2016, doi: 10.1007/s13632-016-0319-4.

[32] Y. S. Chen *et al.*, “Hydrogen trapping and embrittlement in metals – A review,” *Int J Hydrogen Energy*, 2024, doi: 10.1016/j.ijhydene.2024.04.076.

[33] S. K. Dwivedi and M. Vishwakarma, “Hydrogen embrittlement in different materials: A review,” Nov. 15, 2018, *Elsevier Ltd*. doi: 10.1016/j.ijhydene.2018.09.201.

[34] B. Sun, D. Wang, X. Lu, D. Wan, D. Ponge, and X. Zhang, “Current Challenges and Opportunities Toward Understanding Hydrogen Embrittlement Mechanisms in Advanced High-Strength Steels: A Review,” Jun. 01, 2021, *Chinese Society of Metals*. doi: 10.1007/s40195-021-01233-1.

[35] J. Liu, M. Zhao, and L. Rong, “Overview of hydrogen-resistant alloys for high-pressure hydrogen environment: on the hydrogen energy structural materials,” Feb. 01, 2023, *Oxford University Press*. doi: 10.1093/ce/zkad009.

[36] M. B. Djukic, V. Sijacki Zeravcic, G. M. Bakic, A. Sedmak, and B. Rajicic, “Hydrogen damage of steels: A case study and hydrogen embrittlement model,” *Eng Fail Anal*, vol. 58, pp. 485–498, Dec. 2015, doi: 10.1016/j.engfailanal.2015.05.017.

[37] M. B. Djukic, G. M. Bakic, V. Sijacki Zeravcic, A. Sedmak, and B. Rajicic, “The synergistic action and interplay of hydrogen embrittlement mechanisms in steels and iron: Localized plasticity and decohesion,” Jul. 01, 2019, *Elsevier Ltd*. doi: 10.1016/j.engfracmech.2019.106528.

[38] M. Wasim, M. B. Djukic, and T. D. Ngo, “Influence of hydrogen-enhanced plasticity and decohesion mechanisms of hydrogen embrittlement on the fracture resistance of steel,” *Eng Fail Anal*, vol. 123, May 2021, doi: 10.1016/j.engfailanal.2021.105312.

[39] M. B. Djukic, V. S. Zeravcic, G. Bakic, A. Sedmak, and B. Rajicic, “Hydrogen Embrittlement of Low Carbon Structural Steel,” *Procedia Materials Science*, vol. 3, pp. 1167–1172, 2014, doi: 10.1016/j.mspro.2014.06.190.

[40] M. A. Tunes *et al.*, “Limitations of Hydrogen Detection After 150 Years of Research on Hydrogen Embrittlement,” Oct. 01, 2024, *John Wiley and Sons Inc*. doi: 10.1002/adem.202400776.

[41] H. J. Grabke and E. Riecke, “ABSORPTION AND DIFFUSION OF HYDROGEN IN STEELS ABSORPCIJA IN DIFUZIJA VODIKA V JEKLIH.”

[42] G. Lovicu *et al.*, “Hydrogen embrittlement of automotive advanced high-strength steels,” *Metall Mater Trans A Phys Metall Mater Sci*, vol. 43, no. 11, pp. 4075–4087, Nov. 2012, doi: 10.1007/s11661-012-1280-8.

[43] S. Lynch, “Hydrogen embrittlement phenomena and mechanisms,” Jun. 2012. doi: 10.1515/corrrev-2012-0502.

[44] F. D. Gregory, “Associate Administrator for Safety and Mission Assurance iii ACKNOWLEDGMENTS,” 1997.

[45] J. R. Scully, G. A. Young, and S. W. Smith, “Hydrogen embrittlement of aluminum and aluminum-based alloys,” in *Gaseous Hydrogen Embrittlement of Materials in Energy Technologies: The Problem, its Characterisation and Effects on Particular Alloy Classes*, Elsevier Ltd., 2012, pp. 707–768. doi: 10.1533/9780857093899.3.707.

[46] R. Walallawita, J. Stroh, and D. Sediako, “The Effect of Hydrogen Embrittlement on Aluminum Alloys Used for Hydrogen-Fueled Internal Combustion Engine,” in *Proceedings of the 61st Conference of Metallurgists, COM 2022*, Springer International Publishing, 2023, pp. 447–450. doi: 10.1007/978-3-031-17425-4_58.

[47] M. Safyari, M. Moshtaghi, and S. Kuramoto, “On the role of traps in the microstructural control of environmental hydrogen embrittlement of a 7xxx series aluminum alloy,” *J Alloys Compd*, vol. 855, Feb. 2021, doi: 10.1016/j.jallcom.2020.157300.

[48] Y. Chen, S. Zhao, H. Ma, H. Wang, L. Hua, and S. Fu, “Analysis of hydrogen embrittlement on aluminum alloys for vehicle-mounted hydrogen storage tanks: A review,” Aug. 01, 2021, *MDPI AG*. doi: 10.3390/met11081303.

[49] K. Shimizu *et al.*, “Hydrogen embrittlement and its prevention in 7XXX aluminum alloys with high Zn concentrations.” [Online]. Available: https://hdl.handle.net/2324/7160861

[50] P. V Petroyiannis, E. Kamoutsi, A. T. Kermanidis, S. G. Pantelakis, V. Bontozoglou, and G. N. Haidemenopoulos, “Evidence on the corrosion-induced hydrogen embrittlement of the 2024 aluminium alloy.”

[51] M. López Freixes *et al.*, “Revisiting stress-corrosion cracking and hydrogen embrittlement in 7xxx-Al alloys at the near-atomic-scale,” *Nat Commun*, vol. 13, no. 1, Dec. 2022, doi: 10.1038/s41467-022-31964-3.

[52] T. Košová Altnerová, D. Rudomilova, P. Novák, and T. Prošek, “The Role of Precipitates in Hydrogen Embrittlement of Precipitation-Hardenable Aluminum Alloys,” Nov. 01, 2024, *Multidisciplinary Digital Publishing Institute (MDPI)*. doi: 10.3390/met14111287.

[53] R. Braun, “Environmentally assisted cracking of aluminium alloys,” *Materwiss Werksttech*, vol. 38, no. 9, pp. 674–689, Sep. 2007, doi: 10.1002/mawe.200700204.

[54] Y. Xu *et al.*, “Suppressed hydrogen embrittlement of high-strength Al alloys by Mn-rich intermetallic compound particles,” *Acta Mater*, vol. 236, Sep. 2022, doi: 10.1016/j.actamat.2022.118110.

[55] L. T. H. Nguyen, J. S. Hwang, M. S. Kim, J. H. Kim, S. K. Kim, and J. M. Lee, “Charpy impact properties of hydrogen-exposed 316l stainless steel at ambient and cryogenic temperatures,” *Metals (Basel)*, vol. 9, no. 6, Jun. 2019, doi: 10.3390/met9060625.

[56] T. Omura and J. Nakamura, “Hydrogen Embrittlement Properties of Stainless and Low Alloy Steels in High Pressure Gaseous Hydrogen Environment,” 2012.

[57] “Standard Practice for Slow Strain Rate Testing to Evaluate the Susceptibility of Metallic Materials to Environmentally Assisted Cracking 1.”

[58] “Corrosion of metals and alloys-Stress corrosion testing-Part 7: Method for slow strain rate testing,” 2005.

[59] F. Von Zeppelin, M. Haluška, and M. Hirscher, “Thermal desorption spectroscopy as a quantitative tool to determine the hydrogen content in solids,” *Thermochim Acta*, vol. 404, no. 1–2, pp. 251–258, Sep. 2003, doi: 10.1016/S0040-6031(03)00183-7.

[60] B. A. Abebe, “A Review on hydrogen embrittlement behavior of steel structures and measurement methods,” *International Advanced Researches and Engineering Journal*, Aug. 2024, doi: 10.35860/iarej.1414085.

[61] T. Haruna, M. Imamura, and Y. Hirohata, “Pitting Corrosion of Titanium Depending on the Properties of the Passive Film,” *J Electrochem Soc*, vol. 171, no. 1, p. 011502, Jan. 2024, doi: 10.1149/1945-7111/ad1ace.

[62] K. Bergers, E. C. De Souza, I. Thomas, N. Mabho, and J. Flock, “Determination of Hydrogen in steel by Thermal Desorption Mass Spectrometry,” *Steel Res Int*, vol. 81, no. 7, pp. 499–507, Jul. 2010, doi: 10.1002/srin.201000023.

[63] D. J. Long, E. Tarleton, A. C. Cocks, and F. Hofmann, “The link between Microstructural Heterogeneity, Diffusivity, and Hydrogen Embrittlement,” Feb. 2025, [Online]. Available: http://arxiv.org/abs/2502.13793

[64] W. Zhou, R. P. Apkarian, Z. Lin Wang, and D. Joy, “Fundamentals of Scanning Electron Microscopy.”

[65] K. D. Vernon-Parry, “Scanning Electron Microscopy: an introduction.”

[66] C. Y. Tang and Z. Yang, “Transmission Electron Microscopy (TEM),” in *Membrane Characterization*, Elsevier Inc., 2017, pp. 145–159. doi: 10.1016/B978-0-444-63776-5.00008-5.

[67] J. Ćwiek, “Prevention methods against hydrogen degradation of steel,” 2010. [Online]. Available: www.journalamme.org

[68] M. Wetegrove *et al.*, “Preventing Hydrogen Embrittlement: The Role of Barrier Coatings for the Hydrogen Economy,” Jun. 01, 2023, *Multidisciplinary Digital Publishing Institute (MDPI)*. doi: 10.3390/hydrogen4020022.

[69] D. Figueroa and M. J. Robinson, “The effects of sacrificial coatings on hydrogen embrittlement and re-embrittlement of ultra high strength steels,” *Corros Sci*, vol. 50, no. 4, pp. 1066–1079, Apr. 2008, doi: 10.1016/j.corsci.2007.11.023.

[70] Y. Wu, C. Wang, X. Qin, J. Hou, and L. Zhou, “Segregation sequence of phosphorus and its effect on impact toughness of GH984G alloy during thermal exposure,” *Journal of Materials Research and Technology*, vol. 18, pp. 200–209, May 2022, doi: 10.1016/j.jmrt.2022.02.098.

[71] B. Sun *et al.*, “Chemical heterogeneity enhances hydrogen resistance in high-strength steels,” *Nat Mater*, vol. 20, no. 12, pp. 1629–1634, Dec. 2021, doi: 10.1038/s41563-021-01050-y.

[72] H. Ye, “An Overview of the Development of Al-Si-Alloy Based Material for Engine Applications.”

[73] L. Xiao *et al.*, “Microstructure and Mechanical Properties of Cast Al-Si-Cu-Mg-Ni-Cr Alloys: Effects of Time and Temperature on Two-Stage Solution Treatment and Ageing,” *Materials*, vol. 16, no. 7, Apr. 2023, doi: 10.3390/ma16072675.

[74] M. Timpel *et al.*, “The role of strontium in modifying aluminium-silicon alloys,” *Acta Mater*, vol. 60, no. 9, pp. 3920–3928, May 2012, doi: 10.1016/j.actamat.2012.03.031.

[75] E. Fracchia, F. S. Gobber, and M. Rosso, “Effect of alloying elements on the Sr modification of Al-Si cast alloys,” *Metals (Basel)*, vol. 11, no. 2, pp. 1–19, Feb. 2021, doi: 10.3390/met11020342.

[76] M. F. Ibrahim, E. M. Elgallad, S. Valtierra, H. W. Doty, and F. H. Samuel, “Metallurgical parameters controlling the eutectic silicon charateristics in be-treated Al-Si-Mg alloys,” *Materials*, vol. 9, no. 2, 2016, doi: 10.3390/ma9020078.

[77] H. Zhao *et al.*, “Hydrogen trapping and embrittlement in high-strength Al alloys,” *Nature*, vol. 602, no. 7897, pp. 437–441, Feb. 2022, doi: 10.1038/s41586-021-04343-z.

[78] K. Hirayama, H. Toda, T. Suzuki, M. Uesugi, A. Takeuchi, and W. Ludwig, “Crystallographic Analysis of Hydrogen Embrittlement Behavior in Aluminum Alloy Using Diffraction Contrast Tomography,” *Mater Trans*, vol. 63, no. 4, pp. 586–591, 2022, doi: 10.2320/matertrans.MT-L2021020.

[79] Y. Yang, K. Yu, Y. Li, D. Zhao, and X. Liu, “Evolution of nickel-rich phases in Al-Si-Cu-Ni-Mg piston alloys with different Cu additions,” *Mater Des*, vol. 33, no. 1, pp. 220–225, Jan. 2012, doi: 10.1016/j.matdes.2011.06.058.

[80] P. MikoŁajczak and L. Ratke, "Three dimensional morphology of β-Al5FeSi intermetallics in AlSi alloys," *Archives of Foundry Engineering*, vol. 15, no. 1, pp. 47–50, Mar. 2015, doi: 10.1515/afe-2015-0010.

[81] H. Chen, S. Wu, J. Li, D. Zhao, and S. Lü, "Effects of Low Nickel Content on Microstructure and High-Temperature Mechanical Properties of Al-7Si-1.5Cu-0.4Mg Aluminum Alloy," *Metals (Basel)*, vol. 14, no. 2, Feb. 2024, doi: 10.3390/met14020223.

[82] S. A. Awe, S. Seifeddine, A. E. W. Jarfors, Young. C. Lee, and A. K. Dahle, "Development of new Al-Cu-Si alloys for high temperature performance," *Adv Mater Lett*, vol. 8, no. 6, pp. 695–701, Jun. 2017, doi: 10.5185/amlett.2017.1471.

[83] M. Vončina, T. Balaško, M. Petrič, J. Medved, O. Modrijan, and J. Li, "Effect of the addition of Ni and Cu on solidification microstructure evolution of Al-5Si-0.5Mg alloys," *International Journal of Metalcasting*, 2024, doi: 10.1007/s40962-024-01449-8.

[84] M. Yamaguchi, M. Itakura, T. Tsuru, and K. I. Ebihara, "Hydrogen-trapping energy in screw and edge dislocations in aluminum: First-principles calculations," *Mater Trans*, vol. 62, no. 5, pp. 582–589, 2021, doi: 10.2320/matertrans.MT-M2020375.

[85] J. C. Liu, A. D. Marwick, and F. K. Legoues, "Hydrogen segregation and trapping in the Al/Si(111) interface," Jul. 1991.

[86] P. Chao and R. A. Karnesky, "Hydrogen Isotope Trapping in Al-Cu Binary Alloys," 2016.

[87] M. Yamaguchi *et al.*, "Hydrogen trapping in Mg2Si and Al7FeCu2 intermetallic compounds in aluminum alloy: First-Principles calculations," *Mater Trans*, vol. 61, no. 10, pp. 1907–1911, Oct. 2020, doi: 10.2320/matertrans.MT-M2020201.

[88] P. Sahiluoma, Y. Yagodzinskyy, A. Forsström, H. Hänninen, and S. Bossuyt, "Hydrogen embrittlement of nodular cast iron," *Materials and Corrosion*, vol. 72, no. 1–2, pp. 245–254, Jan. 2021, doi: 10.1002/maco.202011682.

[89] A. Forsström, Y. Yagodzinskyy, and H. Hänninen, "Hydrogen effects on mechanical performance of nodular cast iron," *Corrosion Reviews*, vol. 37, no. 5, pp. 441–454, 2019, doi: 10.1515/corrrev-2019-0007.

[90] MatWeb, "Overview of materials for Ductile Iron." Accessed: May 10, 2025. [Online]. Available: https://www.matweb.com/search/datasheet.aspx?matguid=9d44544b44a44addaae133fb3ae3fcf9&utm_source=chatgpt.com&ckck=1

[91] D. M. Abdelrahim, E. E. Ateia, and A. A. Nofal, "Effect of Molybdenum Contents on Microstructure and High-Temperature Wear Behavior of SiMo Ductile Iron," *International Journal of Metalcasting*, vol. 18, no. 1, pp. 530–545, Jan. 2024, doi: 10.1007/s40962-023-01012-x.

[92] F. Dong, M. Zhang, F. Peng, and J. Zhang, "Preparation and Mechanical Properties of High Silicon Molybdenum Cast Iron Materials: Based on Deep Learning Model," *Comput Intell Neurosci*, vol. 2022, pp. 1–12, Sep. 2022, doi: 10.1155/2022/4825356.

[93] X. R. Chen, Q. J. Zhai, H. Dong, B. H. Dai, and H. Mohrbacher, "Molybdenum alloying in cast iron and steel," *Adv Manuf*, vol. 8, no. 1, pp. 3–14, Mar. 2020, doi: 10.1007/s40436-019-00282-1.

[94] H. K. D. H. Bhadeshia, "Prevention of hydrogen embrittlement in steels," 2016, *Iron and Steel Institute of Japan*. doi: 10.2355/isijinternational.ISIJINT-2015-430.

[95] Y. Zheng, P. Yu, and L. Zhang, “Atomistic Study of the Interaction Nature of H-Dislocation and the Validity of Elasticity in Bcc Iron,” *Metals (Basel)*, vol. 13, no. 7, Jul. 2023, doi: 10.3390/met13071267.

[96] K. Kawakami and T. Matsumiya, “Ab-initio investigation of hydrogen trap state by cementite in bcc-Fe,” *ISIJ International*, vol. 53, no. 4, pp. 709–713, 2013, doi: 10.2355/isijinternational.53.709.

[97] Y. Song *et al.*, “Effect of cementite on the hydrogen diffusion/trap characteristics of 2.25Cr-1Mo-0.25V steel with and without annealing,” *Materials*, vol. 11, no. 5, May 2018, doi: 10.3390/ma11050788.

[98] L. Vandewalle, T. Depover, and K. Verbeken, “Hydrogen trapping of carbides during high temperature gaseous hydrogenation,” *Int J Hydrogen Energy*, vol. 42, pp. 32158–32168, Sep. 2023.

[99] N. Abe, H. Suzuki, K. Takai, N. Ishikawa, and H. Sueyoshi, “Identification of hydrogen trapping sites, binding energies, and occupation ratios at vacancies, dislocations and grain boundaries in iron of varying carbon content,” vol. 2, pp. 1277–1284, Jan. 2011.

[100] T. Matsuo, “The effect of pearlite on the hydrogen-induced ductility loss in ductile cast irons,” in *Journal of Physics: Conference Series*, Institute of Physics Publishing, May 2017. doi: 10.1088/1742-6596/843/1/012012.

[101] *BSI Standards Publication Microstructure of cast irons*. 2019.

[102] V. Balobanov, M. Lindroos, T. Andersson, and A. Laukkanen, “Crystal Plasticity Modeling of Grey Cast Irons under Tension, Compression and Fatigue Loadings,” *Crystals (Basel)*, vol. 12, no. 2, Feb. 2022, doi: 10.3390/cryst12020238.

[103] N. Mu *et al.*, “The effects of water vapor and hydrogen on the high-temperature oxidation of alloys,” in *Oxidation of Metals*, Jun. 2013, pp. 461–472. doi: 10.1007/s11085-012-9349-8.

Thank you